Viscoelastic fluids: From the macroscale to the microscale

Inaugural Dissertation

zur Erlangung des Doktorgrades

der Mathematisch-Naturwissenschaftlichen Fakultät

der Heinrich-Heine-Universität Düsseldorf

vorgelegt von

Linnea Heitmeier

aus Leverkusen

Köln, Januar 2026

aus dem Institut für Theoretische Physik II: Weiche Materie
der Heinrich-Heine-Universität Düsseldorf

Gedruckt mit der Genehmigung der
Mathematisch-Naturwissenschaftlichen Fakultät der
Heinrich-Heine-Universität Düsseldorf

Berichterstatter:
1. Prof. Dr. Thomas Voigtmann
2. Prof. Dr. Hartmut Löwen
3. Prof. Dr. Liesbeth Janssen

Tag der mündlichen Prüfung: 26.06.26

Eidesstattliche Versicherung

Ich, Linnea Heitmeier, versichere an Eides statt, dass die vorliegende Dissertation von mir selbstständig und ohne unzulässige fremde Hilfe unter Beachtung der "Grundsätze zur Sicherung guter wissenschaftlicher Praxis an der Heinrich-Heine- Universität Düsseldorf" erstellt worden ist.

Leverkusen, 29.01.2026 Linnea Heitmeier

Linnea Heitmeier

Abstract

We investigate the behavior of viscoelastic fluids both from a macroscopic and a microscopic perspective, with a special focus on interfacial phenomena.
First, experiments on viscoelastic droplet spreading were carried out in microgravity, in a regime where surface tension significantly governs the spreading behavior. These experiments were complemented by simulations of the Navier-Stokes equation, using a modified version of the Oldroyd-B model. The experiments and simulations allowed to test scaling laws derived from a thin-film solution of the Navier-Stokes equation.
Secondly, we investigated the surface tension between glass-forming fluids and vacuum using Molecular-Dynamics simulations, and found a pronounced shear-rate dependence of the surface tension. For experiments, this is highly relevant, as it explains a possible microscopic mechanism behind phenomena like hysteresis during surface tension measurements.
We conclude our studies by performing Molecular-Dynamics simulations of viscoelastic fluids, which were confined on the nanoscale. Here, we found pronounced non-local effects, which do not occur on the macroscale.

Kurzzusammenfassung der Doktorarbeit

In der vorliegenden Arbeit untersuchen wir das Verhalten scherverdünnender viskoelastischer Flüssigkeiten aus sowohl makroskopischer als auch mikroskopischer Perspektive, mit einem besonderen Schwerpunkt auf oberflächeninduzierten Effekten.

Im ersten Teil der Arbeit analysieren wir die Ausbreitung viskoelastischer Tropfen unter Schwerelosigkeit. Eine solche Versuchsanordnung erweitert nicht nur den zugänglichen Parameterraum erheblich, sondern erlaubt auch eine gezielte Untersuchung der Rolle der Oberflächenspannung. Ergänzend zu den Experimenten führen wir Simulationen der Navier–Stokes-Gleichungen durch, in denen eine modifizierte Variante des Oldroyd-B-Modells zum Einsatz kommt. Mit diesen Experimenten und Simulationen können Skalengesetze überprüft werden, die aus einer Dünnfilm-Näherung der Navier-Stokes Gleichung hergeleitet wurden.

Motiviert durch die experimentellen Ergebnisse, die darauf hinweisen, dass die Oberflächenspannung viskoelastischer Fluide deutlich komplexer ist als diejenigen Newtonscher Fluide, widmen wir uns im zweiten Projekt der mikroskopischen Beschreibung der Oberflächenspannung. Mithilfe von Molekulardynamik-Simulationen untersuchen wir glasbildende Fluide und bestimmen deren Oberflächenspannung. Dieses Projekt zeigt, dass viskoelastische Fluide eine scherratenabhängige Oberflächenspannung aufweisen, deren Aus-

wirkungen auch experimentell nachweisbar sind. Darüber hinaus identifizieren wir Beiträge sowohl aus dem Oberflächenbereich als auch aus dem Bulkbetrag.

Abschließend präsentieren wir Simulationen viskoelastischer Flüssigkeiten auf der Nanoskala. Dabei beobachten wir ausgeprägte nichtlokale Effekte, die auf größeren Längenskalen nicht auftreten.

List of publications

- Related to **chapter 3**: Heitmeier, L., D'Angelo, O., Jalaal, M., and Voigtmann, Th. "Spreading droplets of yield-stress fluids with and without gravity."
  Journal of Rheology 70, 631–643 (2026), also listed as Ref. [1]

  My contribution to this paper included the analysis and interpretation of the experimental data, the conduction and analysis of the simulations, and writing parts of the manuscript. The text presented in this thesis has been minimally edited, in order to unify the references with the rest of this thesis.

- Related to **chapter 4**: Heitmeier, L., and Voigtmann, Th. "Shear-Rate Dependent Surface Tension of Glass-Forming Fluids."
  Physical Review Letters 136, 068203 (2026), also listed as Ref. [2]

  My contribution to this paper included the conceptualization, conduction and analysis of the simulations, and writing parts of the manuscript. The text presented in this thesis has been minimally edited, in order to unify the references with the rest of this thesis.

- Related to **chapter 5**: Heitmeier, L., Voigtmann, Th., and Hansen, J.S. "Spectral analysis of the velocity relaxation in nanoscale channels.", *Physics of Fluids* 37, 122019 (2025), also listed as Ref. [3]

My contribution to this paper included the conduction and analysis of the simulations, and writing parts of the manuscript. The text presented in this thesis has been minimally edited, in order to unify the references with the rest of this thesis.

Table of Contents

List of Tables

List of Figures

List of Abbreviations

BCG Bell-Collela-Glaz.

CFL Courant-Friedrichs-Lewy.

GPU Graphics Processing Unit.

ISS International Space Station.

LJ-potential Lennard-Jones-potential.

MCT Mode Coupling Theory.

MD Molecular-Dynamics.

PAA poly acrylic acid.

RUMD Roskilde-University Molecular Dynamics.

VOF Volume-of-Fluid.

WCA-potential Weeks-Chandler-Andersen potential.

YSF yield-stress fluid.

ZARM Center of Applied Space Technology and Microgravity.

List of Symbols

$E_{\mathbf{kin}}$ Kinetic energy.

G_∞ Shear modulus.

Ma Mach-number.

Pe Péclet number.

Re Reynolds number.

T Temperature.

ϵ Energy.

η Viscosity.

$\hat{\sigma}$ Surface tension.

κ Curvature.

$\mathcal{B}$ Bond number.

$\mathcal{C}a$ Capillary number.

$\mathcal{J}$ Plastocapillary number.

$\mathcal{O}h$ Ohnesorge number.

ρ Density.

σ Particle diameter.

τ Relaxation time.

$\underline{r}$ Position.

$\underline{u}$ Velocity.

$\underline{\underline{\sigma}}$ Stress tensor.

c_s Speed of sound.

p Pressure.

t Time.

Chapter 1

Introduction

Complex fluids are omnipresent in both everyday life and industrial applications. They occur in a wide range of different materials, including pastes, gels, emulsions, foams, and various other biological and industrial suspensions [5–7]. One of the most widely recognized applications of these fluids is additive manufacturing. There, the rheological properties of the filament are critical for controlling the flow and deposition processes [8–11]. A very prominent example where complex fluids are used as a filament can be found in the field of bioprinting [12, 13]. Beyond additive manufacturing, complex fluids play a crucial role in numerous other emerging technologies. To mention only a few, applications related to food processing, to pharmaceutical formulations and to energy storage, often rely on the knowledge of the fluid's rheological properties to control spreading, coating, or solidification [14–18].

From a physical point of view, complex fluids can be divided into two groups: Viscoelastic fluids and non-linear fluids. Viscoelastic fluids occupy an intermediate regime between liquids and solids: on short timescales, they exhibit solid-like elasticity, whereas on long timescales they flow like viscous fluids. On the microscopic level, viscoelasticity arises from the deformation and relaxation of microstructures such as polymer chains, colloidal networks, or particle

contacts. The characteristic timescales of these relaxation processes determine the transition from elastic to viscous response. Motivated by this separation of timescales, viscoelastic fluids are often modeled using the Maxwell or Oldroyd-B model, which describe the superposition of a Newtonian fluid and a Hookean spring [19, 20]: on small timescales compared to the material-specific relaxation time their constitutive law has the structure of the one of a Hookean spring, on large timescales, it has the structure of the one of a Newtonian fluid. In the case of a vanishing relaxation time, they reduce to a Newtonian fluid. While in these fluids, the viscosity is a constant, which particularly does not depend on the shear-rate, the viscosity of non-linear fluids depends on the shear-rate. Fluids with a viscosity which decreases with increasing shear-rate are called *shear-thinning* fluids. If the viscosity is increasing with increasing shear-rate the fluid's behavior is called *shear-thickening*. These rheological properties are widely used in applications. For example, only the fact that paint is showing a shear-thinning behavior, makes it possible to both get it out of the bucket, and paint a wall with it. Another class of non-linear fluids are *yield-stress* fluids. These fluids behave like an elastic solid, if the applied stress is below a certain stress, the yield stress, and they start to flow if the stress is above this threshold [21–23]. All these categories are idealized classifications. In reality the phenomena often overlap, e.g. many of the fluids we discuss in the following are viscoelastic, shear-thinning, and yield-stress fluids to some extent. Despite decades of research, many fundamental aspects of both viscoelastic and non-linear fluids, particularly near interfaces, remain poorly understood [24–28].

The primary goal of this thesis is to advance the understanding of complex fluids from both macroscopic and microscopic perspectives, with a special focus on interfacial phenomena. In particular, we study fluids which are a combination of the two groups described above: By investigating the behavior of viscoelastic fluids with a shear-rate dependent relaxation time, we cover both the property of the viscoelasticity and of the non-linearity. A schematic representation of the topics of this thesis can be seen in figure 1.1.

We start our investigations at the macroscale, studying spreading viscoelastic droplets in microgravity. The use of microgravity is essential in this study, as this allows us to study the influence of surface tension, without interferences of gravitational forces. These experimental results were complemented with simulations of the Navier-Stokes equations, which model the fluid from a continuum perspective, using the aforementioned Oldroyd-B model with a shear-rate dependent relaxation time. A strong agreement was observed between the experimental measurements and the simulation results. The experiments were primarily determined by two dimensionless numbers: The Bond-number $\mathcal{B}$, which quantifies the relative importance of gravitational forces compared to capillary forces arising from surface tension; and the plasto-capillary number $\mathcal{J}$, which compares the capillary forces with the effect of the yield-stress of a material. By performing the experiments in microgravity, we significantly enhanced the parameter space of the available data. Additionally, these experiments suggested that the value of the surface tension of yield-stress fluids is hard to determine, which is also in accordance to literature [29, 30].

As the property of the surface tension is not only important for studying droplets, but also in many industrial applications, like wetting and lubrication, we investigated the phenomenon of surface tension in more detail, using a microscopic approach, namely Molecular-Dynamics simulations. The aim of this study is to measure the surface tension, while the surface is moved, *i.e.* while we impose a shear-rate on the system. The underlying idea behind this problem is as follows: While complex fluids are normally characterized by the viscosity (or similarly the relaxation time) and their shear-rate dependence, it should be investigated, whether also other material properties like the surface tension show a shear-rate dependence. The results of this study also have a huge experimental relevance: By showing that there is indeed a shear-rate dependence of the surface tension, we also progress in understanding the hysteresis effects which are present in experimental measurements [29, 30].

This microscopic study, which has many implications for macroscopic processes, raises the question about the lengthscales until which the fluid can be described with the same model as for large lengthscales. Hence, we further investigated a viscoelastic fluid confined to the nanoscale. It is known that hydrodynamic laws are valid also on very small scales, but at these lengthscales, some other effects come into play. For example, the viscosity on these lengthscales cannot be modeled as a constant anymore, but as a spatially dependent variable. The key idea of this project was to study the relaxation behavior of a viscoelastic fluid in a nanochannel. Using a continuous model of a viscoelastic fluid with a spatial-dependent relaxation time, we were able to identify non-local effects in the nanofluid. Similar to the other projects, this part of the thesis has a wide range of applications in technological applications ranging from the biomedical sector to the industrial one [31–36].

The structure of the thesis is as follows:

- Chapter 2 provides the theoretical background and details the simulation methods used throughout the thesis, covering both macroscopic and microscopic approaches.
- Chapter 3 presents the investigation of droplet spreading under microgravity, including a comparison between experiments and macroscopic simulations, showing good agreement, and follows Ref. [1]
- Chapter 4 focuses on a free surface under shear from a microscopic perspective, demonstrating the shear-rate dependence of surface tension and its relevance for experimental measurements and hysteresis effects, and follows Ref. [2]
- Chapter 5 examines viscoelastic fluids in nanoscale confinement, highlighting the emergence of non-local effects, and follows Ref. [3]
- Chapter 6 concludes the thesis and outlines directions for future research.

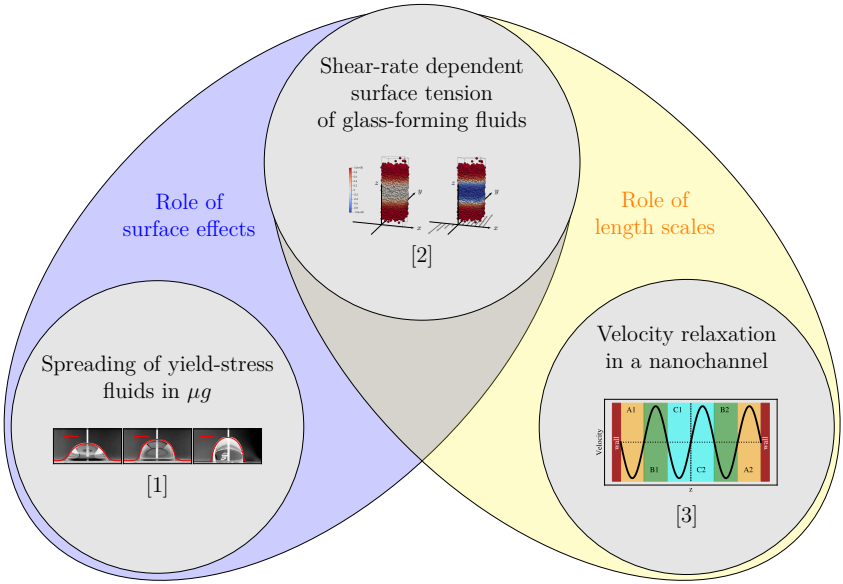

Figure 1.1: Scope of the thesis, highlighting the main overlaps between the different projects. While the first two projects investigate the role of surface effects, also the role of length scales is investigated.

Chapter 2

Theoretical Background

In this chapter, the theoretical framework of the thesis is presented. The first, more physically oriented part derives the fundamental equations of hydrodynamics. Here, we discuss both perspectives: the macroscopic one, based on field-theoretical methods, and the microscopic one, described by fluctuating hydrodynamics. In the second, more technically oriented part, we present numerical methods related to both macroscopic (continuous) investigations (e.g., Volume-of-Fluid (VOF) to solve the Navier–Stokes equations) and to microscopic (particle-resolved) ones (e.g., Molecular-Dynamics (MD) simulations).

2.1 Hydrodynamics

2.1.1 Macroscopic view: Field equations

2.1.1.1 Conservation Equations

Before deriving the conservation equations, we first make a brief remark on how to describe the flow of a fluid. In principle, there are two ways to characterize fluid motion: either by following a single fluid element as it moves and deforms over time (the Lagrangian description), or by considering a fixed control volume and analyzing what flows in and out of it (the Eulerian description).

As it is simpler for many applications the Eulerian description is often chosen. For the conversion between those two points of view, let us assume that we want to follow some scalar quantity a of one fluid element. Let $\underline{r} = (x, y, z)$ be the position vector, $\underline{u} = (u_x, u_y, u_z)$ the flow velocity and t the time. The change of a in time while following the fluid element, and expressed in the fixed coordinate frame $a(\underline{r}, t)$ can be written as

$$\frac{\mathrm{d}a}{\mathrm{d}t} = \lim_{dt\to 0} \frac{a(\underline{r} + \underline{u}\mathrm{d}t, t + \mathrm{d}t)}{\mathrm{d}t} = \frac{\partial a}{\partial t} + \sum_i u_i \frac{\partial a}{\partial x_i} = \frac{\partial a}{\partial t} + \underline{u} \cdot \nabla a \tag{2.1.1}$$

Motivated by this equation, in fluid-dynamics, one defines the "material derivative" (also called "convected derivative") as:

$$\frac{D}{Dt} = \frac{\partial}{\partial t} + \underline{u} \cdot \nabla \tag{2.1.2}$$

Now, we derive the conservation equations using the following strategy: first, we derive a general relation for a conserved quantity, and from this, we get the corresponding specific conservation laws.

We derive an expression for the conservation of the hydrodynamic quantity $\psi = \psi(\underline{r}, t)$. A general conservation equation for this quan-

tity can be written as

$$\frac{d}{dt}\int_\Omega \psi \mathrm{d}\Omega = -\int_\Gamma \psi \underline{u}\cdot\underline{n}\mathrm{d}\Gamma - \int_\Omega s\mathrm{d}\Omega \tag{2.1.3}$$

Here, Ω denotes the control volume, Γ its boundary, $\underline{n}$ the outward-pointing normal vector, $\underline{u}$ the flow velocity, and s are the sinks (or sources, depending on the sign). In words, this relation states that the rate of change of ψ within the control volume equals the net flux of ψ across its boundary plus the contributions from sources and sinks.
According to the divergence theorem [37], one then can derive:

$$\frac{d}{dt}\int_\Omega \psi \mathrm{d}\Omega = -\int_\Omega \nabla\cdot(\psi\underline{u})\mathrm{d}\Omega - \int_\Omega s\mathrm{d}\Omega \tag{2.1.4}$$

With Reynolds transport theorem [37] and the assumption that Ω does not change in time, one then gets:

$$\int_\Omega \frac{\partial\psi}{\partial t}\mathrm{d}\Omega = -\int_\Omega \nabla\cdot(\psi\underline{u})\mathrm{d}\Omega - \int_\Omega s\mathrm{d}\Omega \tag{2.1.5}$$

Since this relation must hold for any arbitrary control volume Ω, we finally obtain the following conservation equation:

$$\frac{\partial\psi}{\partial t} = -\nabla\cdot(\psi\underline{u}) - s \tag{2.1.6}$$

This relation can now be applied to derive an equation for the conservation of mass. Here, we set $\psi = \rho(\underline{r}, t)$, with ρ being the mass density. Since we do not assume any sources or sinks of mass, we set $s = 0$. The mass conservation equation then becomes:

$$\frac{\partial\rho}{\partial t} + \nabla\cdot(\rho\underline{u}) = 0 \tag{2.1.7}$$

For incompressible fluids, i.e. $\frac{D}{Dt}\rho = 0$, this equation reduces to

$$\nabla\cdot\underline{u} = 0 \tag{2.1.8}$$

To derive the momentum conservation equation, we set $\psi = \rho\underline{u}$ in equation 2.1.6:

$$\frac{\partial}{\partial t}(\rho\underline{u}) + \nabla \cdot (\rho\underline{u}\underline{u}) = \underline{s} \tag{2.1.9}$$

With the property of the divergence of a dyadic product $\nabla \cdot (\underline{a}\underline{b}) = (\nabla \cdot \underline{a})\underline{b} + \underline{a} \cdot (\nabla \times \underline{b})$, we can reformulate equation 2.1.9 to

$$\begin{aligned} &\underline{u}\frac{\partial \rho}{\partial t} + \rho\frac{\partial \underline{u}}{\partial t} + \underline{u}\nabla \cdot (\rho\underline{u}) + \rho\underline{u} \cdot \nabla\underline{u} = \underline{s} \\ \Leftrightarrow\ &\underline{u}\left(\frac{\partial \rho}{\partial t} + \nabla \cdot (\rho\underline{u})\right) + \rho\left(\frac{\partial \underline{u}}{\partial t} + \underline{u} \cdot \nabla\underline{u}\right) = \underline{s} \\ \Leftrightarrow\ &\rho\frac{D\underline{u}}{Dt} = \rho\left(\frac{\partial \underline{u}}{\partial t} + \underline{u} \cdot \nabla\underline{u}\right) = \underline{s} \end{aligned} \tag{2.1.10}$$

Finally, one gets the momentum-conservation equation as:

$$\rho\left(\frac{\partial \underline{u}}{\partial t} + \underline{u} \cdot \nabla\underline{u}\right) = \underline{s} \tag{2.1.11}$$

Finally, the source term $\underline{s}$ in the general momentum equation can now be defined explicitly. This term represents the total force acting on a fluid element, which can be divided into two contributions: First, there are body (external) forces, such as gravity or electromagnetic forces, denoted by $\rho\,\underline{f}_{\text{ext}}$, where f denotes the acceleration density caused by the forces. Secondly, there are internal forces, which arise from the interactions between adjacent fluid elements.

The internal forces are described by the Cauchy stress tensor $\underline{\underline{\Sigma}}$, which represents the force per unit area on internal surfaces. This tensor can be decomposed into the isotropic pressure p and the viscous stress tensor $\underline{\underline{\sigma}}$:

$$\underline{\underline{\Sigma}} = -p\,\underline{\underline{I}} + \underline{\underline{\sigma}} \tag{2.1.12}$$

Here, we used $\underline{\underline{I}}$ as the identity matrix. Substituting this relation into the general momentum balance yields the Navier-Stokes equation:

$$\rho\left(\frac{\partial \underline{u}}{\partial t} + \underline{u} \cdot \nabla\underline{u}\right) = -\nabla p + \nabla \cdot \underline{\underline{\sigma}} + \rho\,\underline{f}_{\text{ext}}. \tag{2.1.13}$$

2.1.1.2 Constitutive law for a shear-thinning yield-stress fluid

With the balance equations which were derived in the previous section (equation 2.1.8 and 2.1.13), we obtain an underdetermined system of equations. In order to close this system, additional relations are required. These are provided by the so-called constitutive equations, which describe the material-specific relationship between the stress tensor $\underline{\underline{\sigma}}$ and the strain-rate tensor $\dot{\underline{\underline{\gamma}}}$. The latter is defined as

$$\dot{\gamma}_{ij} = \partial_i u_j + \partial_j u_i, \tag{2.1.14}$$

and characterizes the local deformation rate of the fluid elements due to velocity gradients. One of the simplest constitutive equations assumes a linear dependence:

$$\underline{\underline{\sigma}} = \eta \cdot \dot{\underline{\underline{\gamma}}} + \frac{1}{2}\left(\eta_b - \frac{2}{3}\eta\right) \underline{\underline{I}} : \dot{\underline{\underline{\gamma}}} \tag{2.1.15}$$

Fluids with such a behavior are called "Newtonian" fluids with the viscosity η and the bulk viscosity η_b [38]. Note that η_b is irrelevant for incompressible flows.
In this case, the incompressible Navier-Stokes equation reduces to

$$\rho\left(\frac{\partial \underline{u}}{\partial t} + \underline{u} \cdot \nabla \underline{u}\right) = -\nabla p + \eta \nabla^2 \underline{u} + \rho\, \underline{f}_{\text{ext}}. \tag{2.1.16}$$

Prominent examples of Newtonian fluids are water, air and glycerin [39].
Nevertheless, in nature there exist many fluids with a different, so-called "non-Newtonian" behavior: Fluids, whose viscosity is decreasing with increasing shear-rate, are called shear-thinning fluids. An example of this class of fluids are paints [40]. Those, whose viscosity is increasing with increasing shear-rate are called shear-thickening. For example, corn starch suspensions show this behavior [41].

Another important phenomenological effect is the yield-stress: If the stress is below a certain value, the so-called yield-stress, such fluids behave like a solid. Above this stress, they are behaving like a fluid.

There is a wide amount of different models describing such fluids. One very famous model is the Herschel-Bulkley model. This model is defined for one component of the stress tensor. The underlying idea is that in *simple shear*, the shear-rate has only one non-vanishing component $\dot{\gamma}_{xy}$. Then, it is sufficient to write the model in terms of $\dot{\gamma}_{xy} = \dot{\gamma}$ and $\sigma_{xy} = \sigma$. The model can be formulated as [42]

$$\begin{aligned} \dot{\gamma} &= 0 && \text{if } \sigma < \sigma_0 \\ \sigma &= \sigma_0 + k\dot{\gamma}^n && \text{if } \sigma \geq \sigma_0 \end{aligned}$$

This model explicitly defines the yield-stress σ_0. k is called a consistency factor, and n is called flow index, which is assumed to be a positive number. For $n < 1$, one gets a shear-thinning behavior, and for $n > 1$, one gets shear-thickening behavior.

The viscoelastic fluid is here described by using a stress σ, which is the superposition of a Newtonian contribution σ_N and a polymeric contribution σ_P, which shows non-Newtonian behavior.

$$\begin{aligned} \sigma_{\mathrm{N}} &= \eta_{\mathrm{N}} \cdot \dot{\gamma} \\ \left(\frac{1}{\tau} + \partial_t\right) \sigma_{\mathrm{P}} &= G_\infty \dot{\gamma} \\ \sigma &= \sigma_{\mathrm{N}} + \sigma_{\mathrm{P}} \end{aligned} \tag{2.1.17}$$

Here, τ denotes the relaxation time, and G_∞ the shear modulus. The physical idea of this model is that the polymeric stress behaves like a solid on short timescales compared to τ and like a fluid on long timescales, i.e., it combines the features of Hooke's law for elastic solids and Newton's law for viscous fluids. From this, it follows that the total constitutive law can be written in the following form:

$$\left(\frac{1}{\tau} + \partial_t\right) \sigma = \eta_{\mathrm{N}} \left(\frac{G_\infty}{\eta_{\mathrm{N}}} + \frac{1}{\tau} + \partial_t\right) \dot{\gamma} \tag{2.1.18}$$

Figure 2.1 shows schematically how the viscosity depends on the shear-rate for a shear-thinning fluid. For low and for high shear-rates, the viscosity approaches constants, $\eta_0 = G_\infty \tau + \eta_N$ and $\eta_\infty =$

η_N, respectively. Between these constants, the viscosity decays with $1/\dot{\gamma}$. Hence, to model a shear-thinning fluid, we use formula 2.1.18, with a shear-rate dependent relaxation time $\tau^{-1} \rightarrow \tau^{-1} + \dot{\gamma}/\gamma_c$. Here, γ_c is a constant with a value inspired by microscopic theories [43].

Finally, to model an apparent yield-stress, the low-shear-rate region, in which the viscosity is constant, should vanish. Hence, in this case, the relaxation time should go to infinity. The resulting yield-stress is related to the occurring quantities as $\sigma_0 = G_\infty \cdot \gamma_c$.

This model can be extended by replacing the time-derivative of the constitutive equation with the so-called "upper-convected" derivative. This derivative is defined for an arbitrary tensor $\underline{\underline{A}}$ as

$$\overset{\triangledown}{\underline{\underline{A}}} = \partial_t \underline{\underline{A}} + \underline{u} \cdot \nabla \underline{\underline{A}} - ((\nabla u)^T \cdot \underline{\underline{A}} + \underline{\underline{A}} \cdot (\nabla u)) \tag{2.1.19}$$

The constitutive equation of the Oldroyd-B model is then given as

$$\left(\frac{1}{\tau} + \overset{\triangledown}{\cdot}\right) \underline{\underline{\sigma}} = \eta_\mathrm{N} \left(\frac{G_\infty}{\eta_\mathrm{N}} + \frac{1}{\tau} + \overset{\triangledown}{\cdot}\right) \underline{\underline{\dot{\gamma}}} \tag{2.1.20}$$

The advantage of this model in comparison to (2.1.18) is that this model fulfills the principle of material objectivity [44]. This means that the constitutive law is independent of time-dependent rotations and motion of the fluid.

2.1.1.3 Lubrication Theory

The idea of lubrication theory is to derive an approximation of the Navier-Stokes equations that is valid for thin films.
Since in chapter 3 we investigate the spreading process of droplets, we here employ lubrication theory to derive a partial differential equation describing the height profile of a spreading droplet.

Such calculations have already been performed for Newtonian fluids (as presented here) [45, 46], Bingham fluids, which account for a

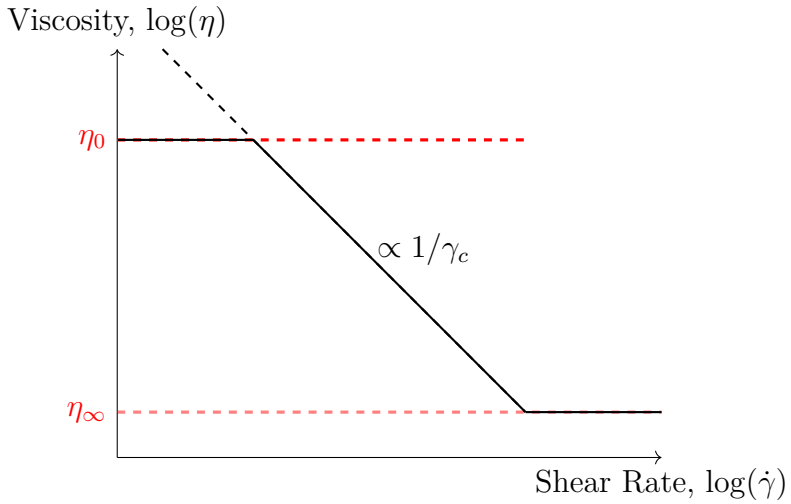

Figure 2.1: Schematic illustration of the viscosity of a shear-thinning fluid.

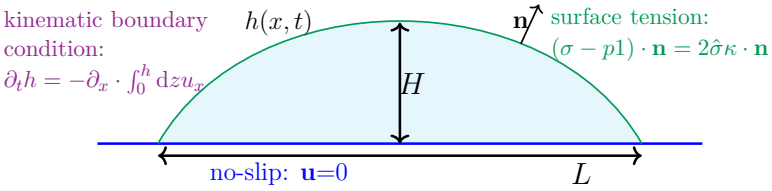

Figure 2.2: Illustration of the setup of the sessile droplet and the corresponding boundary conditions.

yield stress [47], and Jeffrey fluids, which model viscoelastic behavior [48]. Motivated by these results, we are interested in deriving a thin-film equation for a viscoelastic fluid that also incorporates a yield stress. This derivation is presented in the appendix of chapter 3.

Let us first recall the principles of the thin-film approximation. We assume the droplet or thin-film, which is spreading on a pre-wetted surface, to have a height of the order of H, and a width of order L, as shown in figure 2.2. The height profile is described by the function $h(x,t)$.

For simplification we reduce our calculations to the 2-dimensional case, but an extension to 3 dimensions would be straightforward. For the spreading process of a droplet, several boundary conditions should be fulfilled:

1. At the substrate, we assume a no-slip boundary condition, such that $\underline{u}|_{z=0} = 0$.

2. At the free surface, the droplet is subject to a surface tension $\hat{\sigma}$, which gives rise to the boundary condition.

$$(\sigma - p1) \cdot \underline{n} = 2\hat{\sigma}\kappa\,\underline{n} \tag{2.1.21}$$

   Here, $\underline{n}$ denotes the outward-pointing normal vector of the fluid surface, and κ represents the curvature of the droplet's surface. To facilitate working with this boundary condition, it is convenient to introduce a tangential vector $\underline{t}$ in addition to the normal vector $\underline{n}$, defined as

$$\underline{n} = \frac{1}{\sqrt{1+(\partial_x h)^2}} \begin{pmatrix} -\partial_x h \\ 1 \end{pmatrix} \text{ and } \underline{t} = \frac{1}{\sqrt{(1+(\partial_x h)^2}} \begin{pmatrix} 1 \\ \partial_x h \end{pmatrix}$$

   such that $|n|^2 = |t|^2 = 1$ and $\underline{n} \cdot \underline{t} = 0$.

3. We make use of the kinematic boundary condition which relates the time evolution of the droplet's height with the ve-

locities inside the droplet

$$\partial_t h = -\partial_x \int_0^h \mathrm{d}z u_x \tag{2.1.22}$$

This equation can be derived by considering a small slice in x-direction of width $\mathrm{d}x$. The volumetric flux inside this slice can be written as $Q(x,t) = \int_0^{h(x,t)} \mathrm{d}z u_x$. As the change of the droplet height at a point x depends on how much of the fluid is flowing in or out of the slice, we get: $\partial_t h = -\partial_x Q(x,t)$, which is in fact the kinematic boundary condition.

The boundary conditions are also illustrated in figure 2.2.

The next step is to non-dimensionalize all equations, using the small aspect ratio $\epsilon = H/L \ll 1$. Once this is done, each equation can be approximated by neglecting terms of order ϵ or higher. This leads to a simplified set of equations that captures the behavior of the thin film. A detailed summary on which variable is scaled in which way can be found in table 2.1.

First, one can see that the mass-conservation equation (2.1.8) is already non-dimensional. Secondly, we can treat the momentum equation (2.1.13) component-wise. The non-dimensional formulations of the x- and z-component are

$$\begin{aligned} \epsilon^2 Re \cdot \frac{du_x}{dt} &= \epsilon^2 \cdot \partial_x \sigma_{xx} + \partial_z \sigma_{xz} - \partial_x p \\ \epsilon^4 Re \cdot \frac{du_z}{dt} &= \epsilon^2 (\partial_x \sigma_{xz} + \partial_z \sigma_{zz}) - \partial_z p \end{aligned} \tag{2.1.23}$$

Here, the Reynolds-number was defined as $Re = \frac{\rho U L}{\eta}$ by using the characteristic velocity $U = L/T$. We assume this number to be of order 1, since we assume the flow to be laminar.
The constitutive law for a Newtonian fluid can be written for each

component individually, using the non-dimensional viscosity η^*:

$$\begin{aligned} \sigma_{xx} &= \eta^* \partial_x u_x \\ \sigma_{zz} &= \eta^* \partial_z u_z \\ \sigma_{xz}/\epsilon = \sigma_{zx}/\epsilon &= \eta^* \left(\epsilon \partial_x u_z + \frac{1}{\epsilon} \partial_z u_x \right) \end{aligned} \tag{2.1.24}$$

The no-slip boundary condition is also non-dimensional.
The surface tension is treated by first multiplying relation (2.1.21) with the normal vector $\underline{n}$ from the left, which gives:

$$\begin{aligned} \frac{1}{1+(\epsilon \partial_x h)^2} \cdot [\sigma_{zz} - 2 \cdot \sigma_{xz} \partial_x h + \epsilon^2 \sigma_{xx} (\partial_x h^2)] - \frac{p}{\epsilon^2} \\ = \frac{\hat{\sigma}}{\epsilon^2} \cdot \frac{\partial_x^2 h}{(1+(\epsilon \cdot \partial_x h)^2)^{3/2}} \end{aligned} \tag{2.1.25}$$

Similarly, we can multiply the tangential vector from the left, which gives:

$$[1 - \epsilon^2 (\partial_x h)^2] \cdot (\sigma_{xz} \partial_x h) + \epsilon^2 \cdot [\sigma_{zz} (\partial_x h)^2 - \sigma_{xx} (\partial_x h)^2] = 0 \tag{2.1.26}$$

In the next step, we use that all terms which are at least of order ϵ can be neglected.
With this, the momentum equations become:

$$\begin{aligned} \partial_z \sigma_{xz} &= \partial_x p \\ 0 &= \partial_z p \end{aligned} \tag{2.1.27}$$

Up to here, the calculation is generally valid for every kind of fluid. For this section, we choose the constitutive law of a **Newtonian fluid**. In chapter 3, we also show a similar calculation for a shear-thinning viscoelastic fluid. From the Newtonian constitutive law (2.1.24), we get

$$\sigma_{xz} = \eta^* \partial_z u_x \tag{2.1.28}$$

From the boundary condition, which includes the surface tension (equation (2.1.25)), we get

$$p = -\hat{\sigma} \cdot \partial_x h \tag{2.1.29}$$

From equations (2.1.27), we find that p is independent of z. Hence, we can integrate the relation for σ_{xz} from z to h with respect to z and get:

$$\sigma_{xz} = (z - h)\partial_x p \tag{2.1.30}$$

Using the constitutive law 2.1.28, we then get

$$\eta^* \partial_z u_x = (z - h)\partial_x p \tag{2.1.31}$$

This can be integrated one time more with respect to z from 0 to z, using the boundary conditions at the substrate.

$$\int_0^z \mathrm{d}z \eta^* \partial_z u_x = \int_0^z \mathrm{d}z (z - h)\partial_x p \Rightarrow \left(\frac{z^2}{2} - hz\right)\partial_x p = \eta^* u_x \tag{2.1.32}$$

A further integration from 0 to $z = h$ gives:

$$\int_0^h \mathrm{d}z \left(\frac{z^2}{2} - hz\right)\partial_x p = \eta^* \int_0^h \mathrm{d}z u_x \Rightarrow -\frac{h^3}{3} \cdot \partial_x p = \eta^* \int_0^h \mathrm{d}z u_x \tag{2.1.33}$$

Finally, we can include the kinematic boundary condition, introduced in equation (2.1.22):

$$-\partial_x \left\{ -\frac{h^3}{3} \cdot \partial_x p \right\} = \eta^* \partial_t h \tag{2.1.34}$$

We get the final result by using the relation from the free surface (2.1.25):

$$-\partial_x \left\{ \frac{h^3}{3} \cdot \partial_x^3 h \right\} = \frac{\eta^*}{\hat{\sigma}} \partial_t h \tag{2.1.35}$$

An application of this equation is the derivation of "Tanner's" law, which describes the spreading behavior of a cylindrical-symmetric droplet. First, equation (2.1.35) is formulated for a cylindrical-symmetric system, using the radial coordinate r:

$$\frac{\eta^*}{\hat{\sigma}}\partial_t h + \frac{1}{r}\partial_r \left\{ r \cdot \frac{h^3}{3} \cdot \partial_r^3 h \right\} = 0 \tag{2.1.36}$$

The droplet's height is then defined as $H(t)$, its radius is given by $R(t)$. We assume the time-dependence of these functions to be:

$$R(t) \sim t^{\alpha} \text{ and } H(t) \sim t^{-\beta} \tag{2.1.37}$$

For axisymmetric droplets, during the whole spreading process it holds that HR^2 is constant due to conservation of volume. With (2.1.37), it follows:

$$\beta = 2\alpha \tag{2.1.38}$$

Additionally, we can include this ansatz into the thin-film equation (2.1.36) to get:

$$t^{-\beta-1} \sim t^{-4\beta} t^{-4\alpha} \tag{2.1.39}$$

Hence, it holds that

$$4\alpha + 3\beta = 1 \tag{2.1.40}$$

Equations (2.1.38) and (2.1.40) can be solved. Its solution is given by $\alpha = 1/10$. This is refereed to as Tanner's law, stating that

$$R(t) \sim t^{1/10} \tag{2.1.41}$$

	quantity	scaling
lengths	$x,\ z,\ h$	$L \cdot x^*,\ \epsilon L z^*,\ \epsilon L h^*$
velocities	$u_x\ ,\ u_z$	$U \cdot u_x^*,\ \epsilon U \cdot u_z^*$
pressure	p	$P \cdot p$
surface tension	$\hat{\sigma}$	$\frac{U\eta}{\epsilon^3}\hat{\sigma}^*$
stress tensor	$\begin{pmatrix} \sigma_{xx} & \sigma_{xz} \\ \sigma_{zx} & \sigma_{zz} \end{pmatrix}$	$\frac{\eta}{T}\begin{pmatrix} \sigma_{xx}^* & \sigma_{xz}^*/\epsilon \\ \sigma_{zx}^*/\epsilon & \sigma_{zz}^* \end{pmatrix}$
time	t	$T \cdot t^*$

Table 2.1: Summary of how the different variables are scaled in the lubrication approximation.

2.1.2 Overview over non-dimensional numbers

At this point, we got to know a wide range of different non-dimensional numbers which play a large role in hydrodynamics. The aim of the following section is to give a detailed overview over the most important numbers, their definitions and their physical meaning.

Abbr.	Name	Def.	Meaning
Re	Reynolds number	$\frac{\rho u \mathcal{L}}{\eta}$	compares viscous forces and inertial forces
$\mathcal{B}$	Bond number	$\frac{\rho g \mathcal{L}^2}{\hat{\sigma}}$	compares gravitational forces with surface tension induced forces
$\mathcal{J}$	plastocapillary number	$\frac{\sigma_0 \mathcal{L}}{\hat{\sigma}}$	compares yield stress with surface tension
$\mathcal{O}h$	Ohnesorge number	$\frac{\eta}{\sqrt{\mathcal{L}\rho\hat{\sigma}}}$	compares inertial forces with surface tension
Pe	Péclet number	$\dot{\gamma} \cdot \tau_0$	compares advection with diffusion
$\mathcal{C}a$	Capillary number	$\frac{\eta U}{\hat{\sigma}}$	compares the viscous forces with the surface tension
Ma	Mach number	$\frac{U}{c_s}$	compares the flow velocity with the speed of sound

2.1.3 Microscopic view: Hydrodynamics on the nanoscale

Until now, we have assumed that in hydrodynamics all quantities vary smoothly in both space and time, an assumption known as the continuum hypothesis [49]. This is also the reason why all variables have so far been treated as field quantities.

However, when studying fluids on the nanoscale, this assumption no longer strictly holds. For instance, when considering a very small fluid element, it becomes clear that, due to thermal motion, fluid particles continuously enter and leave the element. As a result, the mass contained within this volume fluctuates in time. From this example, it follows that the field theory explained above, only holds at sufficiently large volumes. It turns out — as also demonstrated by the results in chapter 5 — that the precise meaning of this breakdown is not obvious a priori, and that hydrodynamics can in fact be applied on surprisingly small length scales. When studying hydrodynamics on the nanoscale, three main assumptions can be made:

1. Advective forces can be neglected, as the fluid velocity normally does not exceed $0.1m/s$ (see for example Whiteby and Quirke [50]) . Hence, the Reynolds number is in practice always below 0.01 [51].

2. Compressibility effects can be ignored. This is normally quantified by the Mach number, defined as $Ma = U/c_s$, with c_s being the speed of sound. If $Ma \lesssim 0.3$, the fluid can be treated as an incompressible fluid [52]. For water at ambient conditions, and c_s being in the order of 10^3m/s, the Mach-number is smaller than 0.1.

3. It is still possible to describe the fluid's motion by the continuous equations, which were derived above, but they have to be extended by some corrections. It turns out that these corrections can be modelled in terms of non-local variables.

2.1.3.1 Introductory example

A wide range of phenomena are characterized by confinement at the nanoscale. Prominent examples include slip velocities of flows through nanochannels [53, 54], capillary rise [55, 56], and anisotropic behavior of confined dielectrics [57, 58].

In this section, we focus on the effect of the non-local viscous response, which is highly relevant for the analysis of the simulation data presented in chapter 5. This effect was first found by Todd et al. [59]. In this paper, the authors study a fluid, which is infinite in extent, and impose a sinusoidal force, which acts in x-direction:

$$\underline{F}_{\text{ext}} = \rho g_0 \cos(kz)\underline{e}_x \tag{2.1.42}$$

Here, ρ is the density, g_0 is a constant and k is the wavelength of the force and $\underline{e}_x$ is the unit vector in x-direction.

For symmetry reasons, the only non-zero stress-tensor component in this system is σ_{xz}. Hence, in this example, we set $\sigma_{xz} = \sigma$. First, we can write the momentum balance equation in the steady-state:

$$\frac{\partial \sigma}{\partial z} = -\rho g_0 \cos(kz) \tag{2.1.43}$$

For $\sigma(z = 0) = 0$, we get by integrating

$$\sigma(z) = -\frac{\rho g_0}{k} \sin(kz) \tag{2.1.44}$$

Using Newton's law for the viscosity, one can also predict the stress by

$$\sigma(z) = -2\eta_0 \dot{\gamma}(z) \tag{2.1.45}$$

Where $\dot{\gamma}$ is the shear-rate (which is for symmetry reasons simply $\partial_z v_x$). Due to the functional form of the applied force, we get that the shear-rate in this example is given by $\dot{\gamma} = \tilde{\dot{\gamma}}(k)\sin(kz)/2$. So, the stress can also be written as

$$\sigma(z) = -\eta_0 \tilde{\dot{\gamma}}(k) \sin(kz) \tag{2.1.46}$$

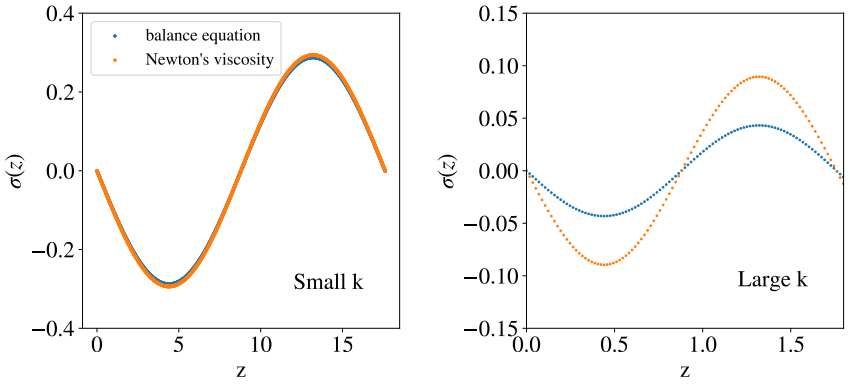

Figure 2.3: Shear-stress profiles from a fluid, which is subjected to a sinusoidal force. Figure replotted from Ref. [51].

In Figure 2.3, the stress values obtained from the balance equation and from Newton's law of viscosity are shown for both small and large wavelengths. For large wavelengths, Newton's law accurately predicts the stress values from the balance equation. However, for small wavelengths, comparable to the atomic spacing, a significant stress reduction is observed. This phenomenon is believed to originate from the non-local response of the fluid to shear forces [51].

As a solution, one can model the viscosity as a function, which depends on the distance between the particle and all other points in the system.

2.1.3.2 Fluctuating hydrodynamics

The concept of fluctuating hydrodynamics extends the field-theoretical approach described above, but now we also take into account the fluctuations of the observables. So, we write the quan-

tities as

$$\begin{aligned}\rho(\underline{r},t) &= \rho_{av} + \delta\rho(\underline{r},t)\\ \rho(\underline{r},t)\underline{u}(\underline{r},t) &= (\rho_{av} + \delta\rho(\underline{r},t)) \cdot (\underline{u}_{\mathrm{av}} + \delta\rho(\underline{r},t)) \approx \rho_{av}\delta\underline{u}(\underline{r},t)\end{aligned} \tag{2.1.47}$$

As we assume being in the steady-state, we set $u_{\mathrm{av}} = 0$. Additionally, we treat fluctuations only until the first order. To derive an equation for the mass balance, we start at the relation $\frac{\partial\rho(\underline{r},t)}{\partial t} = -\nabla \cdot (\rho(\underline{r},t) \cdot \underline{u}(\underline{r},t))$ (see equation 2.1.7) and insert the terms with fluctuations:

$$\frac{\partial[\rho_{av} + \delta\rho(\underline{r},t)]}{\partial t} = -\nabla \cdot [(\rho_{av} + \delta\rho(\underline{r},t)) \cdot \delta\underline{u}(\underline{r},t)] \tag{2.1.48}$$

Keeping only the first order of fluctuations, we get:

$$\frac{\partial\delta\rho(\underline{r},t)}{\partial t} = -\nabla \cdot (\rho_{av}\delta\underline{u}(\underline{r},t)) \tag{2.1.49}$$

Similarly, we can derive the momentum-balance equation. To do so, we start with the momentum-conservation equation 2.1.13, and write it as:

$$\frac{\partial}{\partial t}(\rho\underline{u}) - \underline{u}\frac{\partial\rho}{\partial t} + \rho\underline{u} \cdot \nabla\underline{u} = -\nabla \cdot \underline{\underline{\sigma}} + \underline{f}(\underline{r},t) \tag{2.1.50}$$

Using the mass-balance equation, we get

$$\frac{\partial}{\partial t}(\rho\underline{u}) + \underline{u}(\nabla \cdot \rho\underline{u}) + \rho\underline{u} \cdot \nabla\underline{u} = -\nabla \cdot \underline{\underline{\sigma}} + \underline{f}(\underline{r},t) \tag{2.1.51}$$

Inserting the relations 2.1.47, we finally get the momentum-balance equation for fluctuations

$$\rho_{av}\frac{\partial}{\partial t}(\delta\underline{u}) = -\nabla \cdot \underline{\underline{\sigma}} + \underline{f}(\underline{r},t) \tag{2.1.52}$$

As a constitutive law, we here make use of the Newtonian constitutive law, formulated as [51]:

$$\sigma_{ij} = \eta_0\dot{\gamma}_{ij} + \left(\eta_{\mathrm{b}} - \frac{2}{3}\eta_0\right)\delta_{ij}\partial_k u_k \tag{2.1.53}$$

η_b is here the abbreviation for the bulk viscosity.
To conclude this section, the classical fluctuating hydrodynamic equations are given by

$$\frac{\partial \delta\rho(\underline{r},t)}{\partial t} = -\rho_{av}\nabla\cdot(\delta\underline{u}(\underline{r},t)) \tag{2.1.54a}$$

$$\rho_{av}\frac{\partial}{\partial t}(\delta\underline{u}) = -\nabla\cdot\left[\delta p(\underline{r},t) + \left(\eta_b + \frac{1}{3}\eta_0\right)\nabla\cdot\delta\underline{u}\right]\underline{\underline{I}} + \eta_0\nabla^2\delta\underline{u} - \nabla\cdot\delta\underline{\underline{P}} \tag{2.1.54b}$$

Often, their Fourier-transformation, which is defined as $f(\underline{k},t) = \int f(\underline{r},t)e^{-i\underline{k}\cdot\underline{r}}\mathrm{d}r$, is used:

$$\frac{\partial}{\partial t}\delta\rho(\underline{k},t) = -i\rho_0\underline{k}\cdot\delta\underline{u}(\underline{k},t) \tag{2.1.55a}$$

$$\rho_{av}\frac{\partial}{\partial t}\delta\underline{u}(\underline{k},t) = \tag{2.1.55b}$$

$$-i\underline{k}\left[\delta p(\underline{k},t) - \left(\eta_b - \frac{1}{3}\eta_0\right)[i\underline{k}\cdot\delta\underline{u}(\underline{k},t)]\underline{\underline{1}}\right] - \eta_0 k^2\delta\underline{u}(\underline{k},t) - i\underline{k}\cdot\delta P(\underline{k},t)$$

2.1.3.3 Transverse dynamics

As it is a very important for the understanding of nanoscale hydrodynamics, we here explain the main features of the transverse dynamics. Since it is not used much in the rest of the thesis, we only give a short overview about this topic. A more in-depth explanation can be found for example in [51]. For the transverse dynamics, we assume having a wave-vector $\underline{k}$, which is directed along the z-axis, hence $\underline{k} = (0,0,k_z)$. The transverse momentum density is then defined as

$$C^{\perp}(k,t) = \langle \delta u_x(k,t)\cdot\delta u_x(-k,t)\rangle \tag{2.1.56}$$

From the equations above (equation (2.1.55a)), we get in this case:

$$\rho_{av}\frac{\partial}{\partial t}\delta u_x(k,t) = -\eta_0 k^2\delta u_x(k,t) - ikP_{xz} \tag{2.1.57}$$

For the correlation function, we can derive:

$$\rho_{av}\frac{\partial}{\partial t}C^{\perp}(k,t) = -\eta_0 k^2 C^{\perp}(k,t) \tag{2.1.58}$$

This differential equation can be solved by using the equipartition theorem ($C^{\perp}(k_z,0) = \rho_0 k_B T$):

$$C^{\perp}(k,t) = \rho_{av} k_B T e^{-\eta_0 k^2 t/\rho_0} \tag{2.1.59}$$

From this, one can conclude that the transverse momentum of a Newtonian fluid is predicted to relax exponentially.

2.1.3.4 Velocity relaxation in a nanochannel

In chapter 5, we performed a spectral analysis of the velocity relaxation in nanoscale channels. To prepare for this, we first discuss the general relaxation behavior that can be expected without a mode analysis. A detailed derivation can be found in [60]. For times $t < 0$, the system is subjected to an external driving force of the form

$$F_{\text{ext}} = \rho A \sin(k_n z), \tag{2.1.60}$$

with ρ denoting the fluid density, A the amplitude, and $k_n = 2\pi n/h$ the corresponding wavevector. Here, h represents the channel width, and $n \in \mathbb{N}_+$. One can assume no-slip Dirichlet boundary conditions. The steady-state profile can then be derived from the momentum balance equation, hence

$$\rho\frac{\partial u}{\partial t} = F_{\text{ext}} - \frac{\partial \sigma_{xz}}{\partial z} \tag{2.1.61}$$

For abbreviation, we denote the velocity in x-direction as u. In the steady-state, it is a good assumption to take the fluid to be Newtonian, hence

$$\sigma_{xz} = -2\eta_0\dot{\gamma} = -\eta_0\frac{\partial u}{\partial z} \tag{2.1.62}$$

With this and the momentum conservation equation, we get

$$\frac{d^2u_0}{dz^2} = -\frac{A\rho}{\eta_0}\sin(k_n z) \tag{2.1.63}$$

Using the boundary condition, it directly follows that

$$u_0(z) = \frac{A\rho}{\eta_0 k_n^2}\sin(k_n z) := U_n \sin(k_n z) \tag{2.1.64}$$

Note that this steady-state velocity profile should be understood as the "ideal" one. In the simulations, it turns out that also other modes are excited, see [60] and chapter 5. To study the relaxation behavior, which is a time-dependent process, it turns out that we need a time-dependent constitutive law, formulated as the Maxwell model

$$\frac{\partial u}{\partial z} = -\frac{1}{\eta_0}\left(1 + \tau\frac{\partial}{\partial t}\right)\sigma_{xz} \tag{2.1.65}$$

Here, τ is the relaxation time. For a detailed description of the physical meaning of this equation, the reader is referred to section 2.1.1.2. Note that for the steady-state this model reduces to a Newtonian fluid.
In Laplace space, this equation can be written as

$$\frac{\partial \hat{u}}{\partial z} = -\frac{1}{\eta_0}(1 + \tau s)\hat{\sigma}_{xz} + \frac{\tau}{\eta_0}\sigma_{xz}(z, 0) \tag{2.1.66}$$

Here, the variable s comes from the Laplace transformation, which is defined as

$$\hat{f}(s) = \mathcal{L}\{f\}(s) = \int_0^\infty \mathrm{d}t f(t) e^{-st} \tag{2.1.67}$$

The initial condition can be obtained by using the steady-state profile:

$$\frac{\partial}{\partial z}\sigma_{xz}(z, 0) = \rho A \sin(k_n z) \tag{2.1.68}$$

Finally, one obtains

$$\frac{\partial^2 \hat{u}}{\partial z^2} - \frac{s(1-\tau s)\rho}{\eta_0}\hat{u} = \frac{A}{\eta_0}\frac{\tau\eta_0 k_n^2 - (1+\tau s)\rho}{\eta_0 k_n^2} \tag{2.1.69}$$

This equation can be solved analytically. One gets [60]:

$$u(z,t) = u_0(z) \cdot \exp(-\Gamma t)\Lambda(t) \tag{2.1.70}$$

using $\Gamma = 1/(2\tau)$ and

$$\Lambda(t) = \begin{cases} \frac{1-2\tau\mu}{\sqrt{1-4\tau\mu}}\sinh(\omega_0 t) + \cosh(\omega_0 t), & \text{if } \tau \leq 1/(4\mu) \\ \frac{1-2\tau\mu}{\sqrt{1-4\tau\mu}}\sin(\omega_0 t) + \cos(\omega_0 t), & \text{if } \tau > 1/(4\mu) \end{cases}$$

with $\mu = \eta_0 k_n^2/\rho$ and $\omega_0 = \sqrt{|1-4\tau\mu|}/(2\tau)$. As a consistency-check, one can see that for a Newtonian fluid ($\tau \to 0$), one gets a simple exponential decay.

2.2 Methods

2.2.1 Microscopic simulations: MD Simulations

MD simulations are based on a simple idea: by numerically solving the classical equations of motion, one can track how particles move and interact over time. From these microscopic trajectories, macroscopic properties are then obtained by averaging over the particles and/or over long time spans.

Since its inception, MD simulations became more and more important and were applied to a wide range of systems such as crystals, amorphous solids and liquids [61–68]. In the following section, we will provide a brief overview of the method. Because of its importance for this thesis, we will specifically explain the setup of MD simulations for free surfaces (used in chapter 4) and confined systems (used in chapter 5), as well as the use of a Graphics Processing Unit (GPU) to accelerate the simulations.

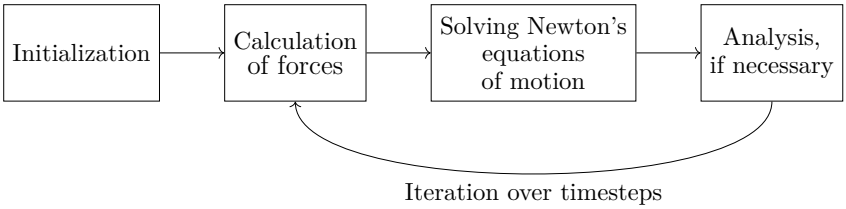

Figure 2.4: Schematic overview of the MD algorithm.

2.2.1.1 Algorithm of MD simulations

The basic idea of MD simulations is illustrated in figure 2.4.
In the first step, one initializes the system. A more in-depth discussion of this step can be found below.

Once an initial configuration is set, the forces can be calculated from the particle positions. These forces are derived from the interaction energy between the particles. In its most general form, this is given by [69, 70]

$$V(\underline{r}) = \sum_{i<j} V_{ij}(\underline{r}_i, \underline{r}_j) + \sum_{i<j<k} V_{ijk}(\underline{r}_i, \underline{r}_j, \underline{r}_k) + \sum_{i<j<k<l} V_{ijkl}(\underline{r}_i, \underline{r}_j, \underline{r}_k, \underline{r}_l) + ... \tag{2.2.1}$$

Here, V is the interaction energy, $\underline{r}$ are the particle positions and $\underline{r}_i$, $\underline{r}_j$, $\underline{r}_k$, and $\underline{r}_l$ represent the individual particle positions. In most systems, the interaction energy is dominated by contributions from pairs of particles. Therefore, MD simulations typically use pair potentials to describe these interactions, which simplifies the calculations.

The choice of the functional form of the pair potential is not obvious in itself. For liquids, one often makes use of the Lennard-Jones-potential (LJ-potential), see figure 2.5, which was first used in 1924 [71]. The idea behind this potential is that at large distances, attractive interaction due to van-der-Waals forces becomes dominant.

The attraction, which is also called London dispersion force, scales with $1/r^6$. At small distances, Pauli repulsion becomes dominant due to overlapping electrons. This exponent of this repulsion is empirically chosen, and the repulsion scales with $1/r^{12}$. From this, one gets a functional form of the LJ-potential as

$$V_{LJ}(r) = 4\epsilon \left(\left(\frac{\sigma}{r} \right)^{12} - \left(\frac{\sigma}{r} \right)^{6} \right) \tag{2.2.2}$$

using the distance σ, which is often associated with the particle diameter and the energy scale ϵ. Working with this potential, one often makes use of the unit system associated with these two quantities, a timescale τ and a mass $\epsilon = \frac{m\sigma^2}{\tau^2}$. This unit system is summarized in table 2.2. The LJ-potential is a model potential for Argon and noble gases [72]. In the case of Argon, the values are normally set to $\sigma = 3.405$Å and $\epsilon/k_B = 119.8$K [69].

To reduce computational cost, interactions are typically calculated only for particles within a cutoff distance $r < r_{\text{cut}}$, rather than considering all particles in the system. In terms of potential, this means that $V(r) = V_{LJ}(r)$ for distances smaller than r_{cut}, and $V(r) = 0$ for distances larger than r_{cut}. To avoid the discontinuity at r_{cut}, one well-established way is to make use of a "truncated and shifted" LJ-potential, formulated as

$$V_{\text{shifted LJ}}(r) = \begin{cases} V_{\text{LJ}}(r) - V_{\text{LJ}}(r_{\text{cut}}) & \text{if } r < r_{\text{cut}} \\ 0 & \text{else} \end{cases} \tag{2.2.3}$$

Another often used potential is the Weeks-Chandler-Andersen potential (WCA-potential), which is simply given by the repulsive part of the LJ-potential, shifted to r_{cut}:

$$V_{\text{WCA}}(r) = \begin{cases} V_{\text{LJ}}(r) + \epsilon & \text{if } r < r_{\text{cut}} \\ 0 & \text{else} \end{cases} \tag{2.2.4}$$

Alternative choices for describing interactions include machine-learning potentials, which are trained to reproduce reference data from experiments [73, 74].

quantity	unit
distance	σ
mass	m
time	$\tau = \sigma\sqrt{m/\epsilon}$
energy	ϵ
velocity	σ/τ
force	ϵ/σ
temperature	ϵ/k_B
pressure	ϵ/σ^3
density	m/σ^3
surface tension	ϵ/σ^2
viscosity	$\epsilon\tau/\sigma^3$

Table 2.2: Units derived from the Lennard-Jones system for 3 dimensions.

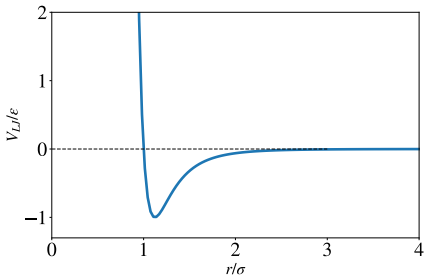

Figure 2.5: Plot of the Lennard-Jones potential.

The challenge is now to efficiently determine the neighbors. Since particles only interact with others within a distance $r < r_{\text{cut}}$, a widely used approach is to employ neighbor lists. One common method is the *Verlet list*, in which each particle keeps a list of neighbors within a distance $r_{\text{cut}} + r_{\text{skin}}$ [75, 76]. This list can then be used for multiple timesteps, as long as the particles do not move too fast.

Another approach which increases the efficiency of this algorithm is the *Cell-linked list*. In this approach, the entire simulation box is divided into subboxes. The neighbors of a given particle are then searched for only within its own subbox and the adjacent ones.

In the next step of the simulations, Newton's equations of motion are solved:

$$m_i \cdot \ddot{\underline{r}}_i = \underline{f}_i \text{ and } \underline{f}_i = -\nabla V(\underline{r}_i) \tag{2.2.5}$$

The solution method is based on a finite-difference scheme, and in fact, many algorithms from numerical mathematics could be used to

solve such a problem [77]. However, the algorithms employed in this context must satisfy certain conditions, such as the conservation of physical laws, even when relatively large timesteps are used. Popular algorithms include the Störmer-Verlet method [78, 79], the Leap-frog algorithm [80] and the Velocity-Verlet integration scheme [81, 82].

The basic idea of all these algorithms is that the position $\underline{r}$, velocity $\underline{u} = \dot{\underline{r}}$ and acceleration $\underline{a} = \dot{\underline{v}}$ can be expanded in Taylor-series:

$$\underline{r}(t+\Delta t) = \underline{r}(t) + \Delta t \cdot \underline{u}(t) + \frac{1}{2}(\Delta t)^2 \cdot \underline{a}(t) + \frac{1}{6}(\Delta t)^3 \cdot \dot{\underline{a}}(t) + \frac{1}{24}(\Delta t)^4 \cdot \ddot{\underline{a}}(t) + ... \tag{2.2.6a}$$

$$\underline{u}(t+\Delta t) = \underline{u}(t) + \Delta t \cdot \underline{a}(t) + \frac{1}{2}(\Delta t)^2 \cdot \dot{\underline{a}}(t) + \frac{1}{6}(\Delta t)^3 \cdot \ddot{\underline{a}}(t) + ... \tag{2.2.6b}$$

$$\underline{a}(t+\Delta t) = \underline{a}(t) + \Delta t \cdot \dot{\underline{a}}(t) + \frac{1}{2}(\Delta t)^2 \cdot \ddot{\underline{a}}(t) + ... \tag{2.2.6c}$$

$$\dot{\underline{a}}(t+\Delta t) = \dot{\underline{a}}(t) + \Delta t \cdot \ddot{\underline{a}}(t) + ... \tag{2.2.6d}$$

The idea of the Störmer-Verlet algorithm is then to evaluate $\underline{r}$ at $t + \Delta t$ and $t - \Delta t$:

$$\underline{r}(t+\Delta t) = \underline{r}(t) + \Delta t \cdot \underline{u}(t) + \frac{1}{2}(\Delta t)^2 \underline{a}(t) \tag{2.2.7a}$$

$$\underline{r}(t-\Delta t) = \underline{r}(t) - \Delta t \cdot \underline{u}(t) + \frac{1}{2}(\Delta t)^2 \underline{a}(t) \tag{2.2.7b}$$

Adding up these equations, one gets:

$$\underline{r}(t+\Delta t) = 2\underline{r}(t) - \underline{r}(t-\Delta t) + (\Delta t)^2 \underline{a}(t) \tag{2.2.8}$$

One disadvantage of this algorithm is that the velocities are not directly accessible, as they are eliminated in the integration scheme. If needed, they can be reconstructed using $\underline{u}(t) = \frac{\underline{r}(t+\Delta t) - \underline{r}(t-\Delta t)}{2\Delta t}$.

One modification of this algorithm is the Leap-frog algorithm, which

calculates the velocities at different times than the positions:

$$\underline{r}(t+\Delta t) = \underline{r}(t) + \Delta t \cdot \underline{u}\left(t + \frac{1}{2}\Delta t\right) \tag{2.2.9a}$$

$$\underline{u}\left(t + \frac{1}{2}\Delta t\right) = \underline{u}\left(t - \frac{1}{2}\Delta t\right) + \Delta t \underline{a}(t) \tag{2.2.9b}$$

Another modification is the Velocity-Verlet algorithm, which obtains positions and velocities at the same times:

$$\underline{r}(t+\Delta t) = \underline{r}(t) + \Delta t \underline{v}(t) + \frac{1}{2}(\Delta t)^2 \underline{a}(t) \tag{2.2.10a}$$

$$\underline{v}(t+\Delta t) = \underline{v}(t) + \frac{\Delta t}{2}[\underline{a}(t) + \underline{a}(t+\Delta t)] \tag{2.2.10b}$$

Finally, one integration method, which also has a very high accuracy, is the Gear-predictor method. This method essentially consists of 3 steps. First, on the basis of the current positions, one makes a prediction of the new positions, velocities and accelerations a^P, using standard Taylor-expansions, see formula 2.2.6a. Secondly, using the new positions, one then calculates the new forces and the corresponding accelerations a^C. One can then define an error as

$$\Delta a(t+\Delta t) = a^c(t+\Delta t) - a^p(t+\Delta t) \tag{2.2.11}$$

Thirdly, the predicted positions are corrected according to the calculated error. A more in-depth discussion of this method can be found in [83–86].

The numerical integration of these classical equations of motion conserves the total energy of the system, which means that a microcanonical ensemble is simulated (particle number N, volume V and energy E are conserved). Nevertheless, it is often an aim to obtain thermodynamic variables corresponding to a different ensemble. For example, one may wish to couple the simulation to a heat bath at temperature T or to a piston at pressure P [87].

One simple method to couple the system to a heat bath is *velocity rescaling*. The idea is to introduce a scaling factor λ and, at each

timestep, scale the velocities of all particles by this factor:

$$u_i^{\text{new}} = \lambda v_i^{\text{old}} \tag{2.2.12}$$

while the scaling factor is obtained by the temperature of the bath T^{bath} and the temperature of the system $T(t)$:

$$\lambda = \sqrt{\frac{T^{\text{bath}}}{T(t)}} \tag{2.2.13}$$

One should note that this method is rarely used in MD simulations, as with this algorithm all fluctuations in the kinetic energy are suppressed.

Using the *Berendsen thermostat* [88], one modifies the scaling factor λ to solve the above mentioned problems. In this approach, we suppose, that the system is coupled to an external bath. Hence, the change of the temperature can be formulated as

$$\frac{\partial T(t)}{\partial t} = \frac{1}{\tau}(T_{\text{bath}} - T(t)) \tag{2.2.14}$$

using τ as the user defined strength of coupling. The scaling factor λ can then be written as

$$\lambda = \sqrt{1 + \frac{\Delta t}{\tau}\left(\frac{T_{\text{bath}}}{T(t)} - 1\right)} \tag{2.2.15}$$

Here, one can see that for a weak coupling (large τ), we do not scale the velocities anymore.
Another thermostat was proposed by *Andersen* [89], who made use of the idea of random collisions. The particles' trajectories are integrated, at each timestep random atoms are chosen. These atoms get a new velocity from the Maxwell-Boltzmann distribution of the desired velocity. The time interval Δt between two velocity reassignments of the same atom follows a Poisson distribution

$$P(\Delta t) = \nu \cdot e^{-\nu \cdot \Delta t} \tag{2.2.16}$$

where ν is the coupling strength to the bath.
One popular way to couple the system to a temperature bath is the use of the *Nosé-Hoover-thermostat*, introduced by Nosé [87] and Hoover [90]. The idea is to introduce an additional variable to couple the system to the heat bath. One gets the Nosé-Hoover equations of motion as:

$$\dot{\underline{r}}_i = \underline{v}_i \tag{2.2.17a}$$

$$\underline{u}_i = \frac{\underline{f}_i}{m_i} - \zeta \cdot \underline{u}_i \tag{2.2.17b}$$

$$\dot{\zeta} = \frac{1}{Q}\left(\frac{\sum_i m_i \underline{u}_i}{3Nk_BT} - 1\right) \tag{2.2.17c}$$

Here ζ and Q are the parameters, which couple the system to the bath. Similarly, one can couple the system to a pistol, i.e. a fixed pressure. Here, instead of scaling the velocities, we scale the volume and the positions respectively:

$$V^{\text{new}} = V^{\text{old}} \cdot \lambda \tag{2.2.18}$$

$$r_i^{\text{new}} = r_i^{\text{old}} \cdot \lambda^{1/3} \tag{2.2.19}$$

The *Berendsen barostat*, for example, is completely analogous to the above mentioned Berendsen thermostat. One assumes that the time evolution of the pressure is given by

$$\frac{\partial P(t)}{\partial t} = \frac{1}{\tau}\left(P_{\text{bath}} - P(t)\right) \tag{2.2.20}$$

and the corresponding scaling is given by

$$\lambda = \left(1 - \frac{k \cdot \Delta t}{\tau}(P(t) - P_{\text{bath}})\right) \tag{2.2.21}$$

where we introduced k, a constant specifying the compressibility of the substance.
The approach of the *Andersen barostat* consists of scaling all the positions with the volume: $\underline{r}_i = V^{1/3}\underline{s}_i$. With this, one can introduce

a new Lagrangian, which also models the movement of the volume V:

$$\mathcal{L} = \sum_i \frac{1}{2} m_i (V^{2/3} \underline{s}_i^2) - V(\underline{r}^N) + \frac{W}{2}\dot{V} - P_{\text{bath}} \cdot V \tag{2.2.22}$$

The parameter W is here control parameter of the coupling to the bath. Finally, the *Parrinello-Rahman barostat* [91] is a generalization of this barostat, which can also deal with different box geometries (which for example occur under shear). Here, the box is written as a matrix

$$h = [\underline{abc}] \tag{2.2.23}$$

and the particle positions are rescaled as $\underline{r}_i = h\underline{s}_i$. Then, the Lagrangian can be written as

$$\mathcal{L} = \sum_i \frac{1}{2} m_i \underline{r}_i^T \underline{r}_i - V(\underline{r}^N) + \frac{W}{2}\text{Tr}(\dot{h}^T \dot{h}) - P_{\text{bath}} \cdot \det(h) \tag{2.2.24}$$

Since usually, the particle numbers that can be achieved by MD simulations are much smaller than the particle number in a real experiment, one often makes use of the concept of periodic boundary conditions. This means that the small simulation box is replicated in all directions and if a particle leaves the box on one side, it is replicated on the other side. To avoid artificial interactions of a particle with itself, one should always make sure that the interaction cut-off distance is smaller than the half-size of the simulation box.

Furthermore, as the procedure consists only of integrating the classical equations of motion, quantum effects are obviously neglected. This is justified by the de-Broglie wavelength, which should be much smaller than the characteristic length to neglect quantum effects. In liquids, the characteristic length scale can be set to $3 - 4$Å [51, 92]. The de-Broglie wavelength is defined as [93]

$$\lambda_{\text{Br}} = \frac{1}{\sqrt{\text{mT}}} 10^{-22} \text{m}\sqrt{\text{kgK}} \tag{2.2.25}$$

For water at ambient conditions ($m = 2.99 \cdot 10^{-26}$kg, $T = 300$K), the de-Broglie wavelength is consequently 0.33Å, which is much smaller than the characteristic wavelength.

2.2.1.2 Initialization

As shown in figure 2.4, before starting the simulation, one first has to initialize the system. For simulations of solids, the positions of the particles are normally the ones of the associated crystal structure. For simulations of liquids, one either takes a crystal structure or a random configuration of atoms. Particles are in this context assumed to be spherical point masses.

The velocities are normally chosen such that the kinetic energy of the system fits to the desired temperature: The kinetic energy E_{kin} and the temperature T are related via the equipartition theorem of classical statistical mechanics, namely $E_{\text{kin}} = \frac{3}{2} N k_B T$ and the kinetic energy of the system can be calculated via $E_{\text{kin}} = \sum_i^N \frac{m_i u_i^2}{2}$. Velocities are normally set according to the Boltzmann distribution: $P(u_i) = \left(\frac{m_i}{2\pi k_B T}\right)^{1/2} e^{-\frac{m_i u_i^2}{k_B T}}$. One should notice that most of the observables should be measured in equilibrium. Hence, before starting the so-called production run, in which the observables are measured, one has to run an equilibration. The equilibration should normally take around $10 - 50$ relaxation times of the liquid. Here, the relaxation time is defined as the time, for which the intermediate scattering function is approaching 0. The (self) intermediate scattering function is defined as the correlation function between Fourier-transformed densities and can be written as

$$F(\underline{k}, t) = \frac{1}{N} \cdot \langle \sum_{i=0}^{N} e^{i\underline{k}(r_i(t) - r_i(0))} \rangle \tag{2.2.26}$$

Here, we use $\underline{k}$ as a wavevector, and N as a number of particles.

2.2.1.3 Evaluation of quantities

In nearly all applications of MD-simulations, one wants to extract some observables from the obtained trajectories. In this section, we briefly explain the quantities, which are used in the scope of the thesis. To calculate the viscosity, one can can make use of the Green-Kubo-approach, evaluating the off-diagonal components of the stress tensor [69]:

$$\eta = \frac{V}{k_B T} \int_0^\infty dt \langle \sigma_{xy}(t_0) \cdot \sigma_{xy}(t_0 + t) \rangle \tag{2.2.27}$$

In an isotropic liquid, the different off-diagonal components xy, xz, and yz, can be used equally, and averaged over to improve the statistics.
In systems with a free surface, the surface tension can be calculated by using the anisotropy of the stress tensor [94, 95]:

$$\hat{\sigma} = \frac{1}{2} \int dz \left[p_z(z) - \frac{1}{2}(p_x(z) + p_y(z)) \right] \tag{2.2.28}$$

Similarly, the surface tension can be estimated from the width of the density profile by fitting the fluid's density distribution to

$$\rho(z) = \frac{\rho_0}{2} - \frac{\rho_0}{2} \cdot \tanh\left(\frac{2(z - z_0)}{\Delta} \right)$$

and using the relation [96]

$$\Delta^2 = \Delta_0^2 + \frac{k_B T}{2\pi\hat{\sigma}} \ln\left(\frac{L}{B_0} \right) \tag{2.2.29}$$

Here, B_0 is a characteristic length scale, and L is related to the system size.

2.2.1.4 Modeling a Glass-Forming Fluid

In this thesis, we focus on the description of glass-forming liquids. A glass-forming fluid is characterized by avoiding crystallization when

it is cooled down. Instead of forming crystals, it becomes more and more viscous. When the viscosity exceeds a certain threshold, the fluid is called a glass, and the corresponding temperature is called glass-transition temperature. An important aspect of the glass transition is that it is not s sharp transition (like for example crystallization), but the viscosity is continuously increasing. The molecular mechanism behind this phenomenon is still not understood [97–99].

A widely used model in this context is the Kob-Andersen binary Lennard-Jones mixture, introduced by Walter Kob and Hans C. Andersen in 1994 [100]. The system consists of two particle species, A (80%) and B (20%), interacting via the LJ-potential with a cutoff radius of $r_{\text{cut}} = 2.5$. The interaction parameters are chosen asymmetrically in order to avoid crystallization, namely

$$\frac{\epsilon_{AB}}{\epsilon_{AA}} = \frac{\epsilon_{BA}}{\epsilon_{AA}} = 1.5, \quad \frac{\epsilon_{BB}}{\epsilon_{AA}} = 0.5, \quad \frac{\sigma_{AB}}{\sigma_{AA}} = 0.8, \quad \frac{\sigma_{BB}}{\sigma_{AA}} = 0.88.$$

In the canonical (NVT) ensemble, the density is typically fixed at $\rho = 1.2$. Under these conditions, the glass transition temperature is found to be at $T \approx 0.435$. This model will be employed in Chapter 4 and Chapter 5.

One of the key features of the Kob–Andersen mixture is its strong tendency to avoid crystallization upon cooling, which makes it a prototypical glass-former. The model has been extensively used to investigate the glass transition and, for instance, to test predictions of Mode-Coupling Theory, which is a first-principle theory for the description of the glass-transition [64].

2.2.1.5 Simulation Setups

In this thesis, we make use of different simulation setups. In chapter 4, we investigate the influence of shear-rate on the surface tension. To model a free surface, the system is first equilibrated in bulk under periodic boundary conditions. After that, the simulation box is extended in the z-direction, thereby creating a free surface. This approach is similar to the ones used in [101–103].

Additionally, we impose a shear-rate on the system. This is done by deforming the simulation box, using the SLLOD-equations [104–108]. With these equation, it is possible to perform non-equilibrium molecular dynamics simulations. The equations of motion in this case are given by

$$\dot{\underline{r}}_i = \underline{u}_i + \underline{r}_i \cdot \nabla \underline{u} \tag{2.2.30}$$

$$\dot{\underline{u}}_i = \underline{F}_i^{(V)} - m_i \underline{u}_i \cdot \nabla \underline{u} - \zeta m_i \underline{u}_i \tag{2.2.31}$$

Here, $\nabla \underline{u}$ is the velocity-gradient tensor, and $\underline{F}_i^{(V)}$ represents the force arising from the intermolecular potential. Here, the terms, which include $\nabla \underline{u}$ couple the motion to the shear, while the term $\zeta m_i \underline{u}_i$ is a thermostat term to control the temperature. The latter one is needed as the shear in principle could heat the system.

In chapter 5, we model a fluid, which is confined in a nanochannel. Here, the setup is chosen, such that the wall atoms form a bcc-crystal, and are interacting via tethering potentials, which bound them to their lattice positions. The interaction of the walls plays a large role for the density profile and it turns out that near the wall, one can observe oscillations in the density profile [109].

2.2.1.6 Accelerating the simulations by GPUs

In the procedure of the MD-simulations, many coupled differential equations have to be solved every timestep. Because of this, both the number of particles and the number of timesteps is limited.

Increasing computational power makes it possible to let the systems grow and grow. For example, in 2013, the SuperMUC supercomputer was able to simulate a system of $4.2 \cdot 10^{12}$ particles, using $40s$ of wall-time per timestep [110].

However, in our applications, we normally do not have the challenge of having as many particles as possible, but of reaching realistic timescales. This is, where GPUs come to play: With the software

"Roskilde-University Molecular Dynamics (RUMD)", a predecessor of *gamdpy*, which is used in this thesis, Bailey et. al were able reach $2 \cdot 10^4$ integration time steps per second, using a relatively small system of 10^3 particles [111]. This is the reason why we used *gamdpy* [112].

GPUs in general consist of many cores, which are optimized for parallel numerical calculations. This is exactly what is used during a MD simulation: There, one wants the integration step to be done for every particle. Hence, if every thread calculates the interaction of one particles and we have very many threads, we get an enormous acceleration of the code.

2.2.2 Macroscopic simulations of the Navier-Stokes equation

In chapter 3, we show simulation results, obtained from simulations done with the open-source software BASILISK C [113]. The aim of this section is to briefly discuss the main features of the numerical scheme, which is used there.

2.2.2.1 Solving the Navier-Stokes equation

In a first step, the domain, on which the Navier-Stokes equation should be solved numerically, is discretized. This is done by using square (or in 3D cubic) finite volumes. To increase the efficiency, they are organized as a quadtree (or octree in 3D). In fact, this means that the the finite volumes do not all have the same side length, such that domains with a more complex flow are treated more accurately.

To model multiphase flow, one makes use of the VOF type approach. This means that every finite volume is assigned to a number $a \in [0, 1]$, which represents the volume fraction of the fluid. For example, if a finite volume is completely filled by the fluid $a = 1$, if there is no

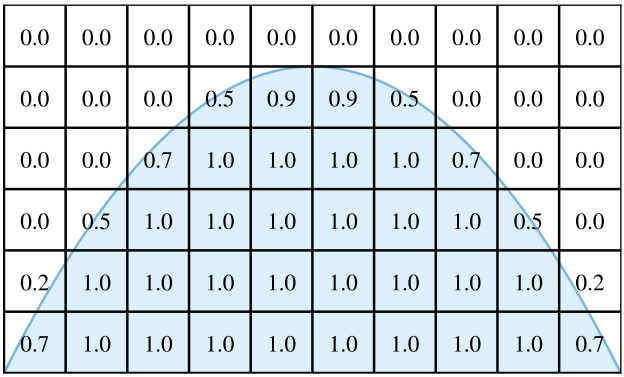

Figure 2.6: Schematic representation of the volume-of-fluid method. The blue area represents the occupation of the fluid. The numbers in the cells correspond to the volume fraction of the fluid in the respective cell.

fluid in it, it is $a = 0$, and if the cell contains the interface $0 < a < 1$. An illustration of this method can be found in figure 2.6.

Time is discretized using a Courant-Friedrichs-Lewy (CFL)-condition [114]. This condition makes sure that the timestep is small enough to obtain numerical stability and it is often used in the field of advection equations. For the general advection equation, describing the quantity q

$$\frac{\partial q}{\partial t} + u\frac{\partial q}{\partial x} = 0 \tag{2.2.32}$$

the condition states that

$$u\frac{\Delta t}{\Delta x} < C \tag{2.2.33}$$

with C being a constant smaller than 1.

The advective part of the Navier-Stokes equation is calculated by the Bell-Collela-Glaz (BCG) advection scheme [115], which is a second order accurate algorithm in space and time. For a detailed

explanation of this method, the reader is referred to Refs. [115, 116]. The principal idea of this scheme is that one wants to solve the (general) advection equation 2.2.32. q_i^n is the cell averaged value of the quantity q in cell i at time t^n.
From a given time n (including q_i^n, u_i^n), we want to determine the values of time $n+1$.

Inside each cell, q is treated as a linear function:

$$q_i(x) = q_i^n + \sigma_i(x - x_i)$$

with a slope, which is obtained by the values of neighbor cells.

$$\sigma_i = \min\left(\frac{q_i - q_{i-1}}{\Delta x}, \frac{q_{i+1} - q_i}{\Delta x}\right)$$

For stability reasons, one always takes the smaller value. Then, a half-time step is calculated using a predictor-corrector approximation:

$$q_{i+1/2}^{n+1/2} = \begin{cases} q_i^n + \frac{1}{2}(1 - C_i)(q_i^n - q_{i-1}^n) & \text{if } u_{i+1/2}^n > 0 \\ q_{i+1}^n - \frac{1}{2}(1 + C_{i+1})(q_{i+2}^n - q_{i+1}^n) & \text{if } u_{i+1/2}^n < 0 \end{cases} \tag{2.2.34}$$

using the Courant-number $C_i = u_i \frac{\Delta x}{\Delta t}$.
In the next step, the numerical flux is calculated as

$$F_{i+1/2} = u_{i+1/2} q_{i+1/2}^{n+1/2}$$

Finally, the cell averages are calculated using the net flux in the cell.

$$q_i^{n+1} = q_i^n - \frac{\Delta t}{\Delta x}(F_{i+1/2} - F_{i-1/2})$$

For the diffusive contributions, one makes use of the implicit viscosity solver [117]. The equation, which should be solved in this part, can be written as

$$\rho \frac{\partial u}{\partial t} = \nabla \cdot [\eta(\nabla u + (\nabla u)^T)] \tag{2.2.35}$$

Discretization and rearranging brings:

$$-\frac{\rho}{\Delta t}u^{u+1} + \nabla \cdot [\eta(\nabla u^{n+1} + (\nabla u^{n+1})^T)] = -\frac{\rho}{\Delta t}u^n$$

With this equation, a linear operator can be defined as

$$L(a) = \nabla \cdot [\eta(\nabla a + (\nabla a)^T)] - \frac{\rho}{\Delta t}a \tag{2.2.36}$$

The problem can be reformulated, using $b = -(\rho/\Delta t)u^n$ as

$$L(u^{n+1}) = b$$

The approach is then not to solve this equation directly, but to take an iterative method. With an initial guess $\tilde{a}$, one calculates a residual

$$\text{res} = L(da) = b - L(\tilde{a}) \tag{2.2.37}$$

If the residual is smaller than a pre-defined threshold, the procedure stops and $\tilde{a}$ is taken as a solution. Otherwise, one solves $L(da) = \text{res}$ and adds da to $\tilde{a}$. The new guess is hence $\tilde{a} + da$.

2.2.2.2 Treatment of viscoelastic fluids

One problem we face in our simulations is the so-called "high-Weissenberg problem" [118, 119], which describes numerical instabilities in the stresses due to high elasticity. To come up with these problems, BASILISK C makes use of the log-conformation-method, explained in Refs. [120, 121]. For implementing this method, one needs to formulate the viscoelastic constitutive equation based on the conformation tensor $\underline{\underline{A}}$ rather than the polymeric stress. The conformation tensor is related to the polymeric stress as follows:

$$\sigma_\text{P} = \frac{\eta_\text{P} f_\text{s}(\underline{\underline{A}})}{\lambda} \tag{2.2.38}$$

Here, we used the polymeric viscosity η_P, and a relaxation parameter λ. The evolution of the conformation tensor is given by the following differential equation:

$$\frac{D}{Dt}\underline{\underline{A}} - \underline{\underline{A}} \cdot \nabla u - \nabla u^T \cdot \underline{\underline{A}} = -\frac{f_{\mathrm{R}}(\underline{\underline{A}})}{\lambda} \tag{2.2.39}$$

using the relaxation function $f_R(A)$.

In our simulations, we make use of the Oldroyd-B-model for which the two functions are given by

$$f_S(\underline{\underline{A}}) = f_R(\underline{\underline{A}}) = \underline{\underline{A}} - \underline{\underline{1}}$$

It is easy to show that in this case, one can combine the equations such that

$$\sigma_{\mathrm{P}} + \lambda(\frac{D}{Dt}\sigma_{\mathrm{p}} - \sigma_{\mathrm{P}} \cdot \nabla u - \nabla u^T \cdot \sigma_{\mathrm{P}}) = 2\mu_{\mathrm{P}}\underline{\underline{\dot{\gamma}}} \tag{2.2.40}$$

The principal idea is then to take the logarithm of the conformation tensor, hence we write:

$$\Psi = \log\Big(\underline{\underline{A}}\Big) \tag{2.2.41}$$

Then, the velocity gradient is decomposed in the following form, using the antisymmetric matrix $\underline{\underline{\Omega}}$:

$$(\nabla \underline{u})^T = \underline{\underline{\Omega}} + \underline{\underline{B}} + N\underline{\underline{A}}^{-1} \tag{2.2.42}$$

Using these definitions, one can write the constitutive law for the logarithm of the conformation tensor as

$$\frac{D}{Dt}\Psi = (\Omega \cdot \Psi - \Psi \cdot \Omega) + 2\underline{\underline{B}} + \frac{e^{-\Psi} f_{\mathrm{R}}(e^{\psi})}{\lambda} \tag{2.2.43}$$

This equation is then solved in 3 steps:

1. Solving the upper-convected part $\partial_t \Psi = 2B + (\Omega \cdot \Psi - \Psi \cdot \Omega)$: In short, this is done by calculating B and Ω, and evaluating $\Delta\Psi = \Delta t[2B + (\Omega \cdot \Psi - \Psi \cdot \Omega)]$. Ψ at the next timestep is then given by $\Psi^{n+1} = \Psi^n + \Delta\Psi$

2. Solving the advection part $\partial_t \Psi + \nabla \cdot (\Psi u)$: This is done by using the Bell–Collela–Glaz scheme, which is explained above.

3. Calculation of model term $\partial_t \underline{\underline{A}} = -\frac{f_r(\underline{\underline{A}})}{\lambda}$: As this term is only available in terms of $\underline{\underline{A}}$, one first has to retransform via $\underline{\underline{A}} = e^{\Psi}$.

Finally, one can get σ_P by inserting in

$$\sigma_{\mathrm{P}} = -\frac{\eta_{\mathrm{P}}}{\lambda} f_{\mathrm{S}}(\underline{\underline{A}}) \tag{2.2.44}$$

and insert the divergence from it into the Navier-Stokes equation. While we have described the log-conformation method for the Oldroyd-B model here, this method can also be applied to other types of constitutive equations that suffer from the high-Weissenberg number problem, see for example [122, 123].

Chapter 3

Spreading droplets of yield-stress fluids with and without gravity

Except for Appendix B, this chapter has been published as Heitmeier, L., D'Angelo, O., Jalaal, M., and Voigtmann, Th. "Spreading droplets of yield-stress fluids with and without gravity." J. Rheol. 70, 631–643 (2026)

We investigate the effect of gravity on the spreading of droplets of yield stress fluids, by performing both microgravity experiments (in a drop tower) and experiments under terrestrial gravity. We study the dependence of the final droplet shape on yield stress and gravity. Droplets are deposited on a thin film of the same material, mimicking a fully wetting surface, and allowing to directly test scaling laws derived from the thin-film equation for viscoplastic fluids, in this limit. Microgravity conditions allow to vary independently the two relevant dimensionless numbers, the Bond number, $\mathcal{B}$, and the plastocapillary number, $\mathcal{J}$, and thus to disentangle the influence of surface tension from that of the yield stress on the final droplet shapes. Simulations using a visco-elastic model with shear thinning

complement the experiments and show good agreement regarding the droplet shapes. Possible deviations arising in the regime of non-negligible elastic effects and large plastocapillary numbers (large yield stress) are discussed.

3.1 Introduction

Yield-stress fluids (YSFs) are characterized by their dual rheological response: they flow like (complex) fluids only when the applied stress exceeds a threshold (the yield stress). Below this threshold, their deformation behavior becomes solid-like [5, 124]. This invites a wide range of applications: many commonly used materials such as pastes, gels, emulsions, foams, and a variety of biological and industrial suspensions exhibit a yield stress [125]. As a result, the spreading of YSFs (and in general non-Newtonian fluids) is central to many processes in sectors including food processing, cosmetics, pharmaceuticals, construction, and energy. For example, the presence of a yield stress in 3D-printing materials ensures that extruded filaments or droplets retain their shape after deposition, enabling the controlled, layer-by-layer fabrication of complex structures [126–130].

Despite this practical importance, some fundamental aspects of the spreading of YSFs have only been established recently [4, 131–139]. A defining characteristic of YSFs is that their droplets reach a finite size even on fully wetting substrates. Unlike Newtonian fluids, which would theoretically spread indefinitely into an infinitesimally thin film, YSFs balance hydrostatic pressure and surface tension against the yield stress, resulting in droplets of finite radius. This principle underpins direct-ink writing technologies, and notably bioprinting [140–142] both on ground and in space [143]. We are therefore interested in how the asymptotic droplet size – achieved at long times, $t \to \infty$ after extrusion – depends on parameters such as the deposited fluid volume, material properties, and gravity.

Since the formation and spreading of YSF droplets is mainly governed by three factors – yield stress, surface tension, and hydrostatic pressure – (at least) two dimensionless groups are needed to characterize their flow properties [4]. The Bond number, $\mathcal{B}$, quantifies the importance of gravity over surface tension, and is well known from the spreading of Newtonian fluids. The existence of a yield stress implies another relevant dimensionless quantity, the plastocapillary

number, $\mathcal{J}$, to quantify the importance of yield-stress effects over surface-tension ones. For a droplet of typical length-scale $\mathcal{L}$ (to be defined more precisely further below) and fluid mass density ρ, one defines

$$\mathcal{B} = \frac{\rho g \mathcal{L}^2}{\hat{\sigma}}\,, \qquad\qquad \mathcal{J} = \frac{\tau_0 \mathcal{L}}{\hat{\sigma}}\,. \tag{3.1.1}$$

Here, τ_0 is the yield stress, $\hat{\sigma}$ the surface tension, and g the gravitational acceleration.

Specifically, scaling laws were derived for the standard viscoplastic Bingham model [4] that predict the asymptotic droplet final radius, R, as a function of the dimensionless numbers $\mathcal{B}$ and $\mathcal{J}$.

A particularly intriguing aspect of these laws is the emergence of distinct scaling exponents when $\mathcal{B} = 0$, highlighting this regime as one where further experimental studies are desired.

To vary the dimensionless numbers $\mathcal{B}$ and $\mathcal{J}$, the length scale $\mathcal{L}$ is arguably the parameter that is most easily changed in Eqs. (3.1.1). However, this does not allow to change both numbers independently. Especially realizing the limit $\mathcal{B} \to 0$ *via* $\mathcal{L} \to 0$, *i.e.* in infinitely small droplets, implies both $\mathcal{J} \to 0$ and obvious experimental limitations. To access a broader range of the parameter space and vary $\mathcal{B}$ and $\mathcal{J}$ independently, we opt to vary the effective gravitational acceleration, g. This allows us to probe the limit $\mathcal{B} \to 0$ while keeping $\mathcal{J}$ finite.

The study of droplets in the regime $g \to 0$ has hitherto mostly focused on Newtonian fluids. Surface tension measurements on droplets under such effective microgravity conditions have a long-established history [144]. Sessile droplets have also been studied at $g \to 0$ to asses variations in contact angles and wettability [145–148]. The coalescence of sessile water drops has been studied on the International Space Station (ISS), investigating the contact line motion at small Bond numbers, while taking advantage of the enhanced optical resolution brought by large droplets [149, 150].

Non-Newtonian droplet studies in the limit $g \to 0$ have been proposed as a promising way to investigate fluid parameters, such as surface tension and viscosity, by means of levitation and droplet oscillations [151]. However, to date, nearly all studies have been conducted under Earth gravity, primarily focusing on the spreading of sessile and impacting droplets [133, 152–155]. More applied studies include experimental setups mimicking inkjet printing [156] or Leidenfrost droplets [157].

We present results from microgravity experiments, that is, experiments performed in a freely falling setup where gravitational acceleration effectively vanishes. In this regime, we test the scaling laws for the final droplet radius that were predicted by [4]. While previous experimental and simulation studies have explored these laws [130, 133], the ability to independently vary both $\mathcal{B}$ and $\mathcal{J}$ in our microgravity experiments enables a far more stringent test of the theoretical predictions. Our findings show agreement with the theoretical power laws, including their predicted asymptotic prefactors. Small systematic deviations appear, and we discuss possible reasons in terms of corrections to the surface tension and the influence of visco-elastic effects. Note that the effects of other dimensionless groups might also come into play, like the Ohnesorge and Deborah numbers [133], $Oh = \eta/\sqrt{\mathcal{L}\rho\tilde{\sigma}}$ and $De = \tau\sqrt{\tilde{\sigma}/\rho\mathcal{L}^3}$, with the fluid's (zero-shear) viscosity η and structural relaxation time τ. While we focus on the asymptotic regime where $Oh/\mathcal{J}$ and $De/\mathcal{J}$ can be considered irrelevant, we employ simulations using a shear-thinning pseudo-yield-stress fluid with finite relaxation time,

The paper is organized as follows: we give a brief review of the experimental and computational methods in Sec. 3.2, including the rheological model studied. We present our experimental findings and comparison with simulation in Sec. 3.3, before we conclude in Sec. 3.4. A key point of the microgravity experiments is to significantly expand the accessible parameter regime in the $(\mathcal{B}, \mathcal{J})$ plane; for illustration the range of values covered in our experiments is compared to that of previous ground-based studies [4] in Fig. 3.1.

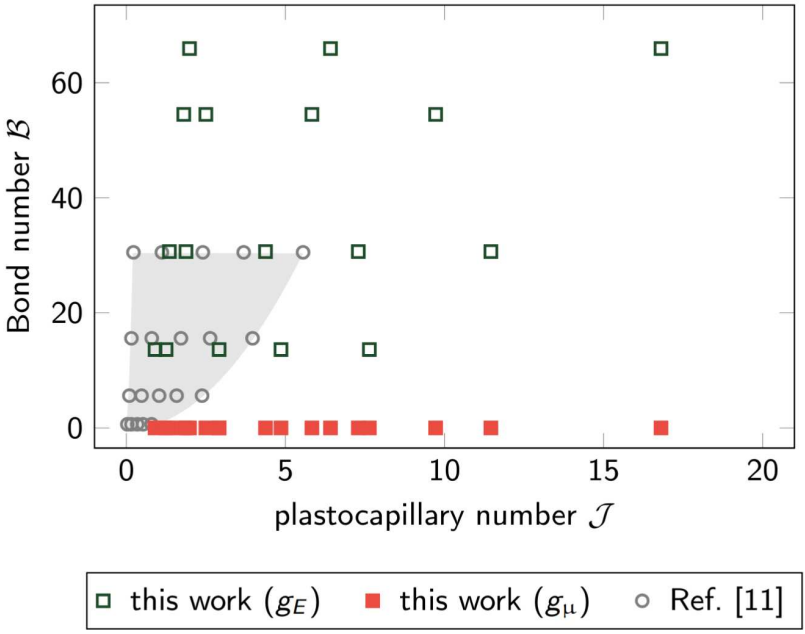

Figure 3.1: Parameter space in terms of Bond number, $\mathcal{B}$, *versus* plastocapillary number, $\mathcal{J}$.Our experiments on ground and in microgravity are represented by open and filled square symbols, respectively; the nominal values of $\mathcal{B}$ and $\mathcal{J}$ are given (see text for details). The parameter space accessed in previous experiments by Jalaal et al. [4] (circle symbols) is indicated by a grey shading.

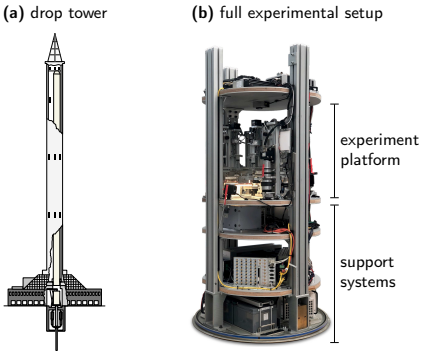

Figure 3.2: Platform used to conduct microgravity experiments. (a) Schematic of the ZARM drop tower, including catapult system below. (b) Full experimental capsule, including experimental platform and support systems. Pictures reproduced from D'Angelo *et al.*, Rev. Sci. Instrum., Vol. 93, Article 115103, 2022; licensed under a Creative Commons Attribution (CC BY) license.

3.2 Methods

3.2.1 Experiments

We conducted microgravity experiments ($g \rightarrow g_\mu \approx 0$) complemented by ground-based experiments (in nominal Earth gravitational acceleration, $g_E = 9.8\,\mathrm{m\,s^{-1}}$). Experimental campaigns were performed at the Center of Applied Space Technology and Microgravity (ZARM) drop tower in Bremen, Germany [158–160] (see Fig. 3.2). Taking advantage of its catapult system, the ZARM drop tower provides a total of 9.3 s of microgravity ($g_\mu < 10^{-4}\,\mathrm{m\,s^{-1}}$). Ground reference experiments were conducted in the same setup, using the same sample batches as the corresponding microgravity experiment, and usually on the same day, a few hours prior. A detailed description of the hardware is provided elsewhere [161]. Below, we summarize the main steps of the experimental procedure.

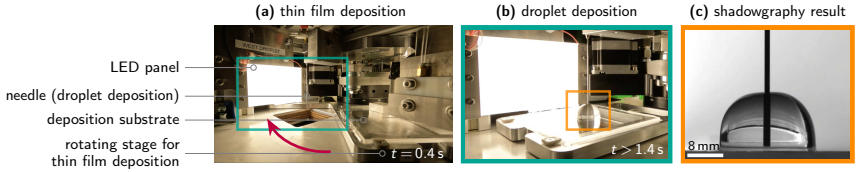

Figure 3.3: Experimental setup and procedure for one droplet. (a) The thin film is deposited by rotating the substrate underneath a disposal blade (red arrow). (b) The droplet is deposited though a needle. (c) Exemplary shadowgraphy result.

The experiment consists of the deposition of a droplet of complex fluid on a pre-wetted glass substrate covered by a thin film of the same fluid (see Fig. A.25). The initial wetting of the substrate is done by rotating a rotary stage onto which the substrate is mounted, underneath a custom-designed nozzle-and-blade system. The latter is designed to cover the glass surface with a thin fluid film. Importantly, for the microgravity experiments, the thin film and droplet are both deposited during the microgravity phase [161]. Subsequently, a droplet is extruded through a nozzle placed in the center of the droplet (inner diameter 0.8 mm, placed at 0.8 mm above the substrate). The glass surfaces are chemically treated to avoid slip [162]. The droplet volume, V, is controlled by a linear motor driving the extrusion syringe. The volumes deposited are $V = 0.5\,\mathrm{mL}$, $1.8\,\mathrm{mL}$, $4.2\,\mathrm{mL}$, and $5.6\,\mathrm{mL}$. Different extrusion speeds were used, but found to have no influence on the asymptotic droplet shapes discussed here. For later reference, unless otherwise specified, we give the corresponding length scale $\mathcal{L}$ as the diameter of a sphere with the same volume, *i.e.*, $\mathcal{L} = (6V/\pi)^{1/3}$. The corresponding values are $\mathcal{L} = 1.0\,\mathrm{cm}$, $1.5\,\mathrm{cm}$, $2.0\,\mathrm{cm}$ and $2.2\,\mathrm{cm}$. We omit the unit when quoting $\mathcal{L}$ values where convenient in the following. Note that, other than in Ref. [4], $\mathcal{L}$ here refers to the diameter of the equivalent sphere rather than its radius.

Pre-wetting takes around 1.4 s, and we find that the droplets attain stationary final shapes well within the remaining microgravity time

label	composition	yield stress
c1	0.3 wt%	6.5 Pa
c2	0.35 wt%	9 Pa
c3	0.4 wt%	14 Pa
c4	0.45 wt%	21 Pa
c5	0.5 wt%	35 Pa
c6	0.55 wt%	55 Pa

Table 3.1: Concentration and yield-stress values of the Carbopol aqueous solutions used in the experiments, with the labels used in the text and figure captions as reference.

for these parameters. While we do not control for evaporation of the liquids, the droplets show no obvious sign of evaporation being relevant over the relatively short time span of the experiments. The video recordings from all experiments are available online [163, 164].

The droplets' spread is measured using shadowgraphy, a straightforward method for extracting the temporal evolution of axisymmetric droplet shapes. For this, the droplet is illuminated from one side using a custom-made LED panel, and observed from the opposite side using a high-speed camera. The resulting images are subject to a standardized image-analysis technique described in Appendix 3.4. We specifically extract the final droplet radius, R, and final height, h, from these images. For the radius, two values are extracted from the left- and right-hand part of the images, and both values are shown to indicate the precision of the measurement.

The complex fluids used as experimental materials are Carbopol aqueous solutions, widely studied as model viscoplastic fluids [4, 5, 165–170]. Six different concentrations (labels c1 to c6) were used, ranging from 0.3 wt% to 0.55 wt%, corresponding to yield stresses, τ_0, between 6.5 Pa and 55 Pa (see Table 3.1 for the precise values).

Experiments cover a large (but not complete) set of combinations of droplet sizes and concentrations. All solutions were produced by dilution from a 1 wt% stock solution. The latter was prepared by

dispersing poly acrylic acid (PAA) powder (Sigma Aldrich) in Milli-Q water using a four-blade marine impeller rotating at 1000 rpm to 1500 rpm at room temperature. The mixture was then pH-neutralized with triethanolamine (TEA; Sigma Aldrich). Bubbles were removed from the sample by centrifuging the fluids at 2200 rpm for 20 min. The yield stress values of the solutions were obtained using an Anton Paar rheometer (MCR-502), measuring flow curves by increasing the shear rate from $0.01\,\mathrm{s}^{-1}$ to $1000\,\mathrm{s}^{-1}$ and fitting a Herschel-Bulkley model through the flow-curve data.

Note that from Eq. (3.1.1) one infers the droplet sizes for which gravitational effects become relevant. This is usually expressed through the capillary length $\ell_\kappa = \sqrt{\hat{\sigma}/\rho g}$, such that $\mathcal{B} = (\mathcal{L}/\ell_\kappa)^2 \gg 1$ if $\mathcal{L} \gg \ell_\kappa$. For a typical liquid density of $\rho \approx 1 \cdot 10^3\,\mathrm{kg\,m}^{-3}$, and with a the surface tension of water, $\hat{\sigma} = 0.072\,\mathrm{N\,m}^{-1}$, as a reference, we obtain $\ell_\kappa \approx 2.7\,\mathrm{mm}$. All our experimental data is in the regime $\mathcal{L} \gg \ell_\kappa$.

3.2.2 Simulations

The experiments are complemented by fluid dynamics simulations, carried out using the open-source software language BASILISK C [113, 171].

In BASILISK, the volume of fluid technique is used to track the interface between the droplet fluid and a surrounding low-density, low-viscosity fluid (representing ambient air). A color function f is used (where $f = 1$ in the liquid and $f = 0$ in the gas), which satisfies the scalar-advection equation. One solves the governing equations using a one-fluid approximation [172, 173], using adaptive mesh refinement based on wavelet estimated discretization errors. The solver has been extensively used for various Newtonian and non-Newtonian problems with deformable interfaces [4, 133, 155, 174–176].

The governing equations are given by the mass-conservation equation for incompressible fluids, $\nabla \cdot \vec{v} = 0$, and the momentum conser-

vation equation,

$$\rho \frac{D}{Dt}\vec{v} = -\nabla p + \nabla \cdot \sigma + \vec{f}_{\text{ext}}\,, \tag{3.2.1}$$

where $\vec{f}_{\text{ext}}$ is an external force density representing gravitational force, if present. For the stress tensor, σ, we use the constitutive equation of a shear-thinning viscoelastic fluid that is representative of a glass-forming fluid with a dynamical yield stress that emerges at the glass transition [177, 178].

Specifically, we set $\sigma = \eta_{\text{N}}\dot{\gamma} + \sigma_p$, where η_{N} is a Newtonian background viscosity, and $\dot{\gamma} = (\nabla\vec{v}) + (\nabla\vec{v})^T$ the symmetrized shear-rate tensor. The non-Newtonian contribution is modeled in a form known as a White-Metzner model from rheology [179, 180],

$$\frac{1}{\tau(\|\dot{\gamma}\|)}\sigma_p + \overset{\triangledown}{\sigma}_p = G_\infty \dot{\gamma}\,. \tag{3.2.2}$$

For fixed relaxation time $\tau = \tau_{\text{eq}}$, this is the standard upper-convected Maxwell model (Oldroyd-B model including the Newtonian background viscosity). The symbol $\triangledown$ indicates the upper-convected time derivative, defined by

$$\overset{\triangledown}{A} = \frac{d}{dt}A - (\nabla\vec{v})^T \cdot A - A \cdot (\nabla\vec{v}) \tag{3.2.3}$$

for a twice-contravariant tensor A such as the stress tensor [181].

The Oldroyd-B model describes viscoelastic stress relaxation: for time scales $t \ll \tau_{\text{eq}}$, the response is that of an elastic solid, while for $t \gg \tau_{\text{eq}}$, viscous flow sets in, with a non-Newtonian contribution to the viscosity $\eta_p = G_\infty \tau_{\text{eq}}$.

To include the effect of shear-thinning, we introduce a shear-rate dependent relaxation rate: We set

$$\tau^{-1} = \tau_{eq}^{-1} + \frac{\|\dot{\gamma}\|}{\gamma_c} \tag{3.2.4}$$

in Eq. (3.2.2). This form is inspired by microscopic approaches to the rheology of glass-forming colloidal suspensions and has been referred to as a "nonlinear Maxwell model" [177, 178]. In the limit $\tau_{\mathrm{eq}} \to \infty$, this model describes a YSF, with a yield stress $\tau_0 = G_\infty \gamma_c$. For finite τ_{eq}, the model describes a quasi-YSF, regularizing the infinite zero-shear viscosity by a finite one. For the numerical simulations considered here, we set $\tau_{\mathrm{eq}} = 50\,\mathrm{s}$, large enough to consider our simulations to be in the YSF regime. Asymptotic droplet shapes are measured in a time window where the initial relaxation of the fluid has passed, but on a time scale $t < \tau_{\mathrm{eq}}$ before viscous relaxation sets in. (See below for specific examples.)

The simulations consider droplet spreading in cylindrical symmetry, assuming the z-axis to be the symmetry axis (and transforming the Navier-Stokes equations into the corresponding coordinate system). Cross-sections are thus obtained in the (x, z)-axis, and gravity, if present, acts in the negative z-direction. The initial conditions are that of a rotation ellipsoid, given by

$$x^2 + (\zeta z)^2 = R_0^2\,, \tag{3.2.5}$$

with $\zeta = 3$ to allow for the relaxation of prolate droplets to flatter shapes. The conversion between experimental values $\mathcal{L}$ and simulated radius R_0 is thus $\mathcal{L} = R_0 \cdot \left(\frac{4}{\zeta}\right)^{1/3}$. Further, a pre-wetted film of thickness $h_\infty = 1\,\mathrm{mm}$ is added to the simulations for numerical stability.

The final heights of the droplets were obtained from an analysis of the long-time behavior of the droplet height $h(t)$: Since the simulations introduce a finite relaxation time τ_{eq}, the final evolution is that of a Newtonian fluid, given by Tanner's law [182], $h(t) \sim t^{-1/10}$. We thus fit the long-time part of the height curve as $h(t) = h_0 - Ct^{-1/10}$ using C and h_0 as fit parameters and the latter as a proxy for the asymptotic droplet height for a true yield-stress fluid.

As further simulation details, the fraction of densities is fixed as $\rho_{\mathrm{air}}/\rho_{\mathrm{fluid}} = 0.001$, and the fraction of Newtonian viscosities

$\eta_{\text{air}}/\eta_{\text{fluid}} = 0.1$. A box of side length $L_x = 0.1\,\text{m}$ (large enough to prevent finite size effects), and a resolution level of 8 for adaptive mesh refinement in BASILISK were chosen for the simulations. The value of the surface tension $\hat{\sigma} = 0.07\,\text{N}\,\text{m}^{-1}$ mimics that of a typical non-surfactant aqueous suspension. For the constitutive equation, Eq. (3.2.2), $\gamma_c = 1/5$ is fixed; this sets a typical strain scale where plastic yielding starts to dominate over elastic response in the model, and values of that order are to be expected on the grounds of microscopic theory [177]. To adjust the yield stress, we vary the Maxwell shear modulus, $G_\infty = 32.5\,\text{Pa}$, $45\,\text{Pa}$, $70\,\text{Pa}$, $105\,\text{Pa}$, $175\,\text{Pa}$, and $275\,\text{Pa}$, such that the simulated fluids have the same yield stress values as determined for the Carbopol solutions used in the experiment. Note that in this model, elasticity and yield stress are linked; the addition of elastic effects is an extension of the simpler Bingham viscoplastic model used in the theory [4]. Our viscoelastic shear-thinning model is also distinct from elasto-viscoplastic models that incorporate an ad-hoc, explicit yield stress, and that have recently been used to study droplet spreading [133].

3.3 Results

3.3.1 Droplet shapes

We begin by analyzing the droplet shapes obtained in the experiments. Figure A.12 shows exemplary height functions obtained from the image analysis, for a fixed concentration (fluid c4, *cf.* Tab. 3.1) and different droplet sizes, for microgravity [Fig. A.12(a)] and Earth gravity [Fig. A.12(b)] experiments. One can observe that the droplet shapes are clearly different depending on g. For the concentration and range of parameters shown in the figure, the droplets in microgravity are taller due to the lack of hydrostatic pressure, and therefore consequently less wide at the same volume than under Earth gravity.

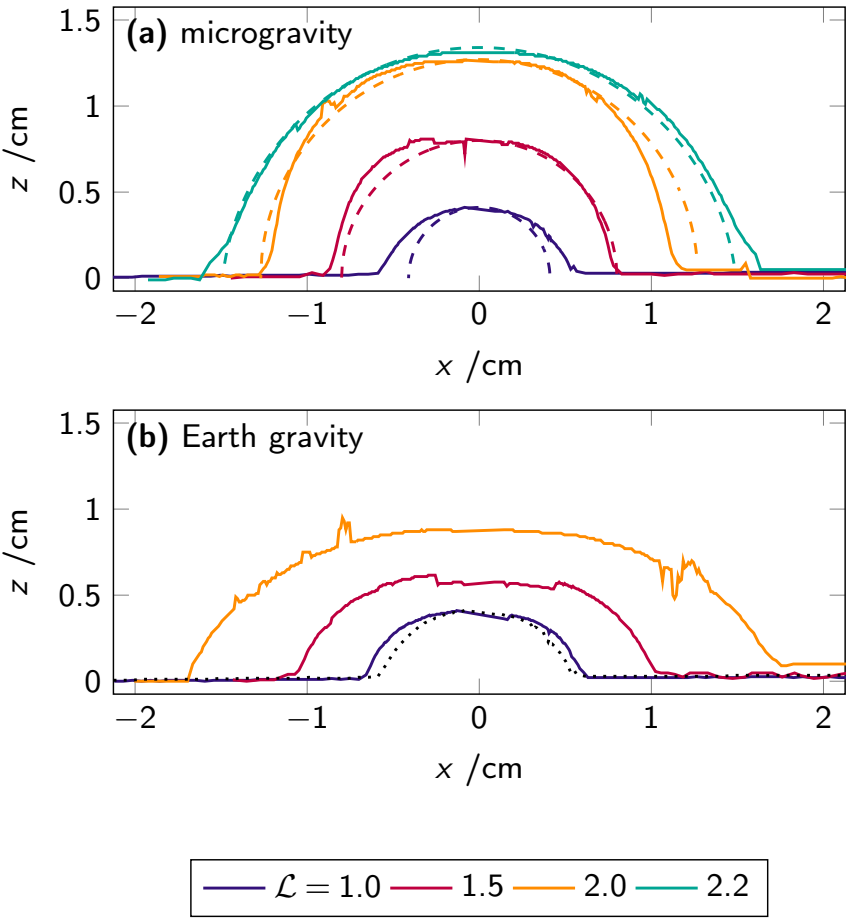

Figure 3.4: Experimental droplet shapes for different volumes ($\mathcal{L} = 1\,\text{cm}$, $1.5\,\text{cm}$, $2\,\text{cm}$ and $2.2\,\text{cm}$ from bottom to top) for concentration c4. Solid lines are reconstructed from image analysis, shown for (a) microgravity experiments and (b) experiments in Earth gravity. (Note that $\mathcal{L} = 2.2\,\text{cm}$ is missing in the latter.) In (a), dashed lines correspond to half-spheres as a comparison. In (b), a dotted line replicates the $\mathcal{L} = 1\,\text{cm}$ result from (a) to ease comparison.

All droplets considered here correspond to non-negligible Bond number. For $\mathcal{L} = 1\,\mathrm{cm}$ (smallest droplet), we get $\mathcal{B} \approx 14$ in Earth gravity, or $\mathcal{B}_h = \mathcal{B}/4^{2/3} \approx 5.4$ if we calculate the Bond number from the expected height of the droplet. Comparing the droplet shapes in g_μ and g_E (Fig. A.12(a) to (b)), we see that in this case, the droplet shapes are still little influenced by g. For larger $\mathcal{L}$, the gravity-induced flattening of the droplets becomes more and more apparent. The largest droplets in microgravity (Fig. A.12(a)) are reasonably close to half-spheres, indicated by dashed lines. However, while this is true for this specific fluid, it does not generalize to other concentrations – we return below to a discussion of the concentration-dependence of droplet shapes.

While the droplet volume is in principle fixed by the automated deposition system, we account for possible deviations in the finally extruded volume. To this end, the droplet cross-sections extracted from the image analysis are numerically integrated to obtain their volume. Assuming cylindrical symmetry around the z axis, we obtain $V_{\mathrm{exp}} = 2\pi \int_{x \gtrless 0} x\, z(x)\, dx$. In the experiments, we confirmed by shadowgraphy also from below for some droplets their cylindrical symmetry (see Appendix 3.4 for details and images). The integral is taken over either positive x or negative x, resulting in two estimates for V_{exp}. Note that the image analysis tends to systematically underestimate $z(x)$: reflections from the light source sometimes cause bright features inside the shadowgraphy projection of the droplet. We thus obtain V_{exp} as the larger of the two integrals. This estimate of the extruded volume defines the experimentally corrected droplet length scale, $\mathcal{L}_{\mathrm{eff}} = (6/\pi)V_{\mathrm{exp}}$.

The resulting $\mathcal{L}_{\mathrm{eff}}$ are compared with the nominal $\mathcal{L}$ in Fig. 3.5. We see that in particular in Earth gravity (open symbols), the reconstructed droplet volumes sometimes show large deviations from the expected ones, droplets often appearing smaller than expected. The microgravity data is much closer to the expected trend.

Discrepancies between $\mathcal{L}$ and $\mathcal{L}_{\mathrm{eff}}$ arise from two main sources apart from poor reconstruction by image analysis. In the experiments,

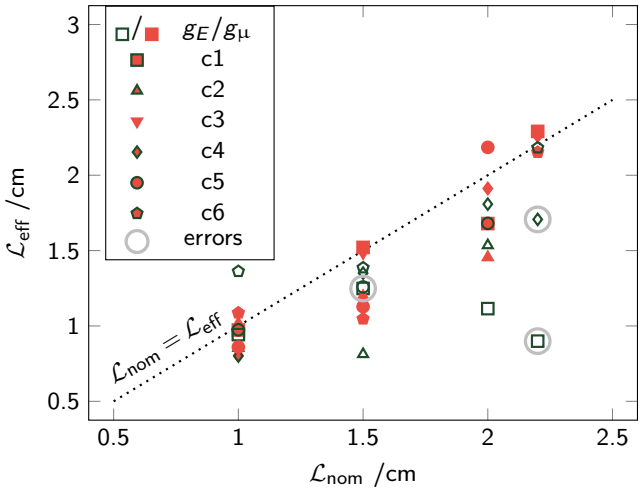

Figure 3.5: Verification of the extruded volumes: equivalent sphere diameter $\mathcal{L}_{\text{eff}} = (6/\pi)V_{\text{exp}}$ from the numerically reconstructed droplet volumes, as a function of their nominal size $\mathcal{L}$. Full symbols correspond to droplets in microgravity experiments, open symbols to those under Earth gravity; symbol shapes indicate the various Carbopol concentrations as labeled. The dotted line is the expected $\mathcal{L}_{\text{eff}} = \mathcal{L}$. Outliers identified from visual inspection of the images are marked with grey circles.

great care was taken to avoid air inclusions in the fluids, and the syringes were driven by precisely controlled linear motors. However, the tubing connecting the syringes and extrusion needles has finite stiffness, which can result in a quantity of extruded material that is lower than expected. There may also be fluid loss into the pre-wetting film. Both these sources of error are compatible with a systematic under-estimation of $\mathcal{L}$.

3.3.2 Scaling laws

[4] derived scaling laws for the dependence of the final droplet radius on the dimensionless numbers $\mathcal{B}$ and $\mathcal{J}$. These scaling laws arise from an asymptotic analysis of the thin-film equations, using the Bingham model as a constitutive equation for the stress tensor. One obtains for the final radius of the droplet

$$\frac{R}{\mathcal{L}} \simeq \begin{cases} \frac{1}{2}\left(\frac{25}{32}\right)^{1/5} \mathcal{B}^{1/5}\mathcal{J}^{-1/5}\,, & \mathcal{B} \gg 1, \\ \beta \cdot \mathcal{J}^{-1/7}\,, & \mathcal{B} \to 0, \end{cases} \tag{3.3.1}$$

with $\beta \approx 0.87$ (converting the results of Ref. [4] to our convention that introduces a factor of 2 in $\mathcal{L}$, as we define $\mathcal{L}$ as the diameter of the equivalent sphere, not its radius). Accounting for conservation of fluid volume, in three dimensions, this implies

$$\frac{h}{\mathcal{L}} \sim \begin{cases} 4\alpha\left(\frac{32}{25}\right)^{2/5} \mathcal{B}^{-2/5}\mathcal{J}^{2/5}\,, & \mathcal{B} \gg 1, \\ \alpha\beta^{-2}\mathcal{J}^{2/7}\,, & \mathcal{B} \to 0. \end{cases} \tag{3.3.2}$$

with a prefactor α that depends on the droplet shape and is $\alpha = (3/2\pi)(\pi/6) = 1/4$ for droplets of ellipsoidal shape with a volume equal to a sphere of diameter $\mathcal{L}$.

These scaling laws are in principle free of fit parameters. However, they require knowledge of the surface tension in the case $\mathcal{B} \to 0$, entering through the definition of the plasto-capillary number $\mathcal{J}$. In the following we assume a fixed value of $\hat{\sigma} = 72\,\mathrm{mN\,m^{-1}}$, assuming

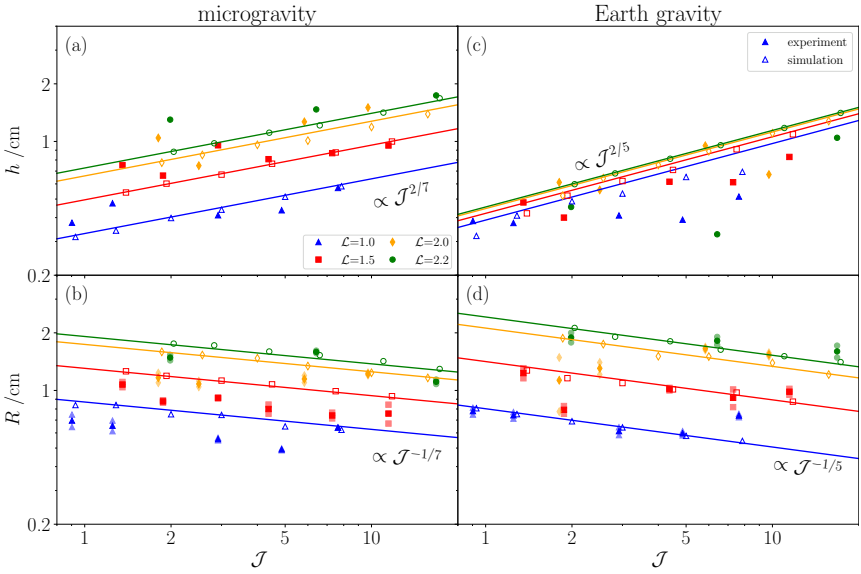

Figure 3.6: Test of the scaling laws of Ref. [4] for final droplet sizes as a function of viscoplastic number $\mathcal{J}$, for different sizes $\mathcal{L}$. Filled symbols correspond to the experimental data ($\mathcal{L}$ = 1.0 cm to 2.2 cm as labeled), open symbols to simulations for height (top row) and radius (bottom row); (a) and (b) refer to microgravity data, $\mathcal{B} \approx 0$, while (c) and (d) refer to data for $\mathcal{B} \gg 1$. Lines in all panels correspond to the expressions given in Eqs. (3.3.1) and (3.3.2); for the height values, hemi-spherical droplets were assumed in evaluating a global prefactor. In (b) and (d) light-filled symbols indicate spearate estimates for the radii to indicate image-analysis error.

that the surface tension of the aqueous solutions is close enough to that of pure water. We will comment on this assumption in Sec. 3.4.

Figure 3.6 shows the experimentally measured heights and radii of the droplets in dependence of the non-dimensional number $\mathcal{J}$. Lines represent the scaling laws. For the case of the droplet radii, the analytically calculated prefactors have been used, thus there are no free fit parameters in this comparison. We observe that all data are compatible with the two predicted power laws, $R \sim \mathcal{J}^{-1/7}$ without gravitational acceleration, and $R \sim \mathcal{J}^{-1/5}$ for the ground experiments. The height data follow the respective power laws, however especially in the ground experiments, stronger deviations are seen, including also the simulation data of $\mathcal{L} = 1\,\mathrm{cm}$. Note that the theoretical predictions for the height have to assume a certain droplet shape, so that potentially some deviations can be attributed to this. Specifically, we assume ellipsoidal shapes as discussed in conjunction with Eq. (3.3.2), $\alpha = 1/4$. Possible sources of error coming from the experiment include the fact that the droplets are extruded through a needle that remains fixed in the center of the droplet. Hence capillary rise of the fluid around the needle cannot be completely avoided. This influences both the droplet height and its determination in image analysis. However, this would likely lead to an over-estimation of the true height, whereas the deviations we observe in Fig. 3.6(c) are systematically towards lower values.

In the data from the microgravity experiments, we observe a systematic deviation most notably in the droplet radii: the experimentally determined values fall below the analytical prediction. This effect had also been seen in Ref. [4] where the limit $\mathcal{B} \to 0$ could only be realized by letting $\mathcal{L} \to 0$. Indeed, also in our microgravity experiments, deviations appear to be most pronounced for the smallest $\mathcal{L}$ [blue triangles in Fig. 3.6(b)], while the $\mathcal{L} = 2.2\,\mathrm{cm}$ data appears to be somewhat closer to the prediction (green circles). However, the quality of our data does not allow to conclude a systematic effect. In the simulations (open symbols) the predicted analytical law is quantitatively fulfilled for all $\mathcal{L}$; this would attribute deviations for small $\mathcal{L}$ in the experiment to the details of the extrusion mechanism

and highlight the difficulty of analyzing small droplets.

Let us investigate the deviations in more detail. Figure 3.7(a) repeats the radii obtained from the microgravity experiments, but in the fully non-dimensionalized form suggested by Eq. (3.3.1), *i.e.*, $R/\mathcal{L}$ as a function of $\mathcal{J}$. This confirms the data collapse predicted by the scaling law to within 20 %, and highlights the systematic overestimation of the radii by the theory.

We do not expect evaporation from the droplet itself to play a significant role. The pre-wetting film, which has a much larger surface area exposed to the ambient atmosphere, is deposited immediately before droplet deposition [161], minimizing possible evaporation time.

Another possible experimental source of error is incomplete extrusion. It is indicated by the fact that we consistently find $\mathcal{L}_{\text{eff}} < \mathcal{L}$ by image analysis (see Fig. 3.5). This is consistent with a systematic deviation towards lower radii. We thus show in Fig. 3.7(b) a comparison of the data from the microgravity experiments to the scaling prediction, where we also correct the nominal droplet sizes $\mathcal{L}$ to the measured ones $\mathcal{L}_{\text{eff}}$ (symbols with error bars). Note that this also shifts the dimensionless numbers to corrected ones, $\mathcal{J}_{\text{eff}}$ (and $\mathcal{B}_{\text{eff}}$ in the presence of gravity). This indeed reduces the deviations to around 15 %, but a systematic difference remains.

Two physically relevant parameters can be considered to contribute to the observed deviation. First, note that in the preparation of the Carbopol suspensions, TEA is added for charge neutralization. TEA can reduce the surface tension of water, by what we estimate to be at most 20% for the low concentrations used [183]. A change in surface tension would introduce a prefactor $\gamma = (\hat{\sigma}'/\hat{\sigma})^{1/7}$ to the scaling law. Indeed such a modified scaling law is compatible with our data (dashed line in the figure), and from a fit we obtain $\gamma \approx 0.87$. This would imply a surface tension reduction from the standard value of water, $\hat{\sigma} \approx 72\,\mathrm{mN\,m^{-1}}$, down to $\hat{\sigma}' \approx 30\,\mathrm{mN\,m^{-1}}$; this is still significantly lower than what one expects from the effect of TEA.

Another source of deviation is suggested by theoretical considera-

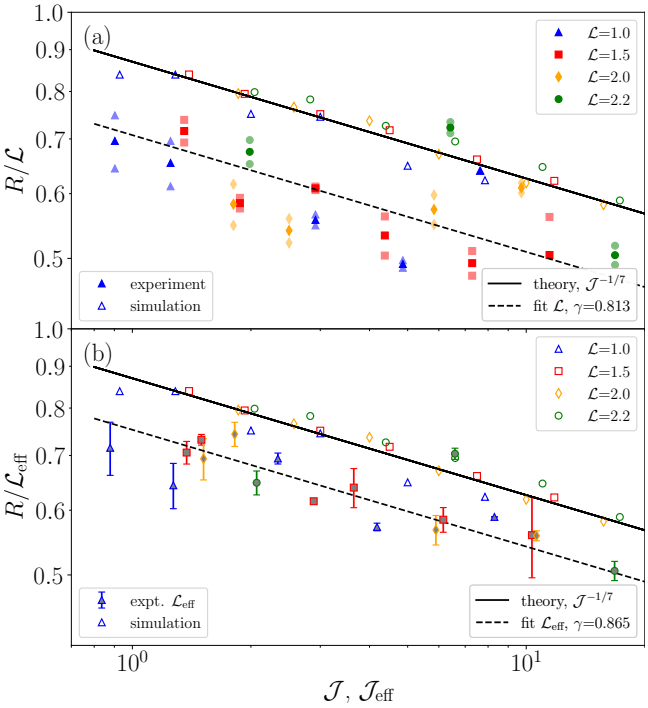

Figure 3.7: Scaling plot for the droplet radii in the regime $\mathcal{B} \to 0$: normalized radii $R/\mathcal{L}$ are shown as a function of the plasto-capillary number $\mathcal{J}$. Filled and open symbols correspond data from microgravity experiments and simulations, respectively. Experimental data is shown using (a) nominal $\mathcal{L}$ and (b) corrected $\mathcal{L}_{\text{eff}}$ accounting for the experimentally extruded volume in separate panels for clarity. A solid line represents the theoretical result, Eq. (3.3.1). Dashed lines represent the theory with an ad-hoc adjusted prefactor as noted in the legend, obtained from a fit of the experimental data.

tions of an elasto-viscoplastic model [133]. There one concludes that elastic effects that are not considered in the Bingham model behind Eq. (3.3.1) should suppress spreading. In the limit of weak elasticity in this model, the leading-order correction can be captured by a reduction of the prefactor of the visco-plastic power law.

Let us note that attributing these deviations to finite elasticity is subtle: our simulations employ a model that also contains elasticity, but in the form of a visco-elastic liquid-material model, with a dynamical yield stress that emerges as the flow rate drops below the relaxation rate of the material. The asymptotic droplet shapes obtained from the model agree well with the prediction based on the Bingham model, except for systematic deviations in the $\mathcal{L} = 1$ case, that can be attributed to the finite h_∞; for a more detailed explanation of the simulation analysis we refer to Sec. 3.3.3 below. In contrast, in Ref. [133], an elasto-viscoplastic solid-material model with a static yield stress was studied. For the model used in the simulations here, no in-depth theoretical analysis is available yet.

Also the gravity-based data collapses onto a master curve. According to Eq. (3.3.1), the normalized radii $R/\mathcal{L}$ become a unique function of $(\mathcal{J}/\mathcal{B})$ for all droplet sizes. This is verified with our data in Fig. 3.8 for which we observe the predicted collapse to within experimental errors. The possible correction to the nominal $\mathcal{L}$ coming from our image analysis plays a sub-leading role here, as both data sets, $R/\mathcal{L}$ as a function of $\mathcal{J}/\mathcal{B}$ (filled symbols in Fig. 3.8), and $R/\mathcal{L}_{\text{eff}}$ as a function of $\mathcal{J}_{\text{eff}}/\mathcal{B}_{\text{eff}}$ (symbols with error bars), do not show any systematic deviation from the prediction.

The shape of the droplets, for fixed volume, depends on their yield stress and on the presence of absence of gravity. We have extracted the aspect ratio of the droplets, $\Phi = h/R$, from the experiments. A value of $\Phi = 1$ indicates a hemi-spherical droplet, while for $\Phi < 1$, droplet shapes are oblate, and $\Phi > 1$ indicates prolate droplets.

Combining the scaling laws, Eqs. (3.3.1) and (3.3.2), one easily obtains analytical predictions for the aspect ratio, $\Phi \sim \mathcal{J}^{3/7}$ for the microgravity case $\mathcal{B} \to 0$, and $\Phi \sim (\mathcal{J}/B)^{3/5}$ in the presence of

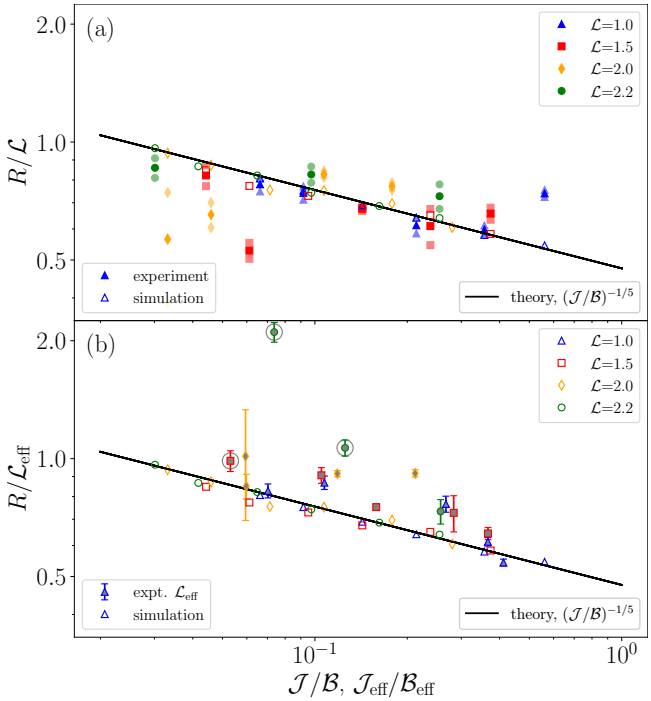

Figure 3.8: Scaling plot for the droplet radii in the regime $\mathcal{B} \neq 0$: normalized radii $R/\mathcal{L}$ as a function of $\mathcal{J}/\mathcal{B}$. Filled and open symbols correspond to data from experiment and simulations, respectively. A solid line represents the theoretical result, Eq. (3.3.1). The two panels show separately the results of scaling (a) with the nominal droplet size $\mathcal{L}$ and (b) with the corrected $\mathcal{L}_{\rm eff}$ (see text). Symbols with enclosing circles indicate outliers as assessed by the quality of the image analysis.

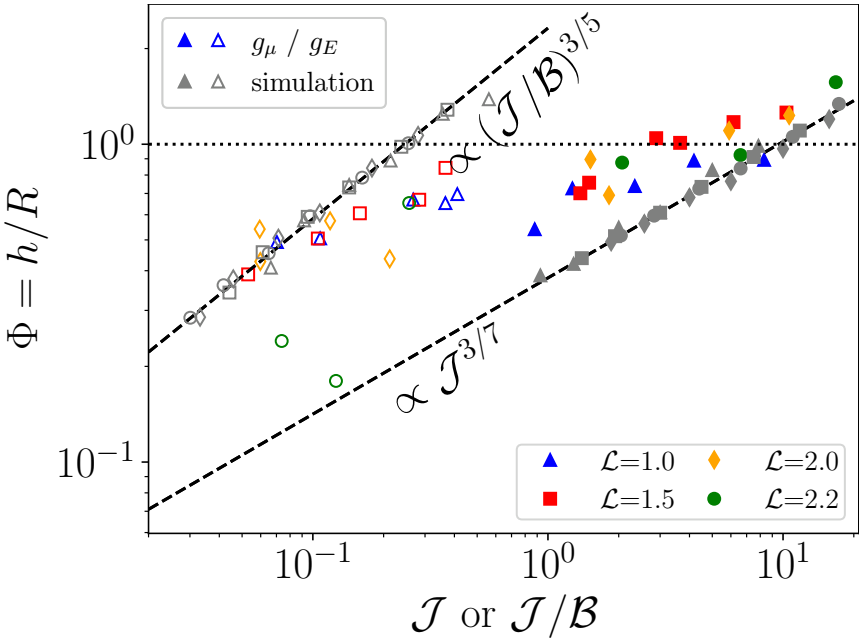

Figure 3.9: Geometrical aspect ratio, $\Phi = h/R$, as a function of the plastocapillary number (for the case in microgravity) and as a function of $\mathcal{J}/\mathcal{B}$ (for the case with gravity). Black dashed lines correspond to the theoretical predictions; a dotted line indicates $\Phi = 1$. Full symbols correspond to data from microgravity experiments, open symbols to those in Earth gravity. Grey symbols represent the simulation results.

gravity, $\mathcal{B} \gg 1$. We show these predictions together with the aspect ratios from our experiments in Fig. 3.9. For the analytical prediction, we assumed ellipsoidal droplet shapes (setting $\alpha = 1/4$) but used no fitting parameter otherwise. Both these asymptotes imply $\Phi \gg 1$ for large enough $\mathcal{J}$. For the microgravity conditions, our experimental values span the regime of both $\Phi < 1$ and $\Phi > 1$. In the ground-based experiments, we observe $\Phi < 1$ for all droplets, *i.e.*, they are all oblate even for those combinations of τ_0 and $\mathcal{L}$ where the scaling laws suggest to reach the regime of prolate droplets also under gravity.

Note that the numbers $\mathcal{J}$ and $\mathcal{J}/\mathcal{B}$ are proportional to the yield stress τ_0. Thus from the droplets' aspect ratio shown in Fig. 3.9, we confirm previous results by [184]: a higher yield stress always increases droplets' aspect ratio. This correlation can be attributed to the fact that a higher yield stress results in a larger immobile regions inside the droplet, which can be lifted up while remaining immobile during deposition. The final droplet shape hence becomes elongated upwards.

3.3.3 Comparison to simulations

Figure 3.10 shows exemplary cases of droplets for $\mathcal{L} = 2.2\,\mathrm{cm}$ and different yield stresses (Carbopol concentrations). In the microgravity experiment one clearly sees the evolution towards more prolate droplets with increasing yield stress.

Also shown in Fig. 3.10 are simulation results for asymptotic droplet shapes (red lines). They confirm that our viscoelastic shear-thinning fluid model is able to capture the specific droplet shapes well. Deviations are seen towards to bottom. But note that the simulations use a rather high background-fluid layer for numerical stability, which results in droplet shapes that are much more "rounded" than the ones in experiment towards the bottom, missing a clearly defined contact line. In fact, in the experiment the apparent contact angles increase with increasing yield stress [161], and they increase in

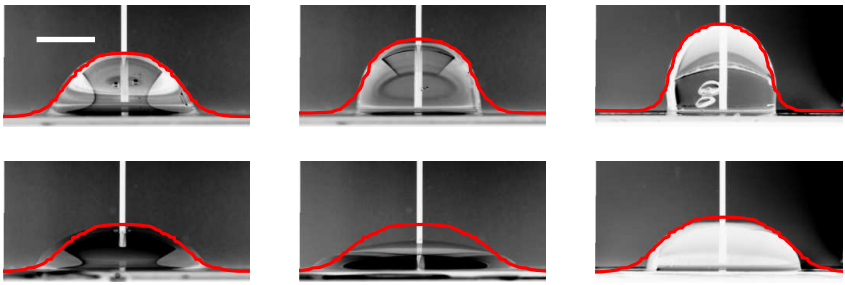

Figure 3.10: Illustration of droplet shapes for droplets with size $\mathcal{L} = 2.2\,\mathrm{cm}$: The top row shows images from microgravity experiments; the bottom row the corresponding results on ground. Different Carbopol concentrations are shown, with increasing yield stress from left to right (concentrations c1, c4, and c6). The white scale bar in the top left panel represents 1 cm. Red lines indicate results from simulations with a shear-thinning Maxwell fluid, using various shear moduli G_∞ to match the experimental yield-stress values. The large deviation in the center bottom panel is attributed to an experimental problem during droplet extrusion.

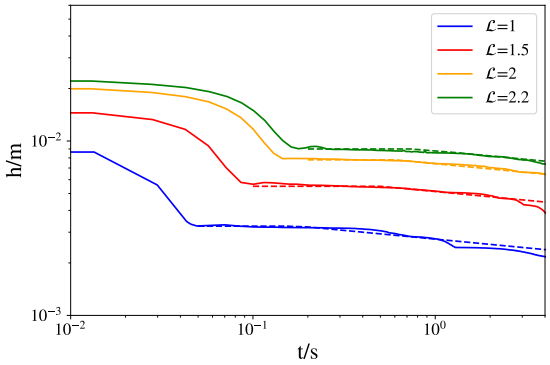

Figure 3.11: Height evolution as a function of time in the simulations; shown for a yield stress of $\tau_0 = 6.5\,\mathrm{Pa}$ (c1), and different droplet sizes $\mathcal{L}$ as labeled. Dashed lines correspond to the fit comprising a yield-stress plateau and the expected $t^{-1/10}$ long-time asymptote (Tanner's law).

the microgravity experiment compared to the one in Earth gravity. For the largest yield stress shown in Fig. 3.10, the apparent contact angle exceeds 90°; an effect not observed in the simulation.

To illustrate how the asymptotic droplet shapes are extracted from the simulation, we show in Fig. 3.11 exemplary results for the evolution of the droplet height in the simulation. Results are shown for fixed yield stress without gravity, and different $\mathcal{L}$. Typically for a visco-elastic fluid model, the height shows an initial decrease at short times, driven by surface tension adjusting the shape of the droplet from the arbitrarily chosen initial configuration. For large droplets, this evolution hints at some oscillations (around $t = 0.2\,\mathrm{s}$ in the figure for $\mathcal{L} = 2.0$ and $\mathcal{L} = 2.2$), indicative of elastic restoring forces. After this initial decay, a plateau is observed in the height-*versus*-time plot. Recall that our model always allows flow on time scales $t \gg \tau$, but acts like a yield-stress fluid for $t \ll \tau$. We thus extract the asymptotic droplet shape that represents the balance of the yield stress with the other forces (surface tension and gravity)

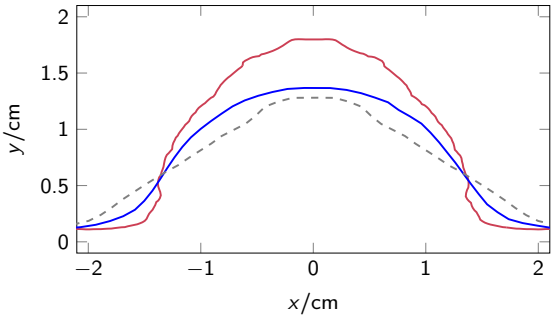

Figure 3.12: Shape of a droplet for $G_\infty = 32.5\,\mathrm{Pa}$ and $R = 0.02m$. Red: simulation results for the case without shear-thinning, blue: simulation results for the case with shear-thinning ($\gamma_c = 1/5$). The case without shear thinning, but effective reduced shear modulus $G_\infty^{\mathrm{eff}} = G_\infty \gamma_c$ is shown as a dashed line for comparison. The red plot exhibits slight wiggles due to the finite numerical resolution.

in the plateau regime that is (within the limits that we checked) independent of the precise initial conditions and not yet affected by the ultimate liquid-like flow of the model.

To unambiguously determine the plateau values, we have fitted the simulation results for $h(t)$ with a combination of a yield-stress plateau and Tanner's law (as described in Sec. 3.2). This is exemplified by the dashed lines in Fig. 3.11. The extraction of a plateau value in this way effectively considers the limit of zero Deborah number (observation time much smaller than the fluid's structural relaxation time).

The simulation allows to address the role of the fluid rheology in determining the droplet shapes. Recall that the scaling laws were obtained for a model viscoplastic fluid, where a yield stress is incorporated in an ad-hoc manner. The good agreement with our simulations of a refined model of a visco-elastic shear-thinning fluid is encouraging: in the asymptotic long-time regime that we analyze,

only the value of the (dynamic) yield stress τ_0 enters.

On purely dimensional grounds, also elastic effects might be considered, *i.e.*, the balance of elastic restoring forces (quantified by the shear modulus G_∞ of the viscoelastic fluid) compared to surface-tension forces. However, the droplet shapes observed in experiment are clearly determined by the dynamic yield stress. To assert this, we compare in Fig. 3.12 droplet shapes obtained from the simulation with and without shear thinning. We observe that the purely viscoelastic droplet (red line in Fig. 3.12) remains taller and less spread compared to the one with shear-thinning: shear-thinning initially aids the flow of the material in response to the surface tension forces. The forces opposing the complete spread of the droplet are then given by the yield stress, $\tau_0 = G_\infty \gamma_c$, and these are not equivalent to a simply reduced elastic force G_∞^{eff}: as the comparison with the model without shear thinning, but $G_\infty^{\text{eff}} = G_\infty \gamma_c$ shows (dashed line), the droplet shapes are not identical with and without shear thinning.

This effect can be understood by recalling that in our model, stress relaxation in the regime $t \ll \tau_{\text{eq}}$ is incomplete. The droplet thus contains inner "residual stresses" that are the result of a dynamical balance between arrested relaxation ($\tau_{\text{eq}} \to \infty$) and shear-thinning effects. As such, the residual stresses are a non-equilibrium phenomenon and can depend on the dynamical pathway of the spreading, and not only on the mechanical balance of elastic forces.

3.3.4 Note on Surface Tension

A potential cause of deviations from the scaling laws could be hidden in the role of the surface tension. In our analysis, we have assumed all our Carbopol solutions to have the same surface tension as water, irrespective of their yield stress. This is in line with recent experiments [185], and the interpretation that Carbopol as a non-surfactant polymer should not drastically change the surface

tension of the solvent. Note however that the determination of surface tension in the presence of a yield stress is intricate [29, 30], as the YSF approaches solid-like behavior and one in principle needs to distinguish surface tension and surface energy.

Making use of the scaling laws for the case $\mathcal{B} = 0$ one could in principle determine the surface tension from a measurement of the droplet radii or heights,

$$\hat{\sigma}_R = \left(\frac{R}{\beta}\right)^7 \mathcal{L}^{-6}\tau_0 \tag{3.3.3}$$

respectively

$$\hat{\sigma}_h = \left(\frac{1}{2\beta\sqrt{h}}\right)^7 \mathcal{L}^{9/2}\tau_0\,, \tag{3.3.4}$$

where $\hat{\sigma}_R = \hat{\sigma}_h = \hat{\sigma}$ holds if the scaling laws are obeyed. In principle, data from microgravity experiments would be uniquely suited to determine $\hat{\sigma}$ this way, because the expected variation with $\mathcal{L}$ can be tested for fixed τ_0 and not leaving the required $\mathcal{B} \to 0$ regime. However, the high powers of R and h entering the equations cause large uncertainties. For our data, the obtained values of $\hat{\sigma}$ are still compatible with the value of the pure solvent.

To illustrate the point, we show in Fig. 3.13 the deviations from the theoretical scaling law in the form $\varepsilon_{\hat{\sigma}} = (\hat{\sigma}_R - \hat{\sigma})/\hat{\sigma}$. Both experimental values, with and without correction for the effective droplet size, are shown alongside deviations observed in our simulations. The latter data indicate the level of accuracy that can be expected if the surface tension is known. One observes that the simulation data has a systematic error of around 10%, slightly increasing with increasing yield stress. Assuming that read-off errors are small in the simulation, this can be interpreted as the influence coming from finite elasticity. The experimental data deviate much more and systematically to lower values. If one were to interpret this as due to an effective surface tension, one would obtain $\hat{\sigma}_h \approx 30\,\mathrm{mN\,m^{-1}}$, relatively independent of the yield stress within errors. Such a strong

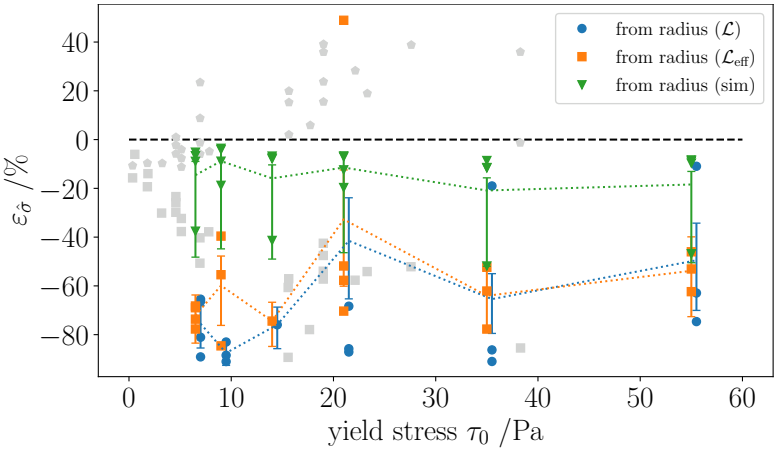

Figure 3.13: Deviation of droplet radius from the viscoplastic scaling law expressed in deviations converted to units of a surface tension, as a function of yield stress. Symbols show results from our microgravity experiments (both using the nominal, $\mathcal{L}$, and the corrected droplet size, $\mathcal{L}_{\text{eff}}$), and from simulation (as labeled in the legend). Dotted lines connect the estimated mean values as a guide to the eye. Gray symbols correspond to values converted from surface-tension measurements of Ref. [30].

decrease of the surface tension in the yield-stress fluid can be regarded as surprising. We note that these values are compatible with those reported earlier from dedicated surface-tension measurements in Carbopol by Jørgensen et al. [30] (gray symbols in Fig. 3.13).

3.4 Conclusion

We studied the spreading of droplets of Carbopol suspensions, a model yield stress fluid, both with and without gravitational acceleration. The droplets spread on a pre-wetted thin film, and eventually attain a finite shape, due to a balance between surface tension, their yield stress, and hydrostatic pressure in the presence of gravity. Conducting microgravity experiments at the ZARM drop tower, we were able to separate the limit $\mathcal{B} \to 0$ from the limit $\mathcal{J} \to 0$ by decoupling $\mathcal{B}$ from the droplet size, $\mathcal{L}$. We could hence verify scaling laws by [4] for both the gravity-dominated case (characterized by finite Bond number, $\mathcal{B} \gg 1$) and the surface-tension dominated case ($\mathcal{B} \to 0$, at finite plastocapillary number $\mathcal{J}$). We complemented our experiments by simulations using a model including a dynamical yield stress together with visco-elasticity, and found that the simulations obey the scaling predictions very well.

The scaling laws predict a power-law dependence of the final droplet size on the plastocapillary number, $\mathcal{J}$. For the experimental droplet radii we find good agreement with the predictions, while the droplet heights show somewhat larger deviations, especially in the gravity-dominated case.

Using a standard viscoplastic constitutive equation, *viz.* the Bingham model, Jalaal et al. also derived the numerical values of the prefactors in the scaling laws. Our experimental results confirm these prefactors, but show that in order to observe them, the limit $\mathcal{L} \to 0$ should be avoided if $\mathcal{B} \to 0$. Systematic deviations could point to finite elasticity effects as discussed more recently by França et al. There, an extension of the Bingham model to include both a

static yield stress and solid elasticity was studied, and corrections to the scaling laws coming from finite Ohnesorge and Deborah number would be compatible with our experimental data. Note however that our simulations show good agreement with the theoretical predictions based on the Bingham model, even though our simulation model includes visco-elastic effects. This is a subtle point: our model is ultimately a liquid-like model, with a regularized dynamical yield stress. The model of França et al. in contrast has a static yield stress and included elasticity in a solid-like model. The connection between these different constitutive modeling approaches will have to be investigated further.

As discussed above, the deviations we observe from the scaling laws in the microgravity case can be connected to previous experimental investigations of yield-stress-induced changes of the surface tension. While the high sensitivity to experimental error prevents definite conclusions, our results still sugest that the role of surface tension in YSF remains to be further explored.

Data Management

The data associated to this study is available on Zenodo repositories 15806543 and 15806731 [163, 164].

Appendix

Appendix A: Data analysis of the experimental data

We briefly summarize our image analysis procedure to obtain the droplet shapes. We analyze the images from the experiment in 5 different steps, as sketched in Figure 3.14.

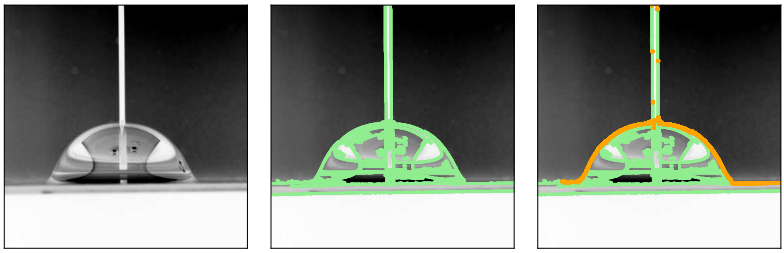

(a) Step 1 (b) Step 2 (c) Step 3

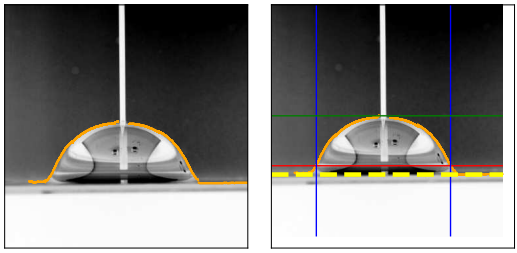

(d) Step 4 (e) Step 5

Figure 3.14: Steps in the image analysis. See text for a description.

From the video recording of the experiment, we extract the raw image of the droplet in the late stage of the experiment (just before impact in the microgravity case), as in Fig. 3.14(a). We first identify all edges in the images with a canny-edge filter (standard OpenCV implementation in python, `cv2.Canny`, using thresholds of 48 % and 52% of the maximal image pixel. This step is illustrated in Fig. 3.14(b). To keep only the outer shape of the droplet, all edges detected inside the droplet (typically from small air inclusions or reflections) are removed. This is done by deleting, for every x-values, every y-value except the highest value. The outer shape of the droplet thus found is marked yellow in Fig. 3.14(c). As the deposition needle, which is part of the experimental images, should not be part of our analysis, we then delete all values which have an

x-value in the range of that of the needle. The resulting image can be seen in Fig. 3.14(d).

Finally, we perform the analysis of the extracted droplet shape. The bottom of the droplet (thin film of pre-wetting fluid), placed at height h_0, is found by taking the minimum value of the y-values of the droplet shape. This is marked by the dashed yellow line in Fig. 3.14(e). The height of the droplet, h, can be extracted by taking the maximum value of the y-values of the droplet's shape. The height of the droplet is drawn as a green line in Fig. 3.14(e). The radius is determined by defining a new height, h_{radius}, given by $h_0 + (h - h_0) \cdot 0.1$, which is drawn in red in Fig. 3.14(e). This rise of 10% of the droplet's height from its bottom allows us to capture the droplets' radii without the wetting angle. We identify the x-values at which the shape of the droplet crosses this point to capture the droplet's extremities (blue lines in Fig. 3.14(e)).

The center of the image is defined by the position of the needle. To convert the values of the heights and radii obtained in image processing, before each experiment calibration images with a 2 mm grid were taken; the resolution of the setup is typically $15\,\text{px}\,\text{mm}^{-1}$.

We verified the circularity of the droplets by pictures taken from below the glass substrate (example in Figure 3.15(a)).

Another concern in the volume reconstruction by image analysis is the fact that light reflections sometimes affect the detection of the droplet's contour. One such example is given in Figure 3.15(b): on the right side of the image, the image analysis algorithm picks up a light reflection instead of the true droplet's shape. In such case, we used the well reconstructed half of the droplet (left half here) and determined its volume by mirroring it.

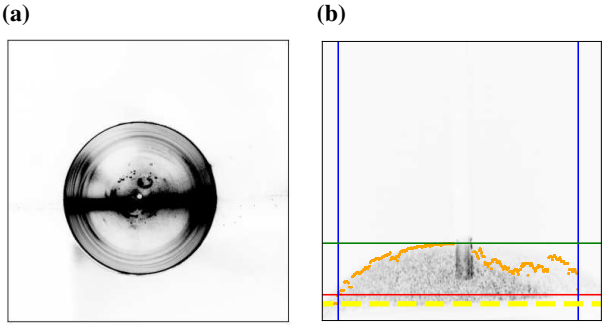

Figure 3.15: Experimental images. (a) Image of a droplet of concentration c4 and size $\mathcal{L} = 2.2$, taken from below. (b) Exemplary image where the shape detection did not work properly.

Appendix B: A thin-film equation for shear-thinning viscoelastic fluids

In this section, we aim to derive a thin-film equation for shear-thinning viscoelastic fluids. The underlying idea behind the derivation of a thin-film equation is described in chapter 2. Instead of taking the constitutive law of a Newtonian fluid, we here describe the fluid as a shear-thinning viscoelastic fluid [43]. Hence, the constitutive law can be formulated as

$$\left(\frac{1}{\tau} + \partial_t\right)\sigma = \eta_N \left(\frac{G_\infty}{\eta_N} + \frac{1}{\tau} + \partial_t\right)\dot{\gamma} \tag{3.4.1}$$

For a more in-depth discussion of this model, the reader is referred to chapter 2.1.1.2.
In contrast to the well-established scaling laws, which were also introduced in chapter 2, in this case it is necessary to introduce two time-scales and treat the two regimes individually. Hence, the time is scaled with T, representing an "inner droplet time", and a timescale T_+, which can be understood as the outer timescale. As for yield-stress fluids, which we aim to describe here, the relaxation time is very large, we can assume that $T < T_+$. In terms of this

new time-scaling, the time derivative is scaled as $\partial_t \to \frac{1}{T}\partial_t + \frac{1}{T_+}\partial_t$. Using this scaling, the xz-component of the constitutive law can be written as

$$\begin{aligned}&\left(\frac{1}{T_+ \cdot \tau} + \frac{1}{T_+}\partial_t + \frac{1}{T}\partial_t + \frac{1}{T}\frac{\sqrt{2}|\partial_z v_x|}{\epsilon\gamma_c}\right) \cdot \frac{\sigma_{xz}}{\epsilon} \\ = &\left(\frac{1}{T}\frac{G_\infty}{\eta_N} + \frac{1}{T_+\tau} + \frac{1}{T_+}\partial_t + \frac{1}{T}\partial_t + \frac{1}{T}\frac{\sqrt{2}|\partial_z v_x|}{\epsilon\gamma_c}\right) \frac{\partial_z v_x}{\epsilon}\end{aligned} \tag{3.4.2}$$

For a further analysis, the two timescales are treated individually. The terms that depend on the timescale T, are given by

$$\left(\partial_t + \frac{\sqrt{2}|\partial_z v_x|}{\epsilon\gamma_c}\right)\frac{\sigma_{xz}}{\epsilon} = \left(\frac{G_\infty}{\eta_N} + \partial_t + \frac{\sqrt{2}|\partial_z v_x|}{\epsilon\gamma_c}\right)\frac{\partial_z v_x}{\epsilon} \tag{3.4.3}$$

To leading order in ϵ, this relation reduces to

$$|\partial_z v_x|\sigma_{xz} = |\partial_z v_x|\partial_z v_x \tag{3.4.4}$$

Hence, we can conclude that in this regime, either $\partial_z v_x = 0$ or $\sigma_{xz} = \partial_z v_x$. Physically speaking, this means that either the droplet's height is not moving, or the droplet is behaving like a Newtonian fluid.
The terms, which are dependent on the timescale T_+ are given by

$$\left(\frac{1}{\tau} + \partial_t\right)\sigma_{xz} = \left(\frac{1}{\tau} + \partial_t\right)\partial_z v_x \tag{3.4.5}$$

This relation also reduces to the constitutive law of a Newtonian fluid. Finally, we can also identify the transition time t_{trans}, where the behavior changes from the regime described by T, and by T_+. At this time, both T, and T_+ are of equal order. From equation (3.4.2), we can infer that at this time scale, it holds that

$$\frac{1}{\tau} \sim \frac{1}{\epsilon\gamma_c} \to \frac{\tau}{\gamma_c} \sim \epsilon \tag{3.4.6}$$

From this estimation, one can conclude that $t_{\text{trans}} \propto \tau$, and $t_{\text{trans}} \propto \gamma_c^{-1}$. This is exactly in agreement with the expected behavior: If

the relaxation time τ is very large, the regime of a constant droplet height is very long. This is in fact what is found by the calculation, using the Bingham-model. Additionally, if the shear-thinning-contribution vanishes, *i.e.* $\gamma_c^{-1} \to 0$, there is no yield-stress anymore, and the regime of constant droplet height disappears. This result also motivated the fit in figure 3.11.

Chapter 4

Shear-rate dependent surface tension of glass-forming fluids

This chapter has been published as Heitmeier, L., and Voigtmann, Th. "Shear-Rate Dependent Surface Tension of Glass-Forming Fluids." Phys. Rev. Lett. 136, 068203 (2026)

We investigate the interface of a glass-forming fluid showing non-Newtonian rheology. By applying shear flow in the interface, we observe that the surface tension depends on the shear rate. Importantly, the standard way of determining surface tension from the pressure anisotropy caused by the interface can give rise to an effective surface tension in the non-Newtonian fluid that mixes bulk and interface properties. We show how the pressure anisotropy can be used to clearly define the bulk and interface regions and extract a genuine shear-rate dependent surface tension. The results have implications for measurement techniques related to interfacial rheology of complex fluids.

The surface of glass-forming fluids is home to many intriguing dynamical phenomena. Glasses are covered by layers of enhanced molecular mobility [186, 187], providing an amorphous analog to surface melting, the physical mechanism conjectured to facilitate ice skating at low temperatures. The highly mobile layers near the surface enable the fabrication by layerwise deposition of ultrastable glasses with unique mechanical properties [188–190], and are a major factor in determining the properties of polymer films [191]. The surface induces a dynamical penetration depth into the bulk that changes non-monotonically with temperature and allows to disentangle the change in mechanisms of relaxation close to a dynamical cross-over temperature T_c [102].

Surface tension is a key parameter characterizing interfaces of complex fluids [192], but not many theoretical studies address it in the dynamical cross-over regime close to the kinetic arrest transition. This is despite the significance in applications for films and coatings, in interfacial rheology in general [24], for certain 3d-printing techniques [193], and also for theoretical concerns: The surface tension of amorphous structures in contact with each other is posited by some theories to play a key role in the dynamical cross-over from supercooled liquid to glass [194, 195].

Glass formers typically are shear-thinning and yield-stress fluids, i.e., their viscosity strongly decreases with the flow rate, and they flow only above a certain threshold stress close to T_c as the structural relaxation rate of the quiescent fluid drops below the imposed flow rate [43, 196]. Reliable experimental data for the surface tension of such non-Newtonian fluids are rare, since the emerging yield stress impedes measurements [30]. Due to the associated slow relaxation time scale of the fluid, typical measurements [29, 30] are prone to hysteresis effects. For example, Jørgensen *et al.* [30] used a liquid-bridge tensionmeter and found the apparent surface tension of carbopol dispersions to be systematically higher in expansion than in compression. They rationalized this finding with an elastoplastic model of the fluid, and attributed it to the existence of a yield stress.

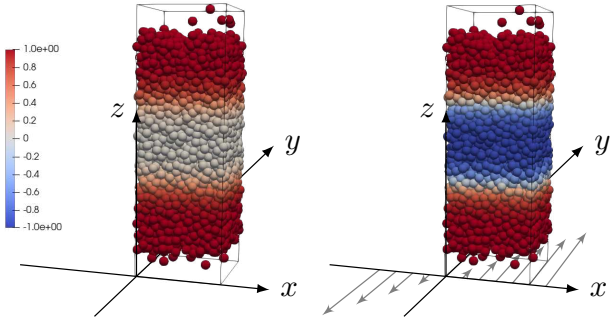

Figure 4.1: Snapshots of the simulation setup without (left) and with (right) imposed shear. Only the central part of the box along z is shown for clarity. We impose 'in-plane' shear, as shown by the arrows in the coordinate system. Particles are colored according to $\Delta p = p_z - (p_x + p_y)/2$ normalized to the interval $[-1, 1]$, see Fig. 4.3.

This poses a number of questions: first, how does the surface tension, a parameter that is typically evaluated from "static" pressure differences across an interface, couple to the non-Newtonian rheology of highly viscoelastic fluids, a typical "dynamic" effect in the bulk? Second, since the bulk rheology of the shear-thinning fluid depends very sensitively on the shear rate, what is the effect of fluid flow on the (apparent) surface tension?

We address these questions by MD simulations of a prototypical model of a glass-forming fluid (involving no polymeric or suspension effects), in a simple setup involving a planar surface. Our simulations reveal how an apparent surface tension arises in non-Newtonian fluids that is a mixture of bulk rheology and genuine surface effects.

We consider the standard Kob-Andersen binary LJ-potential mixture [64] at fixed number density $\rho = 1.2$ using the open-source package LAMMPS [197]. Units of length, σ, time, τ_0, and energy are all in standard LJ-potential units related to the larger particles.

The simulations start from bulk liquids in the NVT ensemble, that are equilibrated at $T_i = 2.0$ for at least $500\tau_0$, cooled to the target temperature T, and then equilibrated again for up to $10^6\tau_0$ (depending on T). We use $N = 5000$ ($N = 10000$) particles corresponding to a cubic box of size $L = L_x = L_y = 13\sigma$ and $L_z = 24.6\sigma$ (49.2σ) for the small (large) system. For the determination of the surface tension from capillary theory, alongside the small system, a wide system with $L = 18\sigma$ with $N = 9564$ particles was used.

After equilibration, the simulation box was enlarged to $L_z = 160\sigma$ keeping the fluid in the center of the box where around $z = 0$, bulk properties are recovered [102]. The interfaces were then relaxed for $250\tau_0$, before measurements were performed. Shear flow with rate $\dot{\gamma}$ is imposed in the (x, y)-plane tangential to the surface (see Fig. A.19) using the SLLOD equations; this is also motivated by the tangential character of the surface tension [95, 198–201]. Note that our shear protocol keeps the total surface area constant, which is conceptually important for viscoelastic fluids [201]. Surface tension values were averaged over at least $2000\tau_0$. Inspection of the z-dependent density profiles revealed no particle-species segregation.

We use two independent methods to determine the surface tension $\hat{\sigma}$: the first is by *ad hoc* extending the expression from equilibrium statistical physics [94] to our nonequilibrium setting, evaluating the pressure difference

$$\hat{\sigma} = \frac{1}{2}\int dz\, \left[p_z(z) - \frac{1}{2}\left(p_x(z) + p_y(z)\right)\right], \tag{4.1}$$

In our simulation setup there are two interfaces that contribute equally (see also Fig. 4.3 below) to the integral, and thus a factor $1/2$ is included in Eq. (4.1). Some remarks are in order: The definition of a spatially resolved pressure tensor requires care, as discussed in detail in Ref. [202]. A crucial requirement is that the pressure $p_z(z)$ normal to the interface is constant as a function of z; this we have checked to be fulfilled in our calculations [203]. Equation (4.1) also assumes the integrand to vanish in the bulk regions. This is no

longer the case for a non-Newtonian fluid under shear, where shear-dependent normal-pressure differences arise. We will discuss this in more detail below. The use of Eq. (4.1) outside equilibrium is not *a priori* justified.

We thus also determine the surface tension via the width of the density profile Δ [204–206]:

$$\Delta^2 = \Delta_0^2 + \frac{k_B T}{2\pi \cdot \hat{\sigma}} \cdot \ln(L/B_0)\,, \tag{4.2a}$$

where we fit the density profile according to

$$\rho(z) = \frac{\rho_l}{2} - \frac{\rho_l}{2} \cdot \tanh\left(\frac{2 \cdot (z - z_0)}{\Delta}\right)\,, \tag{4.2b}$$

with the bulk liquid density ρ_l, and z_0 a fit parameter for the position of the interface. In Eq. (4.2a), Δ_0 and B_0 are unknown prefactors determined from fits for two different L (small and wide system).

We checked that our results recover the surface-tension values for the one-component quiescent LJ-potential fluid reported in Ref. [207]. For reference, the bulk viscocity was determined using the standard Green-Kubo relation [208] in simulations of the bulk fluid, using a correlation time of up to $100\tau_0$.

We begin by summarizing the temperature dependence in the quiescent system. As the glass transition is approached, the viscosity of the bulk fluid strongly increases; for around two orders of magnitude in the interval $T = [0.5, 1]$ studied here (stars in Fig. 4.2). The data is in the regime of the Mode Coupling Theory (MCT): close to the cross-over temperature T_c of MCT, the viscosity shows power-law growth, $\eta \sim |T - T_c|^{-\gamma}$ from which deviations would set in at lower temperatures (a dashed line in Fig. 4.2 indicates the power law with $T_c = 0.4$ and $\gamma = 2.35$). In the same temperature interval, the surface tension (circles) increases by almost a factor of 4. An empirical relation that links the surface tension and the viscosity has been proposed [209, 210]: $\ln(\hat{\sigma}) = \ln(A) + B/\eta$ with fitting parameters A and B. We observe this to hold reasonably

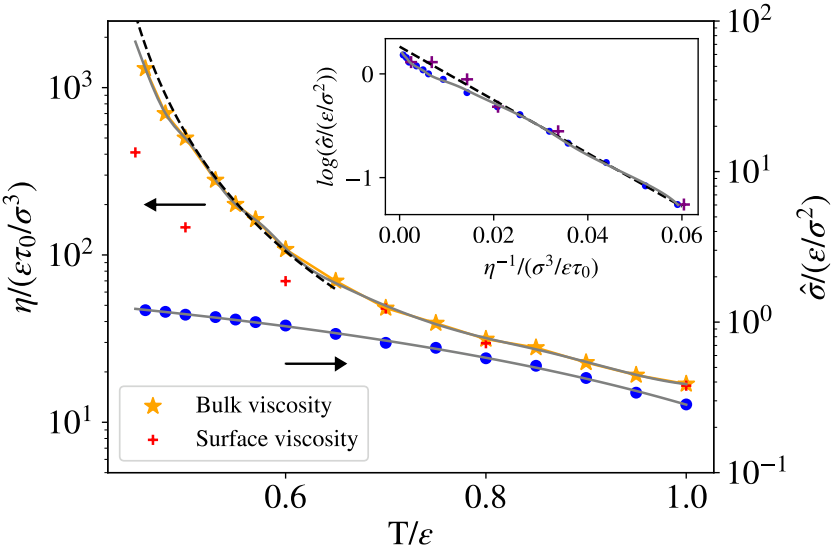

Figure 4.2: Bulk viscosity (star symbols) and surface tension (circles) of the quiescent system as function of inverse temperature. Solid lines are guides to the eye. A dashed line indicates the power-law predicted by mode-coupling theory, and crosses indicate the surface viscosity (see text). Inset: logarithm of the surface tension as a function of inverse viscosity (circles) and inverse surface viscosity (crosses).

well (only) in the no-too-viscous regime ($\eta \lesssim 50$; inset of Fig. 4.2). For lower temperatures, we see deviations that we attribute to the slow structural relaxation affecting the viscosity: while the viscosity strongly grows, the surface tension appears to saturate (or grow less strongly) as the MCT transition is approached.

Particles close to the surface of a glass-forming fluid retain higher mobility than in the bulk [186, 187, 211]. It hence suggests itself to define a "surface viscosity" that might bear a closer connection to the surface tension since it will grow less strongly than the bulk viscosity.

We have defined a surface viscosity by constraining the Green-Kubo integral to particles starting in z-layers close to the surface. The notion of "close" can be made precise by looking at the normal-stress differences, $\Delta p_{\alpha\beta} = p_\alpha - p_\beta$, where $\alpha, \beta \in \{x, y, z\}$. Recall that in the isotropic bulk, all $\Delta p_{\alpha\beta} = 0$. Close to the surface, the values for $\beta = z$, $\alpha \in \{x, y\}$, deviate from zero since the surface induces an anisotropy. This allows to clearly distinguish a surface layer (cf. Fig. 4.3a). Note that this surface layer is significantly wider than the width of the density profile (Fig. 4.3c and d). The surface-layer viscosity thus defined indeed follows the empirical relation to the surface tension more closely (crosses in Fig. 4.2), although approaching to T_c a decoupling still appears to occur. (note that the lowest-T data point in our simulation deviates). We leave this question for a future study.

Now we turn to surfaces with in-plane shear flow. Glass formers are non-Newtonian fluids, featuring non-vanishing normal-stress differences in the bulk.

In particular, the first normal stress difference in the bulk, in our setup is defined as $N_1 = \sigma_{yy} - \sigma_{xx} = \Delta p_{xy}$ [1] and is expected to be positive according to standard rheological models. This is observed in the center of the liquid slab (Fig. 4.3b, around $z = 0$) and confirmed by separate bulk simulations.

Crucially, the surface-near region remains different: here, pressure differences are related to the surface tension, and separate from the bulk. The changes in these regions will be related to a change in surface tension under shear. They become more pronounced at lower temperatures, as T_c is approached, while at higher temperatures the effect vanishes (lower panels of Fig. 4.3). As shown by the density profiles (gray lines in Fig. 4.3) we do not observe systematic density changes in the system, and thus the surface-tension and viscosity effects that we discuss here are not related to a change in density.

[1] We use the "tensile" convention common in rheology, noting that some authors use a "compressive" convention with the opposite sign, noting $\sigma_{\alpha\alpha} = -p_\alpha$.

However, the bulk values give non-trivial contributions to the surface-tension integral that are specific to non-Newtonian fluids, and need to be taken into account when determining the surface tension of the sheared fluid from Eq. (4.1). If not disentangled, an apparent surface tension is obtained that shows a pronounced system-size effect (Fig. 4.4, green symbols). Larger systems are more strongly influenced by the non-Newtonian bulk rheology, to the point that the apparent surface tension might even vanish at large shear rates. It should be noted that this is not a destabilization of the interface; it is rather a non-equilibrium signature of the driven system, similar to what has been observed in active fluids [212, 213].

It is thus crucial to separate the two regions in z – the surface layer identified by positive $\Delta p_{\alpha z}$, and the bulk liquid where these quantities have oppositve sign (blue and orange symbols in Fig. 4.4). Both depend quadratically on the shear rate, as is expected from the symmetry of the problem under reversal of the flow direction.

Intuitively, it is the pressure drop across the surface layer that relates to the surface properties. We confirm this by determining the surface tension from an analysis of the density profile, Eq. (4.2). Since this procedure determines $\hat{\sigma}$ only up to a prefactor, we have adjusted this to match the value obtained from Eq. (4.1) at zero shear rate. The results for the $\dot{\gamma}$-dependence then are in very good agreement with each other (dashed black line in Fig. 4.4).

These results show that there is a genuine shear-rate dependence of the surface tension in the non-Newtonian fluid that can be distinguished from the bulk rheology, but is still coupled to it. (In the Newtonian fluid represented by $T = 1$, we do not observe a significant shear-rate effect, as shown by Fig. 4.3c.) The change in surface tension is not just a consequence of a change in viscosity, as the empirical scaling relation discussed around Fig. 4.2 might have suggested. This is clearly seen by comparing the shear-rate dependences (Fig. 4.5). By symmetry, the shear-thinning viscosity should decrease as $1/|\dot{\gamma}|$ [43]; a somewhat weaker decay is observed in the

simulation, consistent with earlier results [214]. Also the surface-layer viscosity that we defined follows this trend (circle symbols in Fig. 4.5). The onset of shear thinning is at $\dot{\gamma}\tau_0 \ll 1$, indicating that it is the slow structural relaxation time ($\tau \gg \tau_0$) that sets the relevant time scale for shear thinning. The surface tension, properly disentangled from the bulk rheology, follows a $1/\dot{\gamma}^2$ "shear thinning" law, but importantly with an onset at much higher $\dot{\gamma}\tau_0$ (and thus higher than expected for the bulk normal-stress differences [215]).

In summary, we have shown that the surface tension of a typical glass-forming viscoelastic fluid shows a strong shear-rate dependence. In non-Newtonian fluids, normal-stress differences in the bulk and surface anisotropy of the stress tensor contribute to an effective surface tension that is measured using standard techniques that are based on the pressure drop across a liquid film and mix two different contributions. One contribution is a genuine surface contribution, and it comes from the pressure anisotropy in the layers near the surface. In the simulation they can be clearly identified through the different sign of $\Delta p_{\alpha z}$ with respect to the bulk. In addition, there is a non-trivial bulk contribution arising from non-vanishing normal-stress differences, a typical non-Newtonian fluid effect.

This might explain why the determination of surface tension values from pressure balances of bulk viscoelastic samples is difficult, as in experiments it will be difficult to disentangle the pure surface from a bulk contribution. Also, hysteresis effects as previously reported might be arising from a non-Newtonian bulk contribution: we have monitored the transient evolution of the pressure differences after switching on the shear flow, and found no sign of slow relaxation in the surface contribution. But the bulk quantities are known to exhibit patterns of slow relaxation. Also, a changing volume-to-surface ratio, as in techniques where a fluid droplet is expanded or compresses, might see effects from different mixing of surface and bulk contributions.

Our findings should be relevant to various techniques measuring interfacial rheological properties in films of complex fluids [216–218]

and even for the printability of bio-inks in surface-tension assisted 3d-printing techniques [219]. For example, biofilms are known to exhibit complex rheology, and characterization of their mechanical surface properties is an important aspect in their growth and removal [220, 221]. The complex interactions in such films can render the surface tension anisotropic [24], and our method of imposing in-plane shear flow in different directions might be a straight-forward way to interrogate the characteristics of the interface in such cases.

We expect our results to be generic and applicable to a wide range of non-Newtonian fluids, including *e.g.*, polymer melts. So far we are not aware of systematic studies, although in the rheology of foams a flow-rate dependent surface tension has been discussed [222, 223]. Also a recent study of soft silicone gels [224] found a change in surface tension as the material was deformed. Understanding the link of liquid-state surface tension and emergent elastic contributions across the glass transition will be a future field of study that also might help to understand the nature of kinetic arrest further.

On a more theoretical note, it has been shown that the surface of glass-forming fluids reveals non-monotonic changes in the dynamical correlation length governing glassy dynamics [102, 186]. A crucial point there was to distinguish a static length scale linked to the density profile, from a much larger dynamic one linked to the structural-relaxation dynamics. To explore the link between this dynamic length scale and the depth of the surface layers inferred from the pressure anisotropy remains an interesting open question, as it links inherent features of glassy dynamics to surface properties, and thus might provide further insight into theories of dynamical heterogeneities. Also, we leave for further discussion the fate of the surface tension in the deeply supercooled regime (below the MCT transition): eventually, the visco-elastic nature of the glass-forming fluid will be felt, and as one approaches the soft solid state, surface tension and surface energies need to be distinguished [225]. The study of the flow-rate dependence in the glassy regime can probe the different time scales involved in the transition.

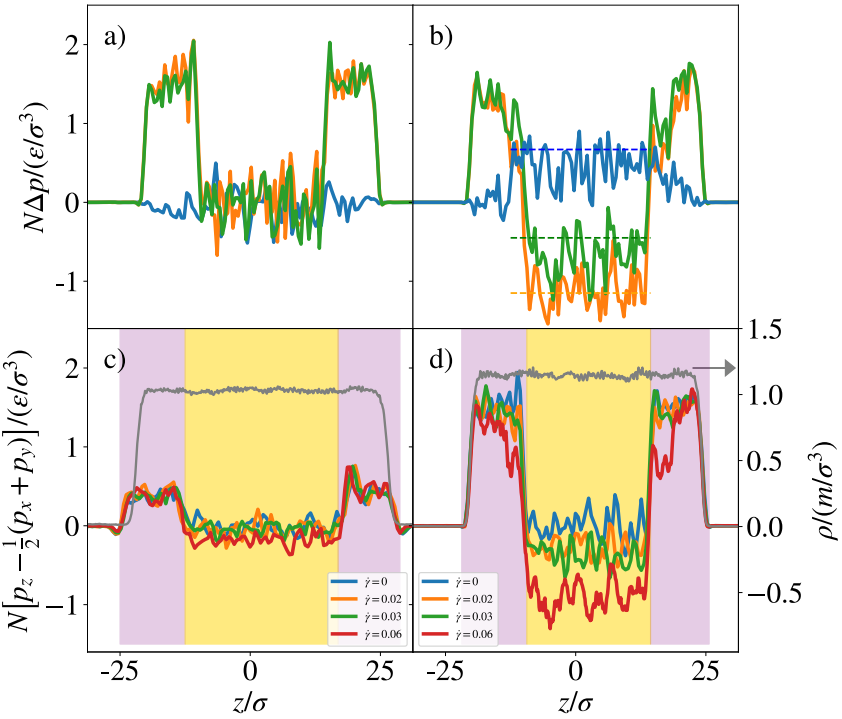

Figure 4.3: Pressure differences across the interface: Top panels show $\Delta p_{\alpha\beta} = p_\alpha - p_\beta$ (blue: Δp_{xy}; green: Δp_{xz}; orange: Δp_{yz}) for temperature $T = 0.6$ in (a) the quiescent system and (b) with shear rate $\dot{\gamma} = 0.06$. Dashed lines in (b) correspond to normal stresses obtained from separate simulations of a bulk system. Bottom panels show the relevant pressure difference for the surface tension, $-(\Delta p_{xz} + \Delta p_{yz})/2$, for (c) temperature $T = 1$, and (d) $T = 0.6$. Color shadings indicate the z-intervals identified as bulk and surface regions. All pressure values are multiplied by the number of particles in the respective z-bin to mitigate fluctuations from normalization. In the bottom panels, gray lines (corresponding to right y-axes) show the corresponding density profiles.

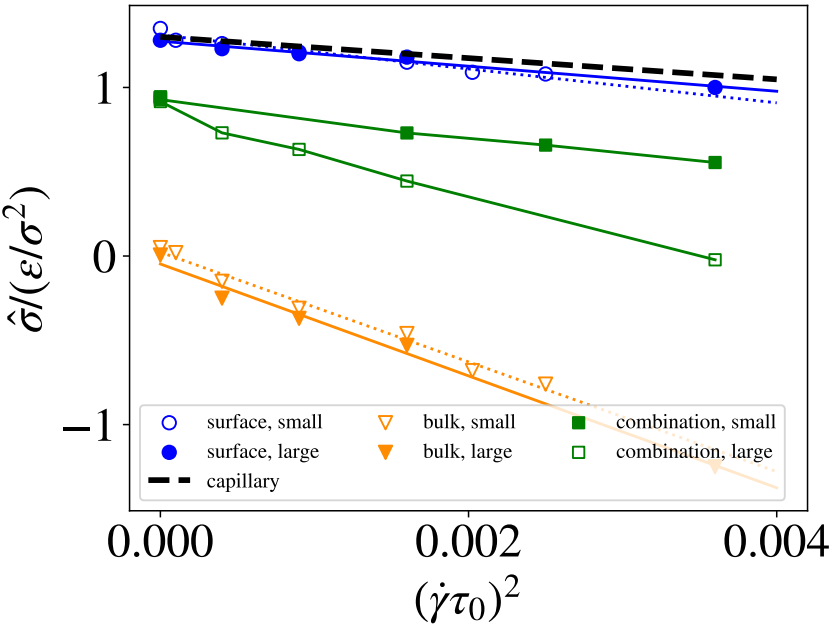

Figure 4.4: Shear-rate dependence of the surface tension, as a function of the square shear rate $\dot{\gamma}^2$, for the Kob-Andersen mixture at $T = 0.6$. Blue symbols show values extracted from the pressure difference, a dashed line the trend extracted from capillary wave analysis. The contribution from the bulk of the non-Newtonian fluid (orange) leads to a system-size dependent effective surface tension (green), if evaluated by the pressure difference.

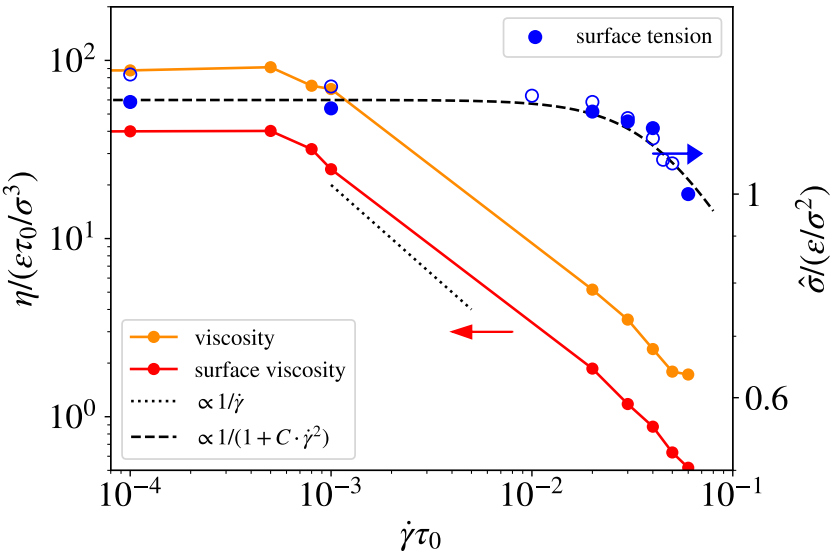

Figure 4.5: Viscosity, surface-layer viscosity, and surface tension as functions of shear rate for $T = 0.6$. A dotted line indicates $1/\dot{\gamma}$, the shear-thinning asymptote expected on dimensional grounds. The dashed line is a fit to the surface tension values that crosses over from a constant to a $1/\dot{\gamma}^2$ behavior.

Chapter 5

Spectral analysis of the velocity relaxation in nanoscale channels

This chapter has been published as Heitmeier, L., Voigtmann, Th., and Hansen, J.S. "Spectral analysis of the velocity relaxation in nanoscale channels.", Phys. Fluids 37, 122019 (2025)

We investigate the fluid velocity relaxation in a nanoscale channel using molecular dynamics simulations and hydrodynamic modeling. The relaxation dynamics is described in terms of the spatially resolved Fourier modes, and we establish from simulations that only modes with wave vector equal to or smaller than then external driving wave vector are excited. The relaxation features a predominantly viscous behavior for small wave vectors, and becomes more viscoelastic as the wave vector increases. From the Fourier mode analysis we can reconstruct the spatial averaged relaxation using particular modes and we conclude that two modes are governing the dynamics: The system's largest wavelength mode and the external driving mode. By comparing model output based on the Maxwell-Wiechert model and the modified Maxwell model to simulation data we see

that the later model performs best. Moreover, from this model we conclude that the system features a wave vector independent reduced viscous response and a wave vector dependent enhanced elastic response for the wavelengths studied here.

5.1 Introduction

Our fundamental understanding of the dynamical properties of fluid systems on the nanoscale is still far from complete. Direct comparison between atomistic simulations and the Navier-Stokes equation have shown that the standard hydrodynamic continuum theory is applicable on surprisingly small length scales, see e.g. Refs. [51, 226–228]. However, as the characteristic length scale decreases to a few nanometers the standard theory eventually breaks down depending on the specific system; for example, intrinsic non-local mechanical responses become important on the nanoscale [59, 229, 230], and coupling phenomena not relevant on macroscopic length scale can significantly affect the system flow properties on the nanoscale [231, 232]. This, of course, calls for new theoretical developments, and the hydrodynamic description has been extended and generalized to model the relevant mechanisms [233–236].

Fluids confined in nanoscale channels and tubes pose a particular challenge because of the static fluid density inhomogeneity that are present in the wall-fluid interfacial region [237, 238]. Depending on the actual definition and the system, this interfacial region can extend 2-3 molecular diameters into the channel, and the density can vary by a factor of around two. Recently Carlson and Netz [239] introduced position dependent wall-fluid friction and viscosity coefficients from a gradient expansion of the non-local kernels. It was shown that introduction of these two coefficients affect the boundary conditions and therefore the system flow properties in the wall-fluid region. One could expect that the entire flow profile is significantly affected by this, however, the inhomogeneity has been shown to have a small effect on the fluid flow for channel heights above 10 molecular diameters for a Lennard-Jones liquid undergoing Couette and Poiseuille flows, see for example Bitsanis et al. [240] and Travis et al. [229]. This is likely due to the non-local response, but other models have also been proposed like the local average density model [241]. Importantly, when modeling these confined systems one can assume homogeneity for channel heights above a certain threshold

and therefore also constant transport coefficients.

Recently, Knudsen et al. [242] investigated a fluid system applying a spatial sinusoidal varying shearing force. In the steady-state it was found that the velocity and shear pressure feature additional Fourier modes for sufficiently small wavelength for the force. This is in agreement with previous studies using synthetic non-equilibrium simulations [243, 244]. Knudsen et al. also investigated the spatially averaged relaxation dynamics at different zones in the channel after the field was switched off. It was shown that in the wall-fluid interface zone the relaxation is characterized by an enhanced elastic process, see also Ref. [245], whereas in the channel center zone the relaxation is mainly viscous (bulk-like) as expected. Interestingly, there is a zone between these two, which initially features a fast exponential relaxation, but transitions into a very slow decay with unknown functional form. It is not clear what underlying processes are behind the relaxation in this zone, but the authors concluded that the purely viscous Newtonian model and the viscoelastic Maxwell model cannot account for this relaxation.

We here extend the work by Knudsen et al. by performing a spectral analysis of the relaxation from a steady-state profile to the zero flow situation. The analysis is based on molecular dynamics simulations of the system and two models: (i) a two element Maxwell-Wiechert model and (ii) a single element modified Maxwell model. These two models are extensions to the classical Newtonian and Maxwell models by including (i) additional relaxation modes and (ii) length scale dependent corrections to the elastic and viscous processes, respectively. The models will give predictions for the relaxation in Fourier space (spectral relaxation), and these predictions are compared to the simulation data.

The spectral relaxation analysis serves two purposes, namely, to gain a deeper understanding of the multiscale viscoelastic relaxation in nanoscale confinement through comparison of model predictions to simulation data, and to test the two models. We choose to simulate a confined binary Lennard-Jones fluid, because the viscoelas-

tic properties can be probed more carefully compared to the single Lennard-Jones fluid used in Ref. [242]. Moreover, we focus on the relaxation dynamics from a single steady-state profile, where the wavelength is sufficiently large such that non-local transport phenomenon can be ignored, while the different relaxation zones are still resolved.

5.2 The models

We follow the system setup given in Knudsen et al. [242]. A fluid is confined between two parallel walls with normals in the z-direction, see Fig. 5.1. For time $t < 0$ an external sinusoidal driving force is applied to the fluid in the x-direction resulting in a local force density

$$F_{\text{ext}}(z) = \rho A \sin(d_3 z)\,, \tag{5.2.1}$$

where ρ is the mass density, A the acceleration amplitude, $d_3 = 3\pi/h$ the external force wave vector, and h the system half height such that $-h \leq z \leq h$. In the Appendix we list the symbols.

Due to density inhomogeneities in the wall-fluid interfacial zone, the steady-state velocity profile $u_0 = u_0(z)$ features other modes than that of the external force given by d_3 [242–244]. In general, we then write u_0 in terms of a sine Fourier series

$$u_0(z) = \sum_{m=1}^{\infty} u_m \sin(k_m z)\,, \tag{5.2.2}$$

where u_m is the velocity Fourier coefficient and $k_m = m\pi/h$. The Fourier transform of u_0 is given by the inner product over the interval $[-h; h]$; for k_m we have

$$\tilde{u}_0(k_m) = \int_{-h}^{h} u_m \sin(k_m z) e^{-ik_n z}\,\mathrm{d}z = -ihu_m\delta_{n,m} = -ihu_m\,, \tag{5.2.3}$$

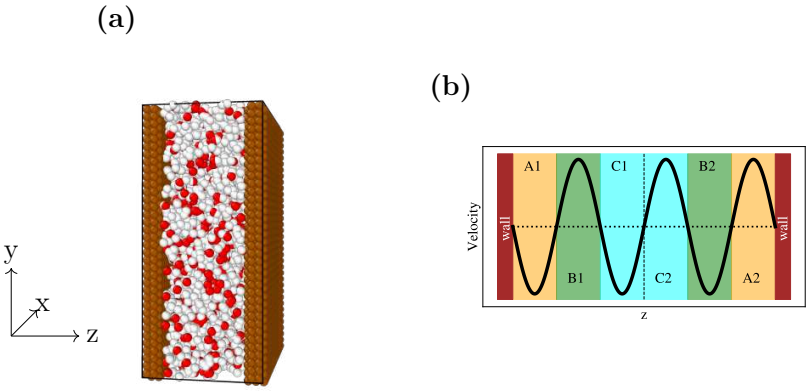

Figure 5.1: (a): Snapshot of the molecular dynamics simulation. White and red particles are A and B particles, respectively, and brown particles are wall particles. (b): Schematic illustration of the system steady-state velocity profile and spatial zones.

where $\delta_{n,m}$ is the Kronecker delta. In the steady-state we have a purely viscous response and the steady-state shear pressure, P_0, we model by Newton's law of viscosity $P_0 = -\eta_0 \partial_z u_0$, where η_0 is the zero frequency shear viscosity, i.e.,

$$P_0(z) = -\eta_0 \sum_{m=1}^{\infty} k_m u_m \cos(k_m z)\,. \tag{5.2.4}$$

The Fourier transform is

$$\tilde{P}_0(k_m) = -\eta_0 k_m h u_m. \tag{5.2.5}$$

Some time after the steady-state is reached the external force is removed (this defines $t = 0$) and we investigate the viscoelastic relaxation. To ease the reading we will from hereon write the wave vector k_m simply as k omitting the subscript m with a few exceptions.

The relaxation dynamics depends on the wave vector, or equivalently, the length scale we study. The spectral modeling we perform here is limited to length scales larger than the density variations in the wall-fluid zone, and we will therefore, as an approximation, assume that the density is constant and given by the bulk density, $\rho = \rho_0$. Moreover, at these length scales we ignore non-local transport phenomena. Thus, the method applied will not be applicable for (i) systems where the density variation extends far into the channel such that the different wave lengths cannot be studied using the constant density assumption, or (ii) where the characteristic length scale for the non-local transport properties become comparable with the wave length, e.g., in glassy systems [230].

5.2.1 Maxwell-Wiechert relaxation

As mentioned above, the single element Maxwell model does not capture correct dynamics for the relaxation [242]. Therefore, we first derive the relaxation dynamics using a two element Maxwell model (or an Maxwell-Wiechert element [246]). The model introduces two partial shear pressures P_1 and P_2, and associated relaxation times, τ_1 and τ_2, and viscosities, η_1 and η_2; these are also referred to as slow and fast coefficients [247]. The shear pressure is the sum of the partial shear pressures $P = P_1 + P_2$. For $\alpha = 1, 2$ we have the constitutive relation

$$\frac{\partial u}{\partial z} = -\frac{1}{\eta_\alpha}\left(1 + \tau_\alpha \frac{\partial}{\partial t}\right) P_\alpha \,, \tag{5.2.6}$$

which relates the partial shear pressures to the local strain rate. Notice that $u = u(z,t)$ is the spatio-temporal dependent velocity. In Fourier space it reads

$$ik\widetilde{u} = -\frac{1}{\eta_\alpha}\left(1 + \tau_\alpha \frac{\partial}{\partial t}\right) \widetilde{P}_\alpha \tag{5.2.7}$$

or by re-arranging

$$\tau_\alpha \frac{\partial \widetilde{P}_\alpha}{\partial t} = -ik\eta_\alpha \widetilde{u} - \widetilde{P}_\alpha \,. \tag{5.2.8}$$

For $t \geq 0$ the external force is zero and the momentum balance is simply $\rho_0 \partial_t u = -\partial_z P$ from the assumption of constant density. In Fourier space we have

$$\rho_0 \frac{\partial \widetilde{u}}{\partial t} = -ik(\widetilde{P}_1 + \widetilde{P}_2) \tag{5.2.9}$$

in terms of the partial shear pressures. Equation (5.2.8) with $\alpha = 1, 2$ and Eq. (5.2.9) form a closed linear problem $\dot{\tilde{\mathbf{x}}} = H\tilde{\mathbf{x}}$, where we have used the dot-notation for the time derivative, $\tilde{\mathbf{x}} = (\widetilde{u}, \widetilde{P}_1, \widetilde{P}_2)$, and H is the hydrodynamic coefficient matrix given by

$$H = -\begin{bmatrix} 0 & \frac{ik}{\rho_0} & \frac{ik}{\rho_0} \\ \frac{ik\eta_1}{\tau_1} & \frac{1}{\tau_1} & 0 \\ \frac{ik\eta_2}{\tau_2} & 0 & \frac{1}{\tau_2} \end{bmatrix}. \tag{5.2.10}$$

The general solution reads $\widetilde{\mathbf{x}} = \sum_{n=1}^{3} c_n \mathbf{v}_n e^{\omega_n t}$, where c_n are integration constants, $\mathbf{v}_n = (v_{n,1}, v_{n,2}, v_{n,3})$ the eigenvectors, and ω_n the eigenfrequencies of H. In particular, for the velocity relaxation we have

$$\tilde{u}(k,t) = \sum_{n=1}^{3} c_n v_{n,1} e^{\omega_n t}. \tag{5.2.11}$$

In our simulations we do not have values for $\tilde{P}_1(k,0)$ and $\tilde{P}_2(k,0)$ and we therefore let c_1 and c_2 be free fitting parameters and determine c_3 from the initial condition for the velocity $\sum_{n=1}^{3} c_n v_{n,1} = \widetilde{u}(k,0) = -ihu_m$. Hence, the model parameter set consists of the two relaxation times, τ_1 and τ_2, the two viscosities, η_1 and η_2, as well as c_1 and c_2. From the treatment here, we expect that the relaxation times and the viscosities are independent of the wave vector k, however, we will allow them to vary with respect to k in the fitting procedure explained below; this also follows Ref. [247].

5.2.2 Single-element modified Maxwell relaxation

We alternatively model the relaxation using a single-element modified Maxwell model [248]

$$-\eta_0 \int f(z-z') \frac{\partial u}{\partial z'} \, \mathrm{d}z' = P(z,t) + \tau_M \frac{\partial}{\partial t} \int g(z-z') P(z',t) \, \mathrm{d}z'. \tag{5.2.12}$$

Here τ_M is the Maxwell relaxation time defined by $\tau_M = \eta_0 / G_\infty$, G_∞ being the modulus of rigidity. The kernels f and g are length scale dependent corrections to the direct interpolation between the purely viscous and elastic behaviors; these corrections relax the attenuation-frequency locking phenomenon present in the original Maxwell model [248]. Notice, that the kernels phenomenologically measure the effect of the different microscopic processes for momentum diffusion (viscosity) and the elastic deformation, however, they do not reveal the underlying details of the molecular motions behind the effects. The original Maxwell model is re-captured in the limit where f and g are given by the Dirac delta. Importantly, f and g are in this treatment not standard transport kernels as used in Ref. [248] and for which the viscosity can be evaluated from independent simulations, e.g., by using the transverse current autocorrelation function. Here the kernels model the length scale dependent corrections to the direct interpolation. In Fourier space Eq. (5.2.12) is

$$-i\eta_0 k \, \tilde{f} \, \tilde{u} = \left(1 + \tau_M \tilde{g} \frac{\partial}{\partial t}\right) \tilde{P} \, . \tag{5.2.13}$$

Note that if $\tilde{f} = \tilde{g} = 1$ for a given wave vector k we obtain the original Maxwell model for this characteristic length scale. It is also clear from Eq. (5.2.13) that if $\tilde{f}$ or $\tilde{g}$ is less than unity the system features a reduced viscous or a reduced elastic response, respectively. Vice-versa, if $\tilde{f}$ or $\tilde{g}$ is greater than unity the system features an enhanced viscous or elastic response.

Now, Laplace transforming with respect to time gives

$$-i\eta_0 k\tilde{f}\,\hat{u} = \hat{P} + \tau_M\tilde{g}\,(s\,\hat{P} - \tilde{P}_0)\,, \tag{5.2.14}$$

where $\hat{u} = \hat{u}(k,s)$ is the Laplace transform

$$\hat{u}(k,s) = \int_0^\infty \tilde{u}(k,t)e^{-st}\,\mathrm{d}t\,, \tag{5.2.15}$$

and s is the Laplace coordinate. The Laplace transform for $\hat{P} = \hat{P}(k,s)$ follows the transform Eq. (5.2.15). Re-arranging Eq. (5.2.14) gives the equation for the shear pressure

$$\hat{P} = \frac{\tau_m\tilde{g}\tilde{P}_0 - i\eta_0 k\tilde{f}\hat{u}}{1+\tau_M\tilde{g}s}\,. \tag{5.2.16}$$

One can eliminate the shear pressure by application of the momentum balance equation as above. Recall, in real space and in absence of an external force we have $\rho_0\partial_t u = -\partial_z P$; in Fourier-Laplace space it becomes

$$\rho_0\,(s\hat{u} - \tilde{u}_0) = -ik\hat{P}\,. \tag{5.2.17}$$

Substitution of Eqs. (5.2.3), (5.2.5) and (5.2.17) into Eq. (5.2.16) we obtain after some re-arranging

$$\left(s + \frac{\eta_0 k^2\tilde{f}}{\rho_0(1+\tau_M\tilde{g}s)}\right)\hat{u} = ih\left(1 + \frac{\tau_M\eta_0 k^2\tilde{g}}{\rho_0(1+\tau_M\tilde{g}s)}\right)u_m\,. \tag{5.2.18}$$

It is instructive to highlight a special case before treating the general situation. In the purely viscous regime $\tau_M = 0$ and Eq. (5.2.18) reduces to

$$\left(s + \frac{\eta_0 k^2\tilde{f}}{\rho_0}\right)\hat{u} = ihu_m\,.$$

Introducing the kinematic viscosity $\nu_0 = \eta_0/\rho_0$ we get

$$\hat{u} = \frac{ihu_m}{s+\nu_0 k^2\tilde{f}} \tag{5.2.19}$$

or in the time domain

$$\tilde{u}(k,t) = ihu_m e^{-\nu_0 k^2 \tilde{f}(k)\, t}\,. \tag{5.2.20}$$

This gives the well-known exponential and purely k^2-dependent viscous relaxation. In this special case, we obtain the same functional form for the relaxation if the f-kernel is the viscosity transport kernel [51].

In the general case, $\tau_M \neq 0$, we get by re-arranging Eq. (5.2.18)

$$\hat{u} = ih\left(\frac{1+\nu_0 k^2 \tau_M \tilde{g} + \tau_M \tilde{g} s}{\nu_0 k^2 \tilde{f} + s + \tau_M \tilde{g} s^2}\right) u_m\,. \tag{5.2.21}$$

It is important to note that the second term in the nominator on the right-hand side depends on the viscosity, but not the f-kernel; this comes from the initial shear pressure $\tilde{P}_0 = \eta_0 kh$. On the other hand, τ_M and $\tilde{g}$ always appear as product, hence, we treat $\tau_M \tilde{g}$ as a single function. We identify two poles, s_1 and s_2, given by

$$s_{1,2}(k) = -\frac{1 \pm \sqrt{D}}{2\tau_M \tilde{g}}\,, \tag{5.2.22}$$

where $D = 1 - 4\nu_0 k^2 \tau_M \tilde{g} \tilde{f}$. The relaxation in time is then

$$\tilde{u}(k,t) = Pe^{s_1 t} + Qe^{s_2 t}\,, \tag{5.2.23}$$

where

$$Q = \frac{\mathcal{A} + \mathcal{B} s_2}{\tau_M \tilde{g}(s_2 - s_1)} \text{ and } P = \frac{\mathcal{B} s_1 - \mathcal{A}}{\tau_M \tilde{g}(s_2 - s_1)} \tag{5.2.24}$$

with the coefficients

$$\mathcal{A} = ih(1 + \nu_0 k^2 \tau_M \tilde{g}) u_m \text{ and } \mathcal{B} = ih\tau_M \tilde{g}\, u_m\,. \tag{5.2.25}$$

For complex poles, $s_{1,2} \in \mathbb{C}$, we have $1 < 4\nu_0 k^2 \tau_M \tilde{g} \tilde{f}$ corresponding to large values for η_0 and τ_M. In this case Q and P have the relations

that $\mathrm{Re}(Q) = -\mathrm{Re}(P)$ and $\mathrm{Im}(Q) = \mathrm{Im}(P)$. From Eq. (5.2.23) we then have

$$\tilde{u}(k,t) = i2be^{-\Gamma t}\cos(\omega_0 t)\,, \tag{5.2.26}$$

where $\Gamma = 1/(2\tau_M\tilde{g})$ is the attenuation coefficient and $\omega_0 = \frac{1}{2\tau_M\tilde{g}}\sqrt{4\nu_0 k^2\tau_M\tilde{g}\tilde{f} - 1}$ the characteristic frequency. Notice that in the limit of zero wave vector we have $1 > 4\nu_0 k^2\tau_M\tilde{g}\tilde{f}$ and $s_{1,2}$ are real.

As stated above, τ_M and $\tilde{g}$ appear as the product $\tau_M\tilde{g}$ and we treat this as a single wave vector dependent fitting parameter. ν_0 (or equivalently η_0) and $\tilde{f}$ are term-wise separated and we will use these two as separate fitting parameters; that is, this model has three free fitting parameters.

5.3 Molecular dynamics method

We perform the simulations with the GPU-accelerated software package gamdpy developed in-house [112]. The system is composed of $N = 5700$ fluid particles of type A and B confined between two planar body-centered-cubic (bcc) crystal walls. A few crystal defects are introduced in the wall in order to avoid fluid crystallization in the wall-fluid interface. All particles interact via the Kob-Andersen binary Lennard-Jones potential [100]

$$U(r_{ij}) = 4\epsilon_{\alpha\beta}\left((\sigma_{\alpha\beta}/r_{ij})^{12} - (\sigma_{\alpha\beta}/r_{ij})^{6}\right)\,, \tag{5.3.1}$$

where r_{ij} is the distance between particle i and j, and $\epsilon_{\alpha\beta}$ and $\sigma_{\alpha\beta}$ depend on the particle types and define the energy and length scales, respectively. Any mechanical property can be expressed in units of σ, ϵ, and mass m; as it is common practice we omit writing these units. We use the standard Kob-Andersen values with the A particles as reference, that is, $\sigma_{AA} = 1.0, \sigma_{BB} = 0.88, \sigma_{AB} = 0.8, \epsilon_{AA} = 1, \epsilon_{BB} = 0.5$, and $\epsilon_{AB} = 1.5$. The fluid mixture is the standard $N_A : N_B = 4 : 1$. The wall particles are A particles, and

they are tethered to the bcc lattice site with a restoring Hookean spring force with spring constant $k = 300$. The wall density is set to $\rho = 1$ and the temperature is controlled by thermostating the walls with a simple relaxation-type thermostat [249]; we have here simulated temperatures $T = 0.9$ and 2.0. In all simulations the equations of motion are integrated forward in time using the standard leap-frog algorithm with time step of 0.005 [250].

In accordance with the theory, each simulation consists of two phases. In the first phase we apply a force in the x-direction to each fluid particle with sinusoidal variation along z, $F = A\sin(d_3 z)$ with $A = 0.056$. This force amplitude is sufficiently low to ensure linearity and neglectable viscous heating effect such that the temperature is constant in the channel and given by the wall temperature [251]. The choice of maximum amplitude A is based on previous work by Knudsen et al. in a very similar simulation setup [242].

After reaching the steady state, the force is removed and the system relaxes to the zero flow situation. The velocity profile is calculated using a bin method for the particle momenta

$$u(z,t) = \frac{\sum_i m_i v_{x,i}(t) 1_Z(z_i)}{\sum_i m_i 1_Z(z_i)}\,, \tag{5.3.2}$$

where m_i is the mass of particle i, $v_{x,i}$ the x-component of the particle velocity, and 1_Z is the indicator function, $Z = [z - \Delta z/2; z + \Delta z/2[$ such that $1_Z(z_i) = 1$ if $z_i \in Z$ and $\Delta z = 0.13$ is the bin width; if $z_i \notin Z$ we have $1_Z(z_i) = 0$. The relaxation dynamics is characterized by a very large noise-to-signal ratio and we therefore average the profiles over 15000 runs. For the steady-state an additional time average is performed.
The code was tested by using a Lennard-Jones fluid and comparing with Ref. [242].

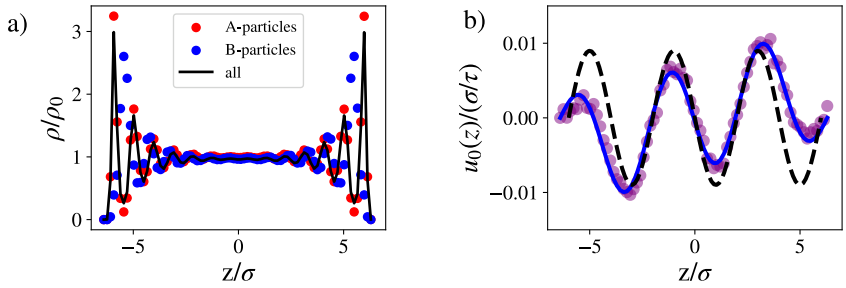

Figure 5.2: (a) Density profiles for particles A and B (circles), and the total density profile (full line). Profiles are normalized with their bulk values ρ_0. (b) The steady-state velocity profile. Circles represents simulations data, dashed line is the single sine velocity profile, Eq. (5.4.1), and full line the sine Fourier series, Eq. (5.2.2), using three terms. In both figures $T = 0.9$.

5.4 Results and Discussion

Figure 5.2 (a) shows the density profiles for A and B particles as well as the total density. We note that the density distribution of A and B particles are different, which is expected since the different Lennard-Jones parameters effect the particle packing both in the bulk fluid and in the wall-fluid zone. The total density, which is the relevant density here, is also shown and features the well-known layering phenomenon in the wall-fluid zone. Importantly, the system does not crystallize and a bulk fluid zone is present, hence, it is relevant to describe the system through hydrodynamics. The density profile is a very good approximation independent of the operating conditions used here.

In Fig. 5.2 (b) we plot the steady-state velocity profile $u(z, 0) = u_0(z)$; it is clearly seen that the profile exhibits additional Fourier modes than the excited d_3 mode. The prediction using the classical

Navier-Stokes equation reads [242]

$$u_0(z) = \frac{A}{\nu_0 d_3^2} \sin(d_3 z)\,, \tag{5.4.1}$$

and this fails to capture the different modes; Eq. (5.4.1) is shown as dashed line. The Fourier coefficients can be extracted from data using a straightforward Fourier sine integral

$$u_m = \frac{1}{2h} \int_{-h}^{h} u_0(z) \sin(k_m z)\, \mathrm{d}z\,, \tag{5.4.2}$$

where we highlight the wave number dependency of the wave vector $k = k_m = m\pi/h$. From Fig. 5.3 we observe that the magnitude of u_m rapidly decays for wave vectors larger than d_3. The long wavelength modes $m = 1$ and $m = 2$ contribute significantly to the overall signal. This is not observed for homogeneous flows [243] and must therefore be to the confinement. Since the characteristic wavelength for the density variations in the wall-fluid zone is smaller than the wavelengths probed here, we conjecture that this system size wavelength excitation is due to the additional shear force exerted by the walls as a result of the non-zero fluid velocity gradient present in the wall-fluid boundary region. A truncated sine Fourier series using three terms with $m = 1, 2, 3$ is plotted Fig. 5.2 (b) capturing the steady-state flow profile very well and we will only consider the long wavelengths (small wave vector) modes where $k_m \leq d_3$. Note that the excitation of modes of longer wavelength than the excited one is more pronounced for the lower temperature $T = 0.9$. This demonstrates that for lower temperature, the fluid's response becomes more non-local in space.

For the relaxation dynamics, the Fourier transformed velocity profile $\tilde{u}(k, t)$ is calculated from the velocity profile data by

$$\tilde{u}_{\mathrm{MD}}(k, t) = -i \int_{-h}^{h} u(z, t) \sin(kz)\, \mathrm{d}z. \tag{5.4.3}$$

The normalized imaginary part of the Fourier transforms are plotted in Fig. 5.4 for $m = 1, 2, 3$, and for $T = 0.9$ and 2.0. First, we observe the expected behavior, namely, that for small wave vectors the

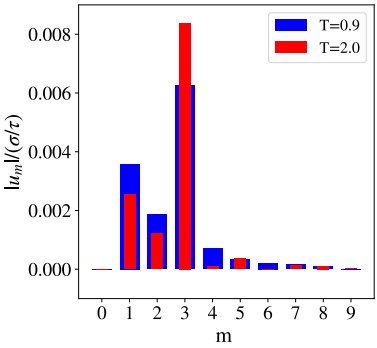

Figure 5.3: The spectrum for the steady-state velocity profile for temperature $T = 2.0$ and $T = 0.9$.

relaxation quickly enters a monotonous decay after approximately $t > 1.0$ consistent with a viscous response. As the wave vector increases, i.e., the characteristic wavelength decreases, the elastic process becomes more pronounced depending on the temperature. This is consistent with the homogeneous case, where the elasticity is observed as anti-correlations (or negative correlations) in the transverse current correlation function on small length scales. Moreover, it is in agreement with the behavior of the Hermite expansion for the moments of the particle distribution function, see Refs [252, 253]. For $T = 2.0$ and $m = 1, 2$ there is an initial increased response as the external force is removed. Note however that Fig. 5.4 shows the amplitudes of the Fourier modes normalized to their steady-state value at each m; the total velocity decreases. The reason for this initial response may be due to non-hydrodynamic coupling between modes and thus redistribution the shorter-wavelength contributions into longer-wavelength ones or the presence of generalized collective modes on these length scales [254].

We also plot the fits to the Maxwell-Wiechert model, Eq. (5.2.11), and the modified Maxwell model, Eq.(5.2.26). The fitting algorithm used is the Levenberg–Marquardt algorithm [255], where the initial parameters were all unity; other initial parameter sets were tested

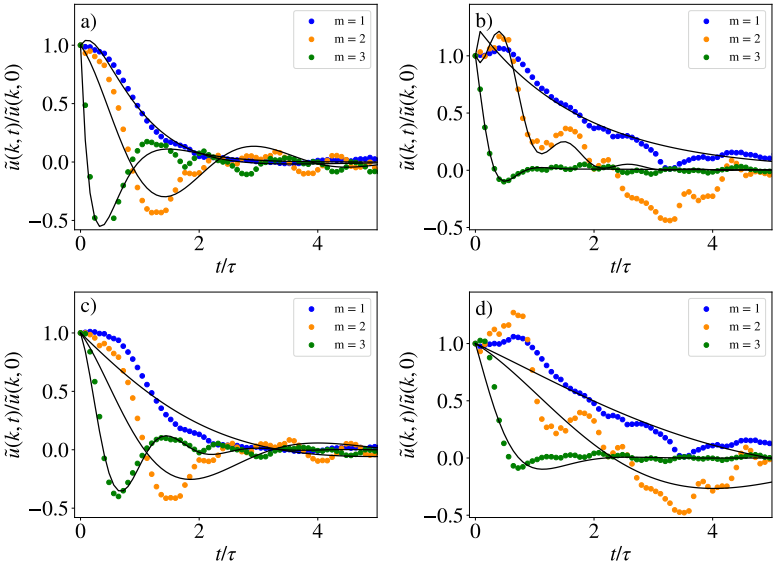

Figure 5.4: Relaxation of the Fourier modes $m = 1, 2, 3$ and fits to data using the Maxwell-Wiechert model (top row) and the modified single-element Maxwell model (bottom row). The first column corresponds to $T = 0.9$, the second column $T = 2.0$.

T	m	η_1	η_2	τ_1	τ_2	c_1	c_2	χ^2	η_0	τ_M
	1	4.7	0.4	0.3	0.6	-2.2	1.7	1.0		
0.9	2	2.2	2009	0.5	860	26.9	-26.0	0.8	22.4	1.6
	3	1.3	994	0.1	591	5.9	-5.8	0.4		
	1	18.8	32.8	0.2	4.4	-0.5	0.1	0.4		
2.0	2	16.5	1.3	0.4	0.7	-5.3	4.6	2.6	6.6	0.30
	3	2.8	1476	0.1	1744	324	-323	0.02		

Table 5.1: Fitting parameters for the Maxwell-Wiechert model. For reference the shear viscosity, $\eta_0(m=0)$, and Maxwell relaxation time, $\tau_M(m=0)$, are also listed in the two last columns; taken from Ref. [248].

giving the same resulting parameter values. The cost function is the standard χ^2-function

$$\chi^2(\boldsymbol{\theta}) = \sum_i \frac{[\tilde{u}_{\mathrm{MD}}(k,t_i) - \tilde{u}(k,t_i;\boldsymbol{\theta})]^2}{\tilde{u}_{\mathrm{MD}}(k,t_i)}, \tag{5.4.4}$$

where $\tilde{u}_{\mathrm{MD}}$ is given in Eq. (5.4.3), $\tilde{u}(k,t_i;\boldsymbol{\theta})$ is the predicted (model) value for the parameter set $\boldsymbol{\theta}$, and i is the sample index. The resulting fitting parameters can be seen in Tables 5.1 and 5.2. For reference we have included the shear viscosity and the Maxwell relaxation time taken from Ref. [248], which are evaluated from the stress-stress autocorrelation function.

Recall, the Maxwell-Wiechert model is fitted with six fitting parameters. We here also allow these to be wave vector dependent, otherwise the agreement will be very poor. From the fitted parameter values, we clearly see that the large parameter space results in a sloppy model [256] due to the over-parameterization, and the parameter values become nonphysical. One way to decrease the parameter space, would be to model the initial values for the two stresses, however, we will not pursue this further here.

The modified Maxwell model has only three free fitting parameters and it is evident that the model is less sloppy compared to the

Maxwell-Wiechert model. Also, we note that the fitted value for η_0 is close to the value found from independent simulations, in particular for $T = 0.9$, which gives confidence in our fitting procedure. For $T = 0.9$ the model, very accurately, captures the relaxation for the mode $m = 3$ which is the external mode, whereas the model predictions for $m = 1$ and $m = 2$ are less satisfactory.

T	m	η_0	$\tau_k\tilde{g}$	$\tilde{f}$	χ^2	η_0 $(m=0)$	τ_M $(m=0)$
	1	22.8	2.5	0.075	0.012		
0.9	2	24.3	1.8	0.072	0.022	22.4	1.6
	3	24.6	0.9	0.092	0.003		
	1	7.0	4.1	0.095	0.014		
2.0	2	8.6	3.8	0.085	0.049	6.6	0.30
	3	9.6	0.7	0.082	0.005		

Table 5.2: Fitting parameters for the modified Maxwell model. For reference the shear viscosity, η_0, and Maxwell relaxation time, τ_M, are also listed in the two last columns; taken from Ref. [248].

It is relevant to investigate the parameter correlations for the modified Maxwell model and to this end we perform a Metropolis Monte-Carlo analysis [257]. Let $\boldsymbol{\theta}_n = (\eta_0, \tau_M\tilde{g}, \tilde{f})$ for some parameter values and $\delta\boldsymbol{\theta}$ be a uniformly distributed increment with zero mean. We then define the Monte-Carlo move by $\boldsymbol{\theta}_{n+1} = \boldsymbol{\theta}_n + \delta\boldsymbol{\theta}$. If $\chi^2(\boldsymbol{\theta}_{n+1}) < \chi^2(\boldsymbol{\theta}_n)$ the new parameter set is always accepted, otherwise if $\chi^2(\boldsymbol{\theta}_{n+1}) \geq \chi^2(\boldsymbol{\theta}_n)$ the new parameter set is accepted only if $R < \exp\left(\chi^2(\boldsymbol{\theta}_{n+1})/\chi^2(\boldsymbol{\theta}_n) - 1\right)$, where R is a random number picked from a uniform distribution between 0 and 1. If the move is accepted the new parameter set is incremented, and in this way we perform a random walk in the parameter space. The initial parameter set is chosen from the best fit found above, and the increment magnitude is such that around half the moves are accepted giving 10^4 sets. From this we can form the covariance matrix and calculate the Pearson correlation coefficient, P. Table 5.3 shows the

correlation coefficients, and except for $P_{\eta_0,\tilde{f}}$ we observe small parameter correlations. This, in turn, indicates a model with identifiable

T	m	$P_{\eta_0,\tau_M\tilde{g}}$	$P_{\eta_0,\tilde{f}}$	$P_{\tau_M\tilde{g},\tilde{f}}$
	1	0.67	0.85	0.75
0.9	2	0.08	0.54	0.18
	3	-0.02	0.28	0.17
	1	0.23	0.32	0.20
2.0	2	0.14	0.41	0.12
	3	0.32	0.49	0.37

Table 5.3: Pearson correlation coefficients for the modified Maxwell model parameters.

parameters and also justifies the separate corrections term for the elastic and viscous element in the modified Maxwell model.

From the values of $\tilde{f}$ we can now conclude that the viscous response is significantly reduced for the wave vectors studied here when compared to the predictions from the standard Maxwell model. From Table 5.2 we have $\eta_0\tilde{f} \approx 1.6$ for $T = 0.9$ and $\eta_0\tilde{f} \approx 0.5$ for $T = 2.0$. Thus, while the response is reduced it is independent of the three wave vectors and the viscous response is the same. In contrast to this, the elastic response is enhanced since $\tau_M\tilde{g} > \tau_M$ except for $m = 3$ and $T = 0.9$. Moreover, the elastic correction changes with wave vector. Importantly, the elastic corrections are also observed for homogeneous systems [248], hence, while we must expect that the large density in the wall-fluid zone will affect the corrections quantitatively, the corrections are not only a result of the density inhomogeneity.

Having the Fourier transform $\tilde{u}(k,t)$ we can reconstruct the velocity profile by using the inverse transformation of Eq. (5.4.2) and from this evaluate the average velocity relaxation in each zone by $\langle u(t)\rangle_{\text{zone}} = \frac{1}{\Delta z}\int_{\text{zone}} u(z,t)\,\mathrm{d}z$, where Δz is the width of the zone; see the zone indices in Fig. 5.1. Due to symmetry, we can average over zones A_1 and A_2, B_1 and B_2, and C_1 and C_2; the average

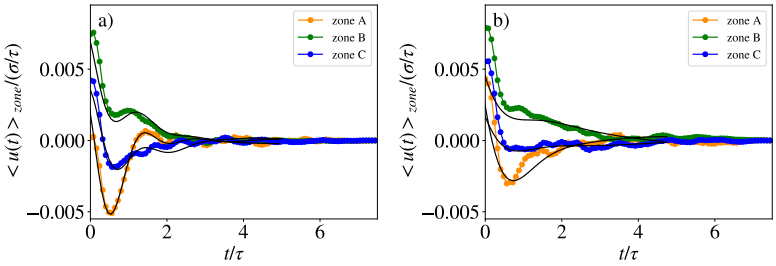

Figure 5.5: Velocity relaxation in the different zones of the channel. Colors are the simulation data, the black lines correspond to the reconstructed velocity relaxations using the three lowest Fourier modes. The images on the left-hand side correspond to $T = 0.9$, the images on the right-hand side correspond to $T = 2.0$.

zones we denote A, B and C. For $T = 0.9$ the averaged relaxation dynamics is captured very well, see Fig. 5.5, in particular the modified Maxwell model predicts the spatial non-monotonicity which the standard Maxwell model cannot. For $T = 2.0$ the agreement is not as good which is to be expected from the spectral fits, however, we still capture the non-homogeneous behavior.

In Fig. 5.6 the relaxation dynamics for $T = 0.9$ is reconstructed by inclusion of different modes. From (a) and (b) one clearly observes that the modes $m = 2$ and $m = 3$ fail to capture the short time dynamics, in particular, the local maximum around $t = 1$ in zone B is absent. In Fig. 5.4 (c) modes $m = 1$ and $m = 3$ are included and the different features are captured quite well, hence, we conclude that the non-monotonic behavior is due to the system longest wavelength response.

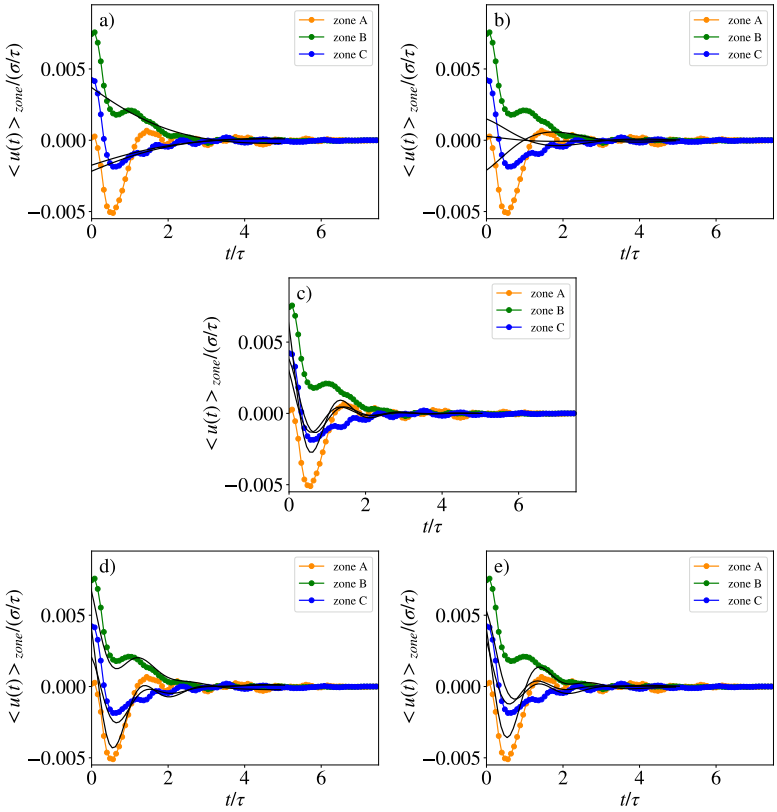

Figure 5.6: Velocity relaxation dynamics in the different zones for $T = 0.9$. Symbols connected with lines are simulation data and lines are predictions from the modified Maxwell model using the modes (a) $m = 1$, (b) $m = 2$, (c) $m = 3$, (d) $m = 1$ and $m = 3$, (e) $m = 2$ and $m = 3$.

5.5 Conclusion

In this paper we performed a spectral analysis of the relaxation dynamics of a visco-elastic fluid in a nano-scale channel. This was done by molecular dynamics simulations of a system relaxing from a sinusoidal velocity profile with characteristic wave vector d_3 to the zero flow state. The simulation results were compared with two different models, namely, the two element Maxwell-Wiechert model and a modified Maxwell model introducing separate spatial non-locality for the viscous and the elastic response.

The initial steady-state profile features excited long wavelength modes, i.e. for wave vectors $k_m \leq d_3$, and non-excited modes when $k_m > d_3$. This is in agreement with the findings in Ref. [242]. We conjecture that the long wavelength modes are due to shear force modes exerted by the walls in the flow situation. To elucidate this further, different surface morphologies should be tested, as was recently done in a related context [109].

For the relaxation of the Fourier modes the modified Maxwell model fits data better than the Maxwell-Wiechert model. Moreover, the Maxwell-Wiechert model has a large parameter space since we did not have information about the partial shear pressures, and this leads to a sloppy model. We therefore focused on the modified Maxwell model. For this model, it is found that both the viscous and elastic elements should be corrected and that these corrections are length scale dependent for the elasticity. Specifically, we observe a reduced viscous response, but an increased elastic response for the length scales studied here.

It is clear from the spectral analysis that two modes govern the averaged relaxation dynamics: One is the external mode, given by d_3, and the other is the mode given by the system's longest wavelength with wave vector $k_1 = \pi/h$.

In general, we find that the modified Maxwell model performs better for $T = 0.9$ than $T = 2.0$, that is, in the more viscoelastic state. Recall that Maxwell-type models are usually designed to describe

viscoelastic relaxation, rather than kinetic short-time contributions that become more prominent at higher temperatures. This could be a physical mechanism why we observe better performance of the modified Maxwell model for $T = 0.9$. For $T = 2.0$, the spectral relaxation predictions are not accurate and the model fails to capture the local maximum at $t = 2$ and $m = 2$. However, this maximum has an insignificant effect on the averaged relaxation curves. The maximum is featured in the Maxwell-Wiechert model, which is not surprising considering the large parameter space, and the physical interpretation of the maximum is still unknown.

The two hydrodynamic models applied here were both based on the fundamental assumptions of constant density and local mechanical responses, and were not able to capture all the dynamical features in the relaxation process, in particular, for $T = 2.0$ the agreement is poor. To improve the modeling one should therefore relax the assumptions, or alternatively, use different underlying descriptions like the generalized collective mode formalism, see Refs. [254] and [258]. Moreover, the hydrodynamic treatment entails a decoupling of modes; to investigate the validity of this assumption in detail one could approach the problem using mode coupling theory [259].

Chapter 6

Summary and Outlook

In the scope of this thesis, we investigated viscoelastic fluids both from a macroscopic and a microscopic perspective. In the first project, we studied the spreading process of droplets in microgravity. There, experimental results, which were obtained in microgravity, were complemented with Volume-of-Fluid simulations, and a strong agreement between these data was found. Both experimental and simulation results were compared to well established scaling laws, which predict how the height and the radius depend on the plasto-capillary number [47]. Surprisingly, our results show a much better agreement with the scaling laws in the case of ground experiments than in the case of microgravity. Since the main difference between the two cases lies in the extent to which surface tension influences the system, we propose that the surface tension of viscoelastic fluids exhibits a behavior that remains poorly understood. This is also supported by measurements of the surface tension of viscoelastic fluids, which show that the value obtained is not constant but shows pronounced hysteresis effects [29, 30].

Motivated by this deviation, the surface tension of viscoelastic fluids was investigated from a microscopic perspective, using molecular-dynamics simulations. There, we found a pronounced shear-rate

dependence of the surface tension, which can be split into two contributions: One contribution stems from the bulk of the fluid, and can be related to the theory of normal stresses in fluids, whereas another contribution originates from the surface region itself. In both regions, one can observe a quadratic dependence on the shear-rate, but in the case of the surface, this dependence is much weaker. With this result, our microscopic results are also highly relevant for experiments: From an experimental point of view, this would mean that the value of the measured surface tension depends on the amount of material which is used. This at least should be taken into account when experiments are conducted.

In the last chapter, we investigated the effect of relevant length scales in viscoelastic fluids. It is known that a fluid which is confined on the nanoscale cannot be fully described by constitutive laws which are established for macroscale descriptions. For example, the viscosity on these lengthscales is not seen as a constant anymore, but as a spatially dependent variable. Also, we identify that due to non-local effects in fluids, we get a pronounced mode dependence in the fluid, which is not seen either on the macroscale. In this last project, we investigated the properties of viscoelastic fluids on the nanoscale in more detail and by analyzing how different modes of the fluid are relaxing, we related this to the Maxwell model.

Each of the projects presented in this thesis opens up new and interesting research questions. Starting with the spreading process of viscoelastic droplets in chapter 3, one particularly intriguing aspect that was not investigated within the scope of this thesis concerns the internal stresses. During the VIPDROP campaign, in addition to shadowgraphy experiments presented here, particle-image velocimetry (PIV) and stress-optical measurements were also conducted [161]. In principle, these data allow for the extraction of both the temporal and spatial evolution of velocities and stresses inside the droplets. Such information could also be obtained from the numerical simulations that we already conducted for the study

in chapter 3. A combined experimental and computational study of this kind would not only provide deeper insights into the physical mechanisms governing droplet dynamics, but also improve our understanding of droplet stability under various gravitational conditions.

For this study, it is essential to further improve the analysis of stress-birefringent images. The main challenge lies in reconstructing the stress field, which is a three-dimensional tensor field, from its two-dimensional projections. While the reconstruction of scalar fields from projections is a well-established mathematical problem with applications also in medicine, only a few studies have addressed the corresponding problem for tensor fields [260–263].

Another promising direction for future research concerns the experimental setup itself. At present, the focus lies on the investigation of single droplets. However, for industrial applications such as 3D printing, it would be of great interest to study the coalescence of multiple droplets, as this process is much more relevant to practical applications.
Another possible experimental setup would be the that of an oscillating bubble. Possible research directions in this field would be to first derive a Rayleigh-Plesset-like equation for the bubble radius, using a similar constitutive law as in chapter 3. As bubble oscillations strongly depend on the surface tension [264, 265], from such a setup and a proper comparison to experiments, one could gain many insights regarding the surface tension of viscoelastic fluids.

Also, chapter 4 opens up several new research directions. A first question concerns the range of validity of the observed shear-rate dependence of the surface tension. It would be interesting to perform similar simulations for more realistic materials instead of the model system used in this work. In this context, one should also emphasize potential applications to active materials. A central question would be whether a comparable shear-dependent behavior of the surface tension can be observed in active systems and how the density profile of active particles look like. *I.e.* it would be of high

interest to find a relation between the properties of active particles and their behavior near the surface. (When do they behave like a surfactant? Is the surface still flat?) A possible application of this could be an investigation on how droplets are spreading, if their material includes active material. Such a project would also have many applications in medicine, where fluids, which contain bacteria, are used [266, 267].

Furthermore, the definition of surface tension in non-equilibrium systems remains an open problem. Although various definitions of surface tension exist, it is still unclear which of them remain valid under non-equilibrium conditions. This question becomes particularly relevant for active systems, which are by definition out of equilibrium, and where even negative values of the surface tension were reported [101, 268–271].

In chapter 4, we identified a distinct interfacial region that we referred to as the "surface region". Future work should include a detailed investigation of its temperature dependence. The physical motivation stems from glassy systems, where it has been observed that near surfaces, characteristic length scales increase with temperature [102].

Another promising direction would be to relate our findings to the Mode-Coupling Theory of the glass transition (MCT). In MCT, it has been shown that the normal stresses exhibit a $\dot{\gamma}^2$-dependence [272, 273]. Developing an analogous theoretical framework for the surface tension could provide further insight into the mechanisms behind this shear-rate dependence.

Finally, these effects should be explored experimentally. While progress has been made in this direction [274, 275], a precise determination of the surface tension under shear conditions is still lacking.

Finally, chapter 5 also leaves room for several open research questions. As in the previous chapter, the present investigation was limited to a model fluid. For practical applications, it would be

highly interesting to perform simulations with more realistic fluids, such as water or alkanes. Additionally, in this project, we observed that, under steady-state conditions, a variety of different modes were excited. The underlying physical mechanisms responsible for this behavior, however, remain to be clarified.
Moreover, in the interpretation of the data, a Gaussian shape was assumed for the kernel of the viscosity. This choice is a simplification and may not fully capture the true behavior of the system. A promising direction for future work would therefore be to investigate the actual form of the kernel and assess its impact on the observed dynamics.

References

[1] L. Heitmeier, O. D'Angelo, M. Jalaal, T. Voigtmann, *Journal of Rheology* **2026**, *70*, 631–643.

[2] L. Heitmeier, T. Voigtmann, *Physical Review Letters* **2026**, *136*, 068203.

[3] L. Heitmeier, T. Voigtmann, J. S. Hansen, *Physics of Fluids* **2025**, *37*, 122019.

[4] M. Jalaal, B. Stoeber, N. J. Balmforth, *Journal of Fluid Mechanics* **2021**, *914*, A21.

[5] D. Bonn, M. M. Denn, L. Berthier, T. Divoux, S. Manneville, *Reviews of Modern Physics* **2017**, *89*, 035005.

[6] M. Kröger, J. Vermant, The structure and rheology of complex fluids, Sciendo, **2000**.

[7] P. Coussot, *Soft Matter* **2007**, *3*, 528–540.

[8] R. L. Truby, J. A. Lewis, *Nature* **2016**, *540*, 371–378.

[9] J. A. Lewis, *Advanced Functional Materials* **2006**, *16*, 2193–2204.

[10] A. M'barki, L. Bocquet, A. Stevenson, *Scientific Reports* **2017**, *7*, 6017.

[11] M. Dey, I. T. Ozbolat, *Scientific reports* **2020**, *10*, 14023.

[12] P. S. Gungor-Ozkerim, I. Inci, Y. S. Zhang, A. Khademhosseini, M. R. Dokmeci, *Biomaterials science* **2018**, *6*, 915–946.

[13] Y.-J. Seol, H.-W. Kang, S. J. Lee, A. Atala, J. J. Yoo, *European Journal of Cardio-Thoracic Surgery* **2014**, *46*, 342–348.

[14] D. Milián, D. C. Roux, F. Caton, N. El Kissi, *Rheologica Acta* **2022**, *61*, 401–413.

[15] Q. Zhong, C. R. Daubert, Food rheology, Elsevier, **2013**, pp. 403–426.

[16] J. Ahmed, S. Basu, Advances in food rheology and its applications, Woodhead Publishing, **2016**.

[17] P. Fischer, E. J. Windhab, *Current Opinion in Colloid & Interface Science* **2011**, *16*, 36–40.

[18] H. G. Muller, An introduction to food rheology. **1973**.

[19] R. B. Bird, R. C. Armstrong, O. Hassager, Dynamics of polymeric liquids. Vol. 1, 2nd Ed. : Fluid mechanics, John Wiley and Sons Inc.,New York, NY, **1986**.

[20] J. G. Oldroyd, *Proceedings of the Royal Society of London. Series A. Mathematical and Physical Sciences* **1965**, *283*, 115–133.

[21] N. Phan-Thien, N. Mai-Duy, Understanding viscoelasticity: An introduction to rheology, Springer, **2013**.

[22] M. M. Cross, *Journal of colloid and Interface Science* **1968**, *27*, 84–90.

[23] F. Irgens, Rheology and Non-Newtonian fluids, Springer, **2014**.

[24] N. O. Jaensson, P. D. Anderson, J. Vermant, *Journal of Non-Newtonian Fluid Mechanics* **2021**, *290*, 104507.

[25] Y. El Omari, M. Yousfi, J. Duchet-Rumeau, A. Maazouz, *Polymers* **2022**, *14*, 2844.

[26] P. Rostami, A. Erb, R. Azizmalayeri, J. Steinmann, R. W. Stark, G. K. Auernhammer, *Physical Review Fluids* **2025**, *10*, 063603.

[27] M. Kansal, PhD thesis, University of Twente, **2024**.

[28] L. Afferrante, G. Violano, G. Carbone, *Scientific Reports* **2023**, *13*, 15060.

[29] J. Boujlel, P. Coussot, *Soft Matter* **2013**, *9*, 5898–5908.

[30] L. Jørgensen, M. Le Merrer, H. Delanoë-Ayari, C. Barentin, *Soft Matter* **2015**, *11*, 5111–5121.

[31] J. Yan Chan Edgar, H. Wang, *Current Pharmaceutical Design* **2017**, *23*, 2108–2112.

[32] N. Kashaninejad, E. Moradi, H. Moghadas, *Progress in Molecular Biology and Translational Science* **2022**, *187*, 9–39.

[33] Q. Ma, J. Cao, Y. Gao, S. Han, Y. Liang, T. Zhang, X. Wang, Y. Sun, *Nanoscale* **2020**, *12*, 15512–15527.

[34] S. U. Choi in ASME international mechanical engineering congress and exposition, *Vol. 17421*, American Society of Mechanical Engineers, **1995**, pp. 99–105.

[35] E. Michaelides, Nanofluidics, Springer, **2014**.

[36] S. U. Choi, Nanofluids: A new field of scientific research and innovative applications, **2008**.

[37] M. Spivak, Calculus on manifolds: a modern approach to classical theorems of advanced calculus, CRC press, **2018**.

[38] I. Newton, Philosophiae naturalis principia mathematica, G. Brookman, **1833**.

[39] B. E. Rapp, Microfluidics: modeling, mechanics and mathematics, Elsevier, **2016**.

[40] E. K. Fischer, *Journal of Colloid Science* **1950**, *5*, 271–281.

[41] S. Park, M.-G. Chung, B. Yoo, *Starch/Stärke* **2004**, *56*, 399–406.

[42] W. H. Herschel, R. Bulkley, *Kolloid-Zeitschrift* **1926**, *39*, 291–300.

[43] T. Voigtmann, *Current opinion in colloid & interface science* **2014**, *19*, 549–560.

[44] C. Truesdell, W. Noll, The non-linear field theories of mechanics, Springer, **2004**, pp. 1–579.

[45] O. Reynolds, *Philosophical transactions of the Royal Society of London* **1886**, *177*, 157–234.

[46] A. Oron, S. H. Davis, S. G. Bankoff, *Reviews of Modern Physics* **1997**, *69*, 931.

[47] M. Jalaal, PhD thesis, University of British Columbia, **2016**.

[48] M. Rauscher, A. Münch, B. Wagner, R. Blossey, *The European Physical Journal E* **2005**, *17*, 373–379.

[49] B. Lautrup, Physics of continuous matter: exotic and everyday phenomena in the macroscopic world, CRC press, **2011**.

[50] M. Whitby, N. Quirke, *Nature nanotechnology* **2007**, *2*, 87.

[51] J. S. Hansen, Nanoscale Hydrodynamics of Simple Systems, Cambridge University Press, **2022**.

[52] W. Van Saarloos, V. Vitelli, Z. Zeravcic, Soft Matter: Concepts, Phenomena, and Applications, Princeton University Press, **2024**.

[53] M. Majumder, N. Chopra, R. Andrews, B. Hinds, *Enhanced flow in carbon nanotubes. Nature* **2005**, *438*, 44.

[54] S. K. Kannam, B. Todd, J. S. Hansen, P. J. Daivis, *The Journal of Chemical Physics* **2013**, *138*.

[55] L. Joly, *The Journal of Chemical Physics* **2011**, *135*, 214705.

[56] D. Dimitrov, A. Milchev, K. Binder, *Physical Review Letters* **2007**, *99*, 054501.

[57] L. Fumagalli, A. Esfandiar, R. Fabregas, S. Hu, P. Ares, A. Janardanan, Q. Yang, B. Radha, T. Taniguchi, K. Watanabe, G. Gomila, K. S. Novoselov, A. K. Geim, *Science* **2018**, *360*, 1339–1342.

[58] S. De Luca, S. K. Kannam, B. Todd, F. Frascoli, J. S. Hansen, P. J. Daivis, *Langmuir* **2016**, *32*, 4765–4773.

[59] B. Todd, J. Hansen, P. J. Daivis, *Physical Review Letters* **2008**, *100*, 195901.

[60] S. Knudsen, B. D. Todd, J. S. Hansen, *Physics of Fluids* **2025**, *37*, 012021.

[61] M. S. Daw, M. I. Baskes, *Physical Review B* **1984**, *29*, 6443.

[62] Y. Mishin, M. J. Mehl, D. A. Papaconstantopoulos, A. F. Voter, J. D. Kress, *Physical Review B* **2001**, *63*, 224106.

[63] D. S. Cerutti, D. A. Case, *Wiley Interdisciplinary Reviews: Computational Molecular Science* **2019**, *9*, e1402.

[64] W. Kob, H. C. Andersen, *Physical Review E* **1995**, *52*, 4134.

[65] K. Vollmayr, W. Kob, K. Binder, *Physical Review B* **1996**, *54*, 15808.

[66] A. Cormack, Y. Cao, *Molecular Engineering* **1996**, *6*, 183–227.

[67] M. Benoit, S. Ispas, P. Jund, R. Jullien, *The European Physical Journal B-Condensed Matter and Complex Systems* **2000**, *13*, 631–636.

[68] A. Rahman, F. H. Stillinger, *The Journal of Chemical Physics* **1971**, *55*, 3336–3359.

[69] M. P. Allen, D. J. Tildesley, Computer simulation of liquids, Oxford University Press, **2017**.

[70] D. Frenkel, B. Smit, Understanding Molecular Simulation: From Algorithms to Applications, Elsevier, **2023**.

[71] J. E. Jones, *Proceedings of the Royal Society. Series A* **1924**, *106*, 441–462.

[72] J. A. White, *The Journal of Chemical Physics* **1999**, *111*, 9352–9356.

[73] Y. Li, X. Zhang, L. Shen, *Journal of Materials Informatics* **2025**, *5*, N–A.

[74] T. Liang, K. Xu, E. Lindgren, Z. Chen, R. Zhao, J. Liu, E. Berger, B. Tang, B. Zhang, Y. Wang, K. Song, P. Ying, N. Xu, H. Dong, S. Chen, P. Erhart, Z. Fan, T. Ala-Nissila, J. Xu, *arXiv preprint arXiv:2504.21286* **2025**.

[75] A. A. Chialvo, P. G. Debenedetti, *Computer Physics Communications* **1990**, *60*, 215–224.

[76] Z. Yao, J.-S. Wang, G.-R. Liu, M. Cheng, *Computer Physics Communications* **2004**, *161*, 27–35.

[77] W. Gautschi, Numerical analysis, Springer Science & Business Media, **2011**.

[78] L. Verlet, *Physical Review* **1967**, *159*, 98.

[79] L. Verlet in Faraday Symposia of the Chemical Society, *Vol. 6*, Royal Society of Chemistry, **1972**, pp. 116–121.

[80] E. Hairer, C. Lubich, *Numerische Mathematik* **2016**, *134*, 119–138.

[81] W. C. Swope, H. C. Andersen, P. H. Berens, K. R. Wilson, *The Journal of Chemical Physics* **1982**, *76*, 637–649.

[82] P. M. Rodger, *Molecular Simulation* **1989**, *3*, 263–269.

[83] S. Toxvaerd, *Molecular Physics* **1991**, *72*, 159–168.

[84] J. Kolafa, *The Journal of Chemical Physics* **2005**, *122*, 164105.

[85] L.-J. Hou, Z. Mišković, *arXiv preprint arXiv:0806.3912* **2008**.

[86] G. J. Martyna, M. E. Tuckerman, *The Journal of Chemical Physics* **1995**, *102*, 8071–8077.

[87] S. Nosé, *Molecular physics* **2002**, *100*, 191–198.

[88] H. J. Berendsen, J. v. Postma, W. F. Van Gunsteren, A. DiNola, J. R. Haak, *The Journal of Chemical Physics* **1984**, *81*, 3684–3690.

[89] H. C. Andersen, *The Journal of Chemical Physics* **1980**, *72*, 2384–2393.

[90] W. G. Hoover, *Physical Review A* **1985**, *31*, 1695.

[91] M. Parrinello, A. Rahman, *Journal of Applied physics* **1981**, *52*, 7182–7190.

[92] J.-P. Hansen, I. R. McDonald, Theory of simple liquids: with applications to soft matter, Academic press, **2013**.

[93] D. J. Griffiths, D. F. Schroeter, Introduction to quantum mechanics, Cambridge University Press, **2018**.

[94] J. S. Rowlinson, B. Widom, Molecular theory of capillarity, Courier Corporation, **2013**.

[95] G. Navascues, *Reports on Progress in Physics* **1979**, *42*, 1131.

[96] R. E. Rozas, J. Horbach, *Europhysics Letters* **2011**, *93*, 26006.

[97] L. Berthier, D. R. Reichman, *Nature Reviews Physics* **2023**, *5*, 102–116.

[98] D. R. Reichman, P. Charbonneau, *Journal of Statistical Mechanics: Theory and Experiment* **2005**, *2005*, P05013.

[99] L. Berthier, G. Biroli, *Reviews of Modern Physics* **2011**, *83*, 587–645.

[100] W. Kob, H. C. Andersen, *Physical Review Letters* **1994**, *73*, 1376.

[101] S. Paliwal, V. Prymidis, L. Filion, M. Dijkstra, *The Journal of Chemical Physics* **2017**, *147*, 084902.

[102] H. Peng, H. Liu, T. Voigtmann, *Physical Review Letters* **2022**, *129*, 215501.

[103] T. Peng, Q. Li, L. Xu, C. He, L. Luo, *Entropy* **2017**, *19*, 620.

[104] D. J. Evans, G. Morriss, *Physical Review A* **1984**, *30*, 1528.

[105] P. J. Daivis, B. D. Todd, *The Journal of Chemical Physics* **2006**, *124*, 194103.

[106] B. D. Todd, P. J. Daivis, Nonequilibrium molecular dynamics: theory, algorithms and applications, Cambridge University Press, **2017**.

[107] M. E. Tuckerman, C. J. Mundy, S. Balasubramanian, M. L. Klein, *The Journal of Chemical Physics* **1997**, *106*, 5615–5621.

[108] B. Edwards, C. Baig, D. Keffer, *The Journal of Chemical Physics* **2006**, *124*, 194104.

[109] G. Marcelli, T. Bottinelli Montandon, R. Ebrahimi Viand, F. Höfling, *The Journal of Chemical Physics* **2025**, *162*, 104101.

[110] C. Niethammer, S. Becker, M. Bernreuther, M. Buchholz, W. Eckhardt, A. Heinecke, S. Werth, H.-J. Bungartz, C. W. Glass, H. Hasse, J. Vrabec, M. Horsch, *Journal of chemical theory and computation* **2014**, *10*, 4455–4464.

[111] N. Bailey, T. Ingebrigtsen, J. S. Hansen, A. Veldhorst, L. Bøhling, C. Lemarchand, A. Olsen, A. Bacher, L. Costigliola, U. Pedersen, H. Larsen, J. Dyre, T. Schrøder, *SciPost Physics* **2017**, *3*, 038.

[112] gamdpy, GPU-Accelerated Molecular-Dynamics in Python, https://github.com/ThomasBechSchroeder/gamdpy.

[113] Basilisk: Adaptive Cartesian Grid CFD Framework, basilisk.fr/.

[114] R. Courant, K. Friedrichs, H. Lewy, *Mathematische Annalen* **1928**, *100*, 32–74.

[115] J. B. Bell, P. Colella, H. M. Glaz, *Journal of Computational Physics* **1989**, *85*, 257–283.

[116] P. Colella, *Journal of Computational Physics* **1990**, *87*, 171–200.

[117] S. Popinet, *Journal of Computational Physics* **2015**, *302*, 336–358.

[118] R. Keunings, *Journal of Non-Newtonian Fluid Mechanics* **1986**, *20*, 209–226.

[119] P. Daripa, G. Paşa, *Institutul de Matematica "Simion Stoilow" al Academiei Romane* **2017**, 1–21.

[120] R. Comminal, J. Spangenberg, J. H. Hattel, *Journal of Non-Newtonian Fluid Mechanics* **2015**, *223*, 37–61.

[121] P. Knechtges, M. Behr, S. Elgeti, *Journal of Non-Newtonian Fluid Mechanics* **2014**, *214*, 78–87.

[122] S. Tanriverdi, J. Cruz, S. Habibi, T. Sych, M. Costa, G. Mårtensson, A. Görgens, S. E. Andaloussi, L. Brandt, O. Tammisola, E. Sezgin, A. Russom, *Small* **2025**, 2503369.

[123] S. Habibi, K. T. Iqbal, M. N. Ardekani, E. Chaparian, L. Brandt, O. Tammisola, *Journal of Fluid Mechanics* **2025**, *1007*, A36.

[124] N. J. Balmforth, I. A. Frigaard, G. Ovarlez, *Annual Review of Fluid Mechanics* **2014**, *46*, 121–146.

[125] P. Coussot, Rheophysics: Matter in all its States, Springer, New York, **2014**.

[126] J. K. Placone, A. J. Engler, *Advanced Healthcare Materials* **2018**, *7*, 1701161.

[127] S. Kyle, Z. M. Jessop, A. Al-Sabah, I. S. Whitaker, *Advanced Healthcare Materials* **2017**, *6*, 1700264.

[128] Z. Jiang, B. Diggle, M. L. Tan, J. Viktorova, C. W. Bennett, L. A. Connal, *Advanced Science* **2020**, *7*, 2001379.

[129] R. A. Buswell, W. L. De Silva, S. Z. Jones, J. Dirrenberger, *Cement and Concrete Research* **2018**, *112*, 37–49.

[130] J. van der Kolk, D. Tieman, M. Jalaal, *Journal of Fluid Mechanics* **2023**, *958*, A34.

[131] S. L. Cormier, J. D. McGraw, T. Salez, E. Raphaël, K. Dalnoki-Veress, *Physical Review Letters* **2012**, *109*, 154501.

[132] M. S. Agrawal, H. S. Gaikwad, P. K. Mondal, G. Biswas, *Applied Mathematical Modelling* **2019**, *75*, 201–209.

[133] H. L. França, M. Jalaal, C. M. Oishi, *Physical Review Research* **2024**, *6*, 013226.

[134] J. D. Shemilt, A. B. Thompson, A. Horsley, C. A. Whitfield, O. E. Jensen, *Physical Review Fluids* **2025**, *10*, 103301.

[135] H. Kim, S. Q. Choi, *Journal of Fluid Mechanics* **2024**, *996*, A48.

[136] T. V. Ball, N. J. Balmforth, *Physical Review Fluids* **2024**, *9*, 023304.

[137] P. Rostami, M. Fricke, S. Schubotz, H. Patel, R. Azizmalayeri, G. K. Auernhammer, *Journal of Fluid Mechanics* **2024**, *988*, A51.

[138] J. D. Shemilt, A. Horsley, O. E. Jensen, A. B. Thompson, C. A. Whitfield, *Journal of Fluid Mechanics* **2022**, *944*, A22.

[139] M. Jalaal, C. Seyfert, J. H. Snoeijer, *Journal of Fluid Mechanics* **2019**, *880*, 430–440.

[140] N. Paxton, W. Smolan, T. Böck, F. Melchels, J. Groll, T. Jungst, *Biofabrication* **2017**, *9*, 044107.

[141] J. M. Townsend, E. C. Beck, S. H. Gehrke, C. J. Berkland, M. S. Detamore, *Progress in Polymer Science* **2019**, *91*, 126–140.

[142] M. Milazzo, V. Fitzpatrick, C. E. Owens, I. M. Carraretto, G. H. McKinley, D. L. Kaplan, M. J. Buehler, *ACS Biomaterials Science and Engineering* **2023**, *9*, 1285–1295.

[143] A. V. Ombergen, F. Chalupa-Gantner, P. Chansoria, B. M. Colosimo, M. Costantini, M. Domingos, A. Dufour, C. De Maria, J. Groll, T. Jungst, R. Levato, J. Malda, A. Margarita, C. Marquette, A. Ovsianikov, E. Petiot, S. Read, L. Surdo, W. Swieszkowski, G. Vozzi, J. Windisch, M. Zenobi-Wong, M. Gelinsky, *Advanced Healthcare Materials* **2023**, *12*, 2300443.

[144] A. Passerone, *Microgravity Science and Technology* **2011**, *23*, 101–111.

[145] A. Ababneh, A. Amirfazli, J. A. W. Elliott, *The Canadian Journal of Chemical Engineering* **2006**, *84*, 39–43.

[146] A. Diana, M. Castillo, D. Brutin, T. Steinberg, *Microgravity Science and Technology* **2012**, *24*, 195–202.

[147] A. Baldygin, A. Ahmed, R. Baily, M. F. Ismail, M. Khan, N. Rodrigues, A.-R. Salehi, M. Ramesh, S. Bhattacharya, T. Willers, et al., *npj Microgravity* **2023**, *9*, 49.

[148] B. Mielniczuk, O. Millet, G. Gagneux, M. S. El Youssoufi, *Granular Matter* **2018**, *20*, 14.

[149] J. McCraney, V. Kern, J. B. Bostwick, S. Daniel, P. H. Steen, *Physical Review Letters* **2022**, *129*, 084501.

[150] J. McCraney, J. Ludwicki, J. Bostwick, S. Daniel, P. Steen, *Physics of Fluids* **2022**, *34*, 122110.

[151] S. I. Tamim, J. B. Bostwick, *npj Microgravity* **2021**, *7*, 42.

[152] A. Saıdi, C. Martin, A. Magnin, *J. Non-Newtonian Fluid Mech.* **2010**, *165*, 596–606.

[153] B. Gorin, G. Di Mauro, D. Bonn, H. Kellay, *Langmuir* **2022**, *38*, 2608–2613.

[154] M. H. Biroun, L. Haworth, H. Abdolnezhad, A. Khosravi, P. Agrawal, G. McHale, H. Torun, C. Semprebon, M. Jabbari, Y.-Q. Fu, *Langmuir* **2023**, *39*, 5793–5802.

[155] A. Mobaseri, S. Kumar, X. Cheng, *Proceedings of the National Academy of Sciences of the United States of America* **2025**, *122*, e2500163122.

[156] S. Jung, S. D. Hoath, I. M. Hutchings, *Microfluidcis Nanofluidics* **2013**, *14*, 163–169.

[157] V. Bertola, *International Journal of Heat and Mass Transfer* **2009**, *52*, 1786–1793.

[158] H. Dittus, *Endeavour* **1991**, *15*, 72–78.

[159] P. Von Kampen, U. Kaczmarczik, H. J. Rath, *Acta Astronautica* **2006**, *59*, 278–283.

[160] H. Dittus, A. Schomisch, *Vacuum* **1990**, *41*, 2135–2137.

[161] O. D'Angelo, F. Kuthe, K. van Nieuwland, C. Ederveen Janssen, T. Voigtmann, M. Jalaal, *Review of Scientific Instruments* **2022**, *93*, 115103.

[162] M. Jalaal, N. J. Balmforth, B. Stoeber, *Langmuir* **2015**, *31*, 12071–12075.

[163] O. D'Angelo, L. Heitmeier, T. Voigtmann, VIP-DROP Experimental Data, DOI:10.5281/zenodo.15806543, **2025**.

[164] O. D'Angelo, L. Heitmeier, T. Voigtmann, VIP-DROP Experimental Data for PIV, DOI:10.5281/zenodo.15806731, **2025**.

[165] B. Barry, M. Meyer, *International Journal of Pharmaceutics* **1979**, *2*, 1–25.

[166] S. Curran, R. Hayes, A. Afacan, M. Williams, P. A. Tanguy, *Journal of Food Science* **2002**, *67*, 176–180.

[167] E. Di Giuseppe, F. Corbi, F. Funiciello, A. Massmeyer, T. Santimano, M. Rosenau, A. Davaille, *Tectonophysics* **2015**, *642*, 29–45.

[168] I. Frigaard, *Current Opinion in Colloid Interface Science* **2019**, *43*, 80–93.

[169] M. Jalaal, D. Kemper, D. Lohse, *Journal of Fluid Mechanics* **2019**, *864*, 596–613.

[170] G. Martouzet, L. Jørgensen, Y. Pelet, A.-L. Biance, C. Barentin, *Physical Review Fluids* **2021**, *6*, 044006.

[171] S. Popinet, *Journal of Computational Physics* **2009**, *228*, 5838–5866.

[172] A. Prosperetti, Computational Methods for Multiphase Flow, Cambridge University Press, **2009**.

[173] G. Tryggvason, R. Scardovelli, S. Zaleski, Direct numerical simulations of gas–liquid multiphase flows, Cambridge University Press, **2011**.

[174] A. G. Balasubramanian, V. Sanjay, M. Jalaal, R. Vinuesa, O. Tammisola, *Journal of Fluid Mechanics* **2024**, *1001*, A9.

[175] V. Sanjay, D. Lohse, M. Jalaal, *Journal of Fluid Mechanics* **2021**, *922*, A2.

[176] B. Zhang, V. Sanjay, S. Shi, Y. Zhao, C. Lv, X.-Q. Feng, D. Lohse, *Physical Review Letters* **2022**, *129*, 104501.

[177] M. Fuchs, M. E. Cates, *Faraday Discuss.* **2003**, *123*, 267–286.

[178] S. Papenkort, T. Voigtmann, *Journal of Chemical Physics* **2015**, *143*, 044512.

[179] J. L. White, A. B. Metzner, *Journal of Applied Polymer Science* **1963**, *7*, 1867–1889.

[180] J. White, A. Metzner, *AIChE Journal* **1965**, *11*, 324–330.

[181] J. G. Oldroyd, *Proceedings of the Royal Society A* **1950**, *200*, 523–541.

[182] L. H. Tanner, *Journal of Physics D* **1979**, *12*, 1473.

[183] G. Vázquez, E. Alvarez, R. Rendo, E. Romero, J. M. Navaza, *Journal of Chemical Engeering Data* **1996**, *41*, 806–808.

[184] G. German, V. Bertola, *Journal of Physics: Condensed Matter* **2009**, *21*, 375111.

[185] H. Mohammadigoushki, K. Shoele, *Langmuir* **2023**, *39*, 7672–7683.

[186] L. Tian, C. Bechinger, *Nature Communications* **2022**, *13*, 6605.

[187] P. Zhang, J. J. Maldonis, Z. Liu, J. Schroers, P. M. Voyles, *Nature Communications* **2018**, *9*, 1129.

[188] S. F. Swallen, K. L. Kearns, M. K. Mapes, Y. S. Kim, R. J. McMahon, M. D. Ediger, T. Wu, L. Yu, S. Satija, *Science* **2007**, *315*, 353–356.

[189] L. Berthier, P. Charbonneau, E. Flenner, F. Zamponi, *Physical Review Letters* **2017**, *119*, 188002.

[190] C. Rodriguez-Tinoco, M. Gonzalez-Silveira, M. A. Ramos, J. Rodriguez-Viejo, *Nuovo Cimento* **2022**, *45*, 325–406.

[191] M. D. Ediger, J. A. Forrest, *Macromolecules* **2014**, *47*, 471–478.

[192] G. G. Fuller, J. Vermant, *Annu. Rev. Chem. Biomol. Eng.* **2012**, *3*, 519–543.

[193] H. Ragelle, M. W. Tibbitt, S.-Y. Wu, M. A. Castillo, G. Z. Cheng, S. P. Gangadharan, D. G. Anderson, M. J. Cima, R. Langer, *Nature Communications* **2018**, *9*, 1184.

[194] C. Cammarota, A. Cavagna, G. Gradenigo, T. S. Grigera, P. Verrocchio, *Journal of Statistical Mechanics: Theory and Experiment* **2009**, L12002.

[195] D. Ganapathi, K. H. Nagamanasa, A. K. Sood, R. Ganapathy, *Nature Communications* **2018**, *9*, 397.

[196] N. J. Wagner, J. Mewis, Eds., Theory and Applications of Colloidal Suspension Rheology, Cambridge University Press, Cambridge, UK, **2021**.

[197] S. Plimpton, *Journal of Computational Physics* **1995**, *117*, 1–19.

[198] K. Birdi, Surface tension and interfacial tension of liquids, CRC: New York, **1997**.

[199] P.-G. Gennes, F. Brochard-Wyart, D. Quéré, et al., Capillarity and wetting phenomena: drops, bubbles, pearls, waves, Springer, **2004**.

[200] M. Durand, *American Journal of Physics* **2021**, *89*, 261–266.

[201] A. Marchand, J. H. Weijs, J. H. Snoeijer, B. Andreotti, *American Journal of Physics* **2011**, *79*, 999–1008.

[202] F. Varnik, J. Baschnagel, K. Binder, *J. Chem. Phys.* **2000**, *113*, 4444–4453.

[203] L. Heitmeier, T. Voigtmann, LAMMPS simulation script, Zenodo archive, DOI:10.5281/zenodo.16780956, **2025**.

[204] R. Evans, *Advances in physics* **1979**, *28*, 143–200.

[205] S. W. Sides, G. S. Grest, M.-D. Lacasse, *Physical Review E* **1999**, *60*, 6708.

[206] R. L. C. Vink, J. Horbach, K. Binder, *The Journal of Chemical Physics* **2005**, *122*, 134905.

[207] J. F. Lutsko, C. Schoonen, *Physical Review E* **2020**, *102*, 062136.

[208] D. J Evans, G. P Morriss, Statistical mechanics of nonequilbrium liquids, ANU Press, **2007**.

[209] A. Pelofsky, *Journal of Chemical and Engineering Data* **1966**, *11*, 394–397.

[210] G. Di Nicola, M. Pierantozzi, S. Tomassetti, G. Coccia, *Fluid Phase Equilibria* **2018**, *463*, 11–17.

[211] G. Sun, S. Saw, I. Douglas, P. Harrowell, *Physical Review Letters* **2017**, *119*, 245501.

[212] U. M. B. Marconi, C. Maggi, S. Melchionna, *Soft Matter* **2016**, *12*, 5727–5738.

[213] T. Speck, *Europhysics Letters* **2016**, *114*, 30006.

[214] J.-L. Barrat, L. Berthier, *Phys. Rev. E* **2000**, *63*, 012503.

[215] J. M. Brader, T. Voigtmann, M. Fuchs, R. G. Larson, M. E. Cates, *Proc. Natl. Acad. Sci. USA* **2009**, *106*, 15186–15191.

[216] C. F. Brooks, G. G. Fuller, C. W. Frank, C. R. Robertson, *Langmuir* **1999**, *15*, 2450–2459.

[217] T. Verwijlen, P. Moldenaers, H. A. Stone, J. Vermant, *Langmuir* **2011**, *27*, 9345–9358.

[218] N. Jaensson, J. Vermant, *Curr. Opin. Colloid Interf. Sci.* **2018**, *37*, 136–150.

[219] S. Naghieh, X. Chen, *J. Pharmaceutical Analysis* **2021**, *11*, 564–579.

[220] S. Geisel, E. Secchi, J. Vermant, *Interface Focus* **2022**, *12*, 20220032.

[221] S. G. V. Charlton, A. N. Bible, E. Secchi, J. L. Morrell-Falvey, S. T. Retterer, T. P. Curtis, J. Chen, S. Jana, *Advanced Science* **2023**, *10*, 2207373.

[222] C. Clarke, F. Spyropoulos, I. T. Norton, *Phys. Fluids* **2019**, *31*, 092002.

[223] C. Clarke, F. Spyropoulos, I. T. Norton, *J. Colloid Interface Sci.* **2020**, *573*, 348–359.

[224] N. Bain, A. Jagota, K. Smith-Mannschott, S. Heyden, R. W. Style, E. R. Dufresne, *Phys. Rev. Lett.* **2021**, *127*, 208001.

[225] R. W. Style, A. Jagota, C.-Y. Hui, E. R. Dufresne, *Annual Review of Condensed Matter Physics* **2017**, *8*, 99–118.

[226] J. Koplik, J. Banavar, J. Willemsen, *Physics of Fluids* **1989**, *1*, 781–794.

[227] K. P. Travis, D. J. Evans, *Physical Review E* **1997**, *55*, 1566.

[228] J. S. Hansen, *Molecular Simulations* **2021**, *47*, 1391.

[229] K. P. Travis, B. D. Todd, D. J. Evans, *Physical Review E* **1997**, *55*, 4288–4295.

[230] A. Furukawa, H. Tanaka, *Physical Review Letters* **2009**, *103*, 135703.

[231] J. D. Bonthuis, D. Horinek, L. Bocquet, R. R. Netz, *Physical Review Letters* **2009**, *103*, 144503.

[232] F. Bresme, A. Lervik, D. Bedaux, S. Kjelstrup, *Physical Review Letters* **2008**, *101*, 020602.

[233] S. R. de Groot, P. Mazur, Non-equilibrium Thermodynamics, Dover Publications, **1984**.

[234] J. Dahler, L. Scriven, *Proceedings of the Royal Society A* **1963**, *275*, 504.

[235] D. J. Evans, W. B. Streett, *Molecular Physics* **1978**, *36*, 161–176.

[236] I. M. de Schepper, E. G. D. Cohen, C. Bruin, J. C. van Rijs, W. Montfrooij, L. A. de Graaf, *Physical Review A* **1988**, *38*, 271.

[237] R. Horn, J. Israelachvili, *Journal of Chemical Physics* **1981**, *83*, 5311.

[238] S. Toxvaerd, E. Præstgaard, *Journal of Chemical Physics* **1977**, *67*, 5291.

[239] S. R. Carlson, R. R. Netz, *Nano Letters* **2025**, *25*, 15605–15612.

[240] I. Bitsanis, J. Magda, M. Tirrell, H. Davis, *Journal of Chemical Physics* **1987**, *87*, 1733.

[241] I. Bitsanis, T. Vanderlick, M. Tirrell, H. Davis, *Journal of Chemical Physics* **1988**, *89*, 3152.

[242] S. Knudsen, B. Todd, J. S. Hansen, *Physics of Fluids* **2025**, *37*, 012021.

[243] B. Dalton, P. Daivis, J. Hansen, B. Todd, *Physical Review E* **2013**, *88*, 052143.

[244] B. Dalton, K. Glavatskiy, P. Daivis, *Physical Review E* **2015**, *92*, 012108.

[245] J. S. Hansen, P. J. Daivis, B. D. Todd, *Journal of Chemical Physics* **2007**, *126*, 144706.

[246] N. Tschoegl, The Phenomenological Theory of Linear Viscoelastic Behavior, Springer-Verlag, **1989**.

[247] H. Mizuno, R. Yamamoto, *Physical Review Letters* **2013**, *110*, 095901.

[248] J. Hansen, *Physical Review E* **2024**, *110*, L023101.

[249] R. Sadus, Molecular Simulation of Fluids. Theory, Algorithms and Object-Orientation, Elsevier, **1999**.

[250] D. Frenkel, B. Smit, Understanding Molecular Simulation, Academic Press, London, **1996**.

[251] J. S. Hansen, P. J. Daivis, K. P. Travis, B. D. Todd, *Physical Review E* **2007**, *76*, 041121.

[252] C. Colosqui, H. Chen, X. Shan, I. Staroselsky, V. Yakhot, *Physics of Fluids* **2009**, *21*, 013105.

[253] C. Colosqui, *Physical Review E* **2010**, *81*, 026702.

[254] I. Mryglod, *Condensed Matter of Physics* **1998**, *1*, 753.

[255] This is used under Python's lmfit package.

[256] R. Gutenkunst, N. Ryan, J. Waterfall, F. Casey, P. Fergal, K. Brown, C. Myers, J. Sethna, *PLOS Comp. Biol.* **2007**, *3*, 1.

[257] S. Frederiksen, K. Jacobsen, K. Brown, J. Sethna, *Physical Review Letters* **2004**, *93*, 165501.

[258] T. Bryk, I. Mryglod, G. Ruocco, *Philosophical Magazine* **2020**, *100*, 2568.

[259] S. Papenkort, T. Voigtmann, *Journal of Chemical Physics* **2015**, *143*, 204502.

[260] J. Vogel, F. Schaff, A. Fehringer, C. Jud, M. Wieczorek, F. Pfeiffer, T. Lasser, *Optics Express* **2015**, *23*, 15134–15151.

[261] M. Defrise, G. T. Gullberg, *Lawrence Berkeley National Laboratory* **2005**, `https://api.semanticscholar.org/CorpusID:62840074`.

[262] H. Aben, C. Guillemet in Photoelasticity of Glass, Springer, **2012**, pp. 86–101.

[263] N. F. Osman, J. L. Prince, *Inverse problems* **1998**, *14*, 185.

[264] J. S. Allen, R. A. Roy, *The Journal of the Acoustical Society of America* **2000**, *107*, 3167–3178.

[265] J. S. Allen, R. A. Roy, *The Journal of the Acoustical Society of America* **2000**, *108*, 1640–1650.

[266] B. C. Sessa, F. Cao, R. A. Pelcovits, T. R. Powers, G. Duclos, *arXiv preprint arXiv:2506.17532* **2025**.

[267] J. K. Wilt, N. Schramma, J.-W. Bottermans, M. Jalaal, *arXiv preprint arXiv:2411.16011* **2024**.

[268] J. Bialké, J. T. Siebert, H. Löwen, T. Speck, *Physical Review Letters* **2015**, *115*, 098301.

[269] M. E. Cates, C. Nardini, *Reports on Progress in Physics* **2025**, *88*, 056601.

[270] A. K. Omar, Z.-G. Wang, J. F. Brady, *Physical Review E* **2020**, *101*, 012604.

[271] N. Lauersdorf, T. Kolb, M. Moradi, E. Nazockdast, D. Klotsa, *arXiv preprint arXiv:2106.02008* **2021**.

[272] J. M. Brader, T. Voigtmann, M. Fuchs, R. G. Larson, M. E. Cates, *Proceedings of the National Academy of Sciences* **2009**, *106*, 15186–15191.

[273] T. F. Farage, J. Reinhardt, J. M. Brader, *Physical Review E* **2013**, *88*, 042303.

[274] A. Alicke, J. Vermant, *Rheologica Acta* **2025**, *64*, 583–600.

[275] A. Alicke, PhD thesis, ETH Zurich, **2021**.

Acknowledgements

First and foremost, I would like to thank **Prof. Dr. Thomas Voigtmann**, who was not only my PhD supervisor but also the person who first inspired me to study physics by introducing me to the fascinating field of soft matter very early in my academic career. I am deeply thankful for his continuous guidance and support throughout the past years. I have greatly enjoyed our collaboration and sincerely hope that it will continue beyond the completion of my PhD.

Additionally, I would like to express my gratitude to my second examiner, **Prof. Dr. Hartmut Löwen**, for taking the time to review my thesis and for providing insightful comments and suggestions that have greatly improved the quality of this work. His constructive feedback and perspective were highly appreciated.

Furthermore, I wish to express my gratitude to **Prof. Dr. Jesper S. Hansen**. I have always enjoyed our collaboration and greatly value the time he dedicated to our discussions. Through his guidance, I was introduced to the field of hydrodynamics on the nanoscale during my PhD, which played a crucial role in shaping this work and allowed me to complete my thesis much faster than expected.

I would also like to extend my thanks to the members of the **Glass & Time Group** at Roskilde University, in particular **Prof. Dr. Jeppe Dyre**. I am very grateful not only for the opportunity to work with him during August 2024, but also for his valuable advice and guidance during that period.

Special thanks go to my colleagues and friends from my stay in Denmark **Lorenzo, Danqi, Krishna, Francesco, and Pablo** for their infectious enthusiasm, memorable moments, and the many activities we shared inside and outside the lab — from cooking together to biking and running adventures in and around Roskilde.

I would also like to thank **Olfa D'Angelo**, not only for our productive collaboration and numerous discussions in the last time, but also for appreciating even my very first steps of investigating.

My gratitude further extends to all my colleagues at DLR with whom I had the pleasure to collaborate. In particular, I thank **Leon Granz** for teaching me how to use the HPC cluster effectively. I am also grateful to **Dr. Johannes Sandberg, Stephan Domann, Paulina Blair, Martin Weiß,** and **Dr. Till Böhmer** for many fruitful discussions. My special thanks go to **Dr. Jan Gabriel**, whose ideas and enthusiasm for the physics of aging were always a source of inspiration and motivation.

I would further like to thank my collegues **Katharina Dammer, Marlo Kunzner, Dr. Benedikt Reiplinger, Johannes Thore,** and **Martin Uttendorfer,** who reminded me that taking breaks is just as important as working hard during a PhD.
Then, I would also like to express my gratitude to **Sumeja Burekovic** for carefully proofreading large parts of this thesis and providing highly constructive feedback.

Finally, I owe my deepest gratitude to my family and friends for supporting me with their patience, understanding and encouragement during the researching and writing periods of this thesis.

Addendum

In addition to the papers presented above, I have coauthored the following works that have not yet been published at the time of thesis submission. Preprints of these works are included here for the reviewers' discretion.

- Yuna Kato, Jürgen Brillo, Dirk Holland-Moritz, Fan Yang, Thomas C. Hansen, Thomas Voigtmann and **Linnea Heitmeier** (2026): Molecular Dynamics simulations of Al-Ti metallic alloy melts using a transferable machine-learning potential, (see arXiv:2604.26362)

  My contribution to this paper included the conceptualization, the planning and supervision of the project, the interpretation of the simulation results, and writing the draft.

- **Linnea Heitmeier** and Thomas Voigtmann (2026): A thin-film analysis of viscoelastic shear-thinning fluids using a droplet geometry

  My contribution to this paper included the conceptualization, the conduction of the analytical calculations, the conduction and analysis of the simulations, and writing the draft.

- **Linnea Heitmeier** and Jesper S. Hansen (2026): Velocity profiles of butane in a nanochannel

  My contribution to this paper included the conceptualization, the conduction of the analytical calculations, the conduction,

analysis and interpretation of the simulations, and writing the draft.

- **Linnea Heitmeier** and Jan Gabriel (2026): Particle Dynamics in Vibrated Granular Systems: A DEM Study (see arXiv:2603.01921)

  My contribution to this paper included the conduction, analysis and interpretation of the simulations, and writing the draft.

Molecular Dynamics simulations of Al-Ti metallic alloy melts using a transferable machine-learning potential

We investigate the structural and dynamical properties of binary metallic alloys, consisting of Aluminum and Titanium, in dependence of temperature and composition. For this, we make use of MD-simulations, using a transferable machine-learning potential, developed by Song et al. [1] and compare our results to experimental data.
Although this potential was initially trained on solid properties, we find a very good agreement between the experimental data and the simulation results for the liquid state.
Specifically, we find a qualitative agreement in the study of the excess volume, which shows that the mixing mechanisms between the different atoms can be reproduced by the potential. Also for dynamical properties like the viscosity and the diffusion coefficient, we obtain a qualitative agreement.

Introduction

As alloys are produced from their melts, exact knowledge of the thermophysical properties of the melts is important [2–4]. Owing to their low density and high tensile strength, Al-based alloys play a key role in aeronautic and automotive applications [5–8]. The binary aluminum alloys where Al is combined with a semi-noble metal provide good reference systems, and thus have been the focus of experimental and computational studies: for example AlNi and AlFe [9], AlAg and AlCu [10], AlAu [11, 12], or AlTi [13, 14]. Especially AlTi is an exciting material due to its high melting temperature, strong chemical bonding, and technological relevance in lightweight, high-strength applications.

Molecular Dynamics simulations access the relevant length- and time scales to predict thermophysical and transport properties of melts, in particular as input quantities for further coarse-grained simulations of material properties. However, they rely on ultimately empirical interaction potentials between the atoms to describe a specific system. The search for a suitable interaction model is generally laborious and time consuming. Traditional approaches include the EAM or similar empirical fits to force fields determined in quantum-mechanical calculations.

A more modern approach is to use machine-learning methods for the task of approximating the interparticle forces as functions of the atomic positions. Typically ab initio simulation data are used to train a neural network representing the interaction potential, including also solid-state experimental properties. This approach is increasingly gaining traction in the description of alloy melts [15–18]. In principle, neural network potentials can be transferrable: once trained on a sufficiently large training set, a suitably large neural network has the capability of describing not just a specific alloy but rather a larger set of materials. However, the performance in comparison to experimental data related to the melt remains to be checked, since also a neural-network-based potential can only be as good as the underlying ab initio calculation.

In the present study we investigate the predictive capabilities of a recent proposal of a very broadly transferable machine learning potential, the NEP-potential NEP89 [19], for the dynamics of AlTi alloy melts. The model has been trained on a large basis of data, and models of the same architecture have demonstrated success in the simulation of nanostructures [20], diamonds [21], and HCP-zirconium [22]. By performing MD-simulations using NEP89 for AlTi melts and comparing key thermophysical properties and transport coefficients with the available experimental data, we provide a stringent test for the transferability of the potential in a highly application-relevant context. This provides a key validation for the potential for AlTi systems.

We evaluate both structural and dynamical properties of AlTi melts for different compositions and temperatures. We observe good agreement with experimental data in general, emphasizing the generality of the NEP potential.

The paper is structured as follows: We start by investigating the composition dependent atomic volumes of the binary alloys, and especially the atomic excess volume which quantifies the deviation from the ideal-solution behavior which is identical to the linear combination of the atomic volumes of the pure unmixed elements. Similar to other Al-composites [11], the excess volume becomes negative, and its minimal value corresponds to the same concentration in both experiment and simulations. The fact that with the potential, we can reproduce this data, shows that the potential also covers the mixing mechanism, which depend on chemical interactions between the two kinds of particles. We also study the structure of the liquid microscopically. We also get a quantitative agreement between the structure factors from the simulations and the structure factors, which were measured experimentally by using neutron diffraction [23]. We find that the mixing behavior of the alloy significantly derivatives from the expectations of hard-spheres, but they can be well compared to the soft-sphere model.

In terms of dynamical properties, we studied the behavior of the

viscosity, where also an agreement between simulations and experiments was found. Specifically, we see that the qualitative behavior of the concentration-dependence of the viscosity is similar to the one found in other alloys, which include Al, like AlAu [11].

We conclude the paper by a discussion of the diffusion coefficients.

Methods

Computer simulations

We perform Molecular-Dynamics simulations using the open-source software `LAMMPS` [24]. As an interatomic potential, we employ the models developed by [1] and [19]. Unless stated otherwise, all simulations are carried out with N=10000 atoms and periodic boundary conditions in all three spatial directions. The equations of motion are integrated using the standard velocity-Verlet algorithm with a time step of 0.001 ps.

Each simulation run is first equilibrated at 2000 K for 500 ps and then cooled down to the desired temperature in the NPT ensemble (constant particle number, zero external pressure, and linearly decreasing temperature) for 10 ps. After further equilibration at the desired temperature, production runs are performed for a time of 200 ps. Temperatures considered in this work are T = 1550, 1650, 1720, 1800, 1873, 1950, 2000, 2100, and 2200 K, Compositions, i.e., the Aluminium mole fractions, are given in units of atomic-%, and include $x_{\mathrm{Al}} = 0\%$, 10%, 20%, 30%, 40%, 50%, 60%, 70%, 80%, 90%, and 100%.

The density is obtained by

$$\rho = \frac{N \cdot (x_{\mathrm{Al}} \cdot m_{\mathrm{Al}} + x_{\mathrm{Ti}} \cdot m_{\mathrm{Ti}})}{V} \tag{A.1}$$

where x_i is the concentration of the respective element, m_i is the corresponding atomic mass, N is the number of particles in the box,

and V is the volume of the system.
For the atomic masses, we used values of $m_{\mathrm{Ti}} = 47.86u$ and $m_{\mathrm{Al}} = 26.98u$.

The viscosity η is determined by the Green-Kubo-relation, using the stress-autocorrelation function of the off-diagonal stress tensor elements:

$$\eta = \frac{V}{k_B T} \cdot \int_0^\infty dt' \langle P_j(0) P_j(t') \rangle_{j \in \{(xy),(xz),(yz)\}} \tag{A.2}$$

where T is the temperature, k_B is the Boltzmann constant, t' is the time, and the P's are the off diagonal elements of the stress tensor. The diffusion coefficient D was calculated using the long-time behavior of the mean-squared displacement (MSD) in three dimensions, according to the Einstein relation:

$$D = \frac{\langle |\mathbf{r}(t) - \mathbf{r}(0)|^2 \rangle}{6t}, \tag{A.3}$$

where $\mathbf{r}(t)$ is the position vector of an atom at time t. The radial distribution function (RDF) was calculated by

$$g(r) = \frac{1}{4\pi r^2 \Delta r \rho N} \sum_{i=1}^{N} \sum_{j \neq i} \chi_{[r, r+\Delta r)}(r_{ij}) \tag{A.4}$$

where ρ is the number density, Δr is the width of the bin, and $\chi(x)$ is 1 when $x \in [r, r + \Delta r)$ and 0 otherwise. The function qualifies the probability of finding a particle at a distance r from a reference particle, normalized by the average density.

The coordination number (CN) was evaluated using two different approaches following the calculation of the radial distribution function (RDF). The first method is based on the integration of the first peak of the radial distribution function $g(r)$. With this method, the coordination number is given by

$$CN = 4\pi\rho \int_0^{r_c} r^2 g(r)\, dr, \tag{A.5}$$

where ρ is the atomic number density and r_c is the cutoff distance corresponding to the first minimum of $g(r)$. This integration yields the average number of neighboring atoms within the first coordination shell. The second method utilizes atomic configurations obtained from the simulations. For each atom i, the number of neighboring atoms j within the cutoff radius r_c was directly counted as

$$CN_i = \sum_{j \neq i} \Theta(r_c - r_{ij}), \tag{A.6}$$

where r_{ij} is the distance between atoms i and j, and Θ is the Heaviside step function. The average coordination number was then obtained by averaging over all atoms and sampled configurations.
We also calculate the static structure factor $S(q)$, assuming that the system is isotropic:

$$S(q) = \frac{1}{N} \left\langle \sum_{j=1}^{N} \sum_{k=1}^{N} e^{-iq|r_j - r_k|} \right\rangle \tag{A.7}$$

In our calculation, for each q, we choose 120 different directions and sum up the atomic distances directly. For efficiency reasons, we only sum up those distances, which are smaller than a cutoff-distance $r_c = 15$Å.

Experiments

The experimental data shown in this work is all taken from literature. As liquid Ti alloys are chemically highly reactive, containerless processing techniques, such as electrostatic or electromagnetic levitation is the method of choice in order to avoid pollution of the samples due to reactions with a substrate or a crucible. The data of density, molar volume and the structure factor are measured containerless. Density and molar volume shown here [25] are measured in electromagnetic levitation [26] using a shadow graph technique sometimes referred to as optical dilatometry [27]. In this technique, a shadow of the levitating droplet is projected from the side onto

the sensor of a camera. After recording a series of images, the sample volume is determined by integration of the time-averaged edge curve. Rotational symmetry regarding the vertical axis is assumed for the equilibrium shape. The uncertainty of this method is ±1.5% The experimental structure factor $S(q)$ is measured at ILL by the neutron scattering method [23] in electrostatic levitation [27, 28]. The viscosity data shown in this work is measured by Takeda [29] using the oscillating cup technique [27]. Very good care has been taken here in order to avoid crucible reactions in the latter case. In the oscillating cup technique, the melt is inside a cylindrical crucible which is suspended by a torsion wire and performed angular oscillations which decay with time due to the inner friction of the liquid. The decay time is measured by an optical arrangement and the viscosity is calculated from it by numerically solving the Navier-Stokes equations for that problem. The uncertainty of this method can vary up to ±20% .

Results

Densities

Figure A.1 shows the mass density and the corresponding molar volume as a function of the composition, at fixed temperature. Overall, the simulation results are in good agreement with experimental data, although a systematic overestimation of the density (and corresponding underestimation of the molar volume) is seen on the Ti-rich side. The error is on the order of 5% and becomes noticeable for $x_{\mathrm{Al}} \lesssim 0.5$. Still the simulation captures well the fact that in this regime, the molar volume remains almost independent of concentration, while for $x_{\mathrm{Al}} \gtrsim 0.5$ the molar volume increases with increasing Al content noticeably. Possible causes for the deviation on the Ti-rich side include limitations of the interatomic potential training set [19], which may underrepresent Ti-rich configurations. Alternatively, although the experimental values are supported by

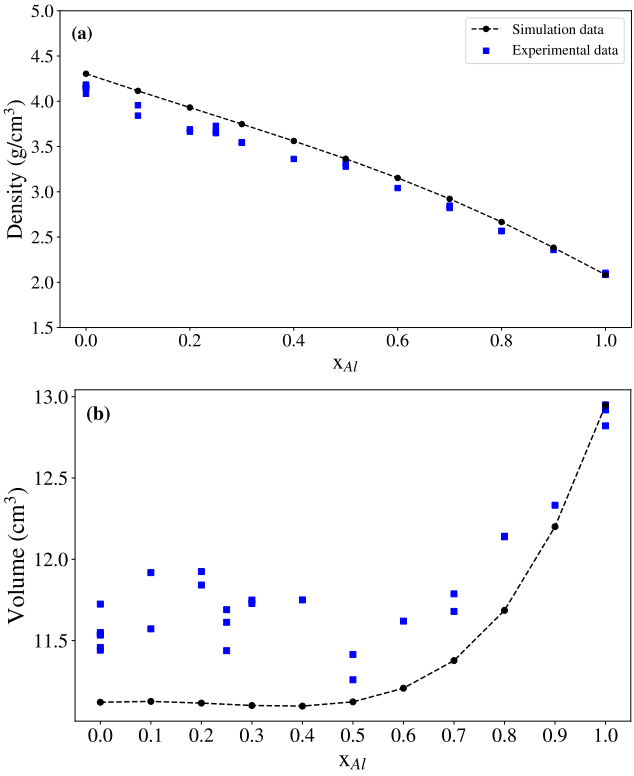

Figure A.1: Panel a) shows the mass density of the AlTi melts at $T = 1873\,\mathrm{K}$ as a function of Aluminium concentration. Black circle symbols joined by dotted lines are simulation data, blue squares represent experimental data from Ref. [30]. Panel b) shows the corresponding molar volume.

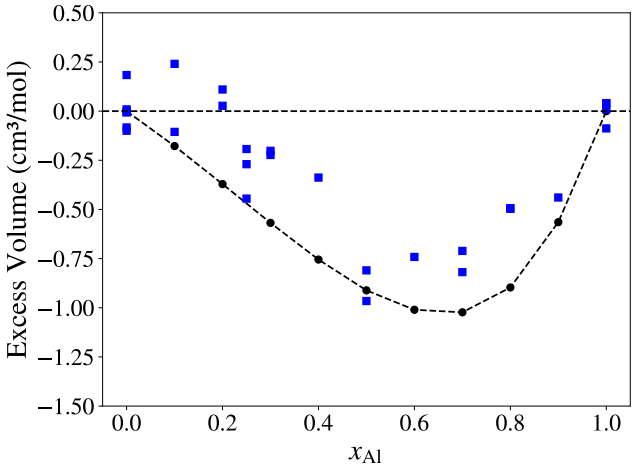

Figure A.2: Excess volume as a function of Al concentration at fixed temperature $T = 1873\,\mathrm{K}$. Circle symbols joined by dashed lines represent the simulation data, squares the experimental data from Ref. [30].

multiple literature sources [25, 31], a systematic experimental error cannot be fully ruled out.

A convenient measure to quantify non-ideal mixing of the two components of the melt is the excess volume, defined as

$$V_{\mathrm{excess}} = V - (x_{\mathrm{Al}} V_{\mathrm{Al}} + x_{\mathrm{Ti}} V_{\mathrm{Ti}}) \ , \tag{A.8}$$

where V is the volume of the mixture, and V_{Al} and V_{Ti}, respectively, are the volumes of the pure systems. By this, the excess volume measures the derivation from the ideal-mixing behavior.

Figure A.2 compares the simulation results with available experimental data. Due to an unexpected change of sign in the experimental data at low Al-concentrations, we can estimate the experimental error to be in the order of 0.3 $\mathrm{cm}^3/\mathrm{mol}$.

Within the estimated experimental uncertainty, the simulation reproduces the general trend observed in experiments. A negative

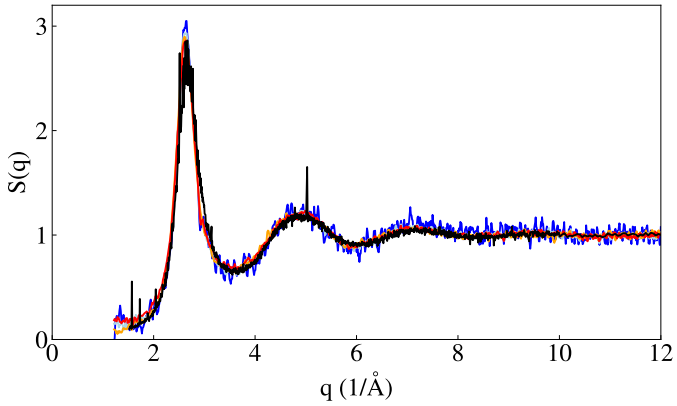

Figure A.3: Static structure factor for pure Aluminium. Blue: 1745K, lightblue: 1845K, orange: 1900K, red: 1965K, black: simulation at 1950K. Experimental data taken from [23]

excess volume is found, most pronounced at a concentration of $x_{\mathrm{Al}} \approx 0.6 \pm 0.1$ in both experiment and simulation.

Static structure factor

The MD-simulation allows to connect the composition dependence of the transport coefficients and thermophysical properties to the changes in microscopic structure. Figure A.3 shows the static structure factor for pure Ti at different temperatures obtained from simulations and experiments. Overall, the agreement between simulations and experiment is very accurate. One can observe that the peak positions are recovered by the simulations very well. Nevertheless, derivations in the height of the first peak can be found. A possible explanation for this behavior could be a shifted temperature scale in the simulations, which still has to be investigated.
Similarly, we can compare the inverse coordination number, obtained from simulations, with the experimental volume in figure A.4. Also there, we see a nice agreement between simulations and

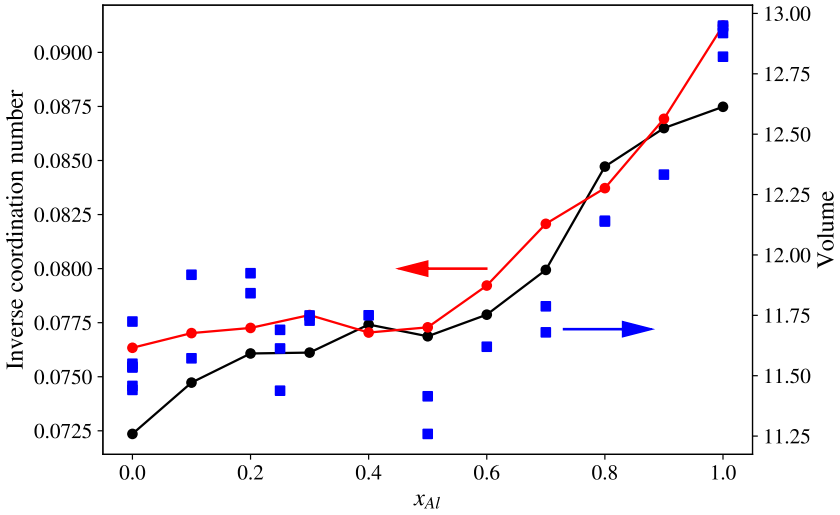

Figure A.4: Inverse coordination number from simulations (red and black), and experimental volume (blue)

experiment. Also, the partial radial distribution functions $g_{\alpha\beta}(r)$ are natural quantities to characterize this structure. Figure A.5 shows the evolution of this quantity for a constant temperature, and different concentrations. Interpreting the peak positions, one can conclude that there occurs some compression in the second-neighbor Ti-shells, when the Al-concentration increases. A comparison of the functions for AlAl and TiTi shows that the effective radii of the atoms are rather close. This could also explain why there is not a lot of structural change.

A common model for mixing effects in metallic melts is that of hard spheres of different sizes, where each atomic species is assigned an effective size. One way of estimating this size is via the position of the first peak in the pair distribution functions. We show the composition dependence of these quantities in Fig. A.6. Note that for the hard-sphere model, the peak positions would be solely given by the sizes of the spheres, and be independent of composition. Instead, we

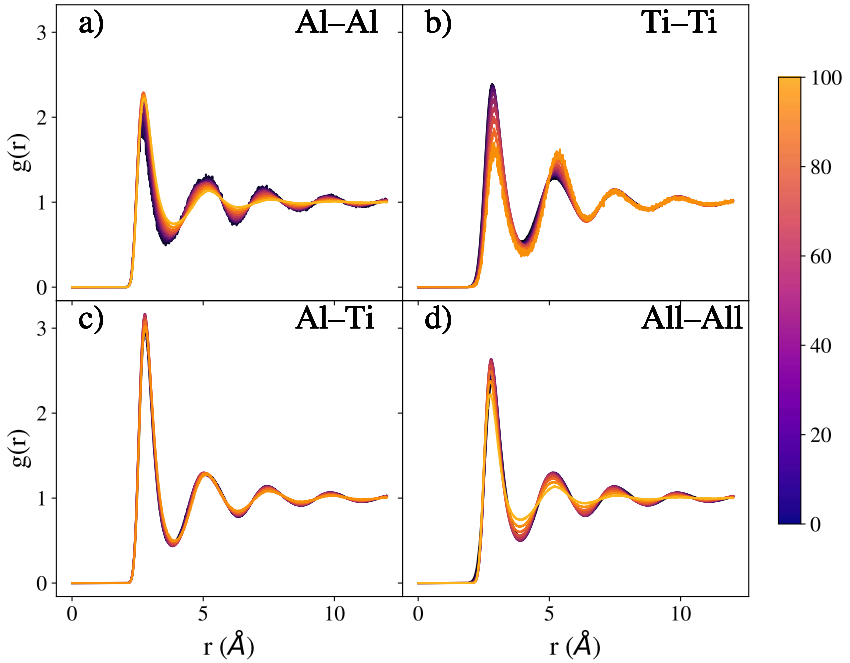

Figure A.5: Partial and total radial distribution functions $g(r)$ at fixed temperature $T = 1873$. Color codes the Al concentration from dark ($x_{\mathrm{Al}} = 0\%$) to bright ($x_{\mathrm{Al}} = 100\%$).

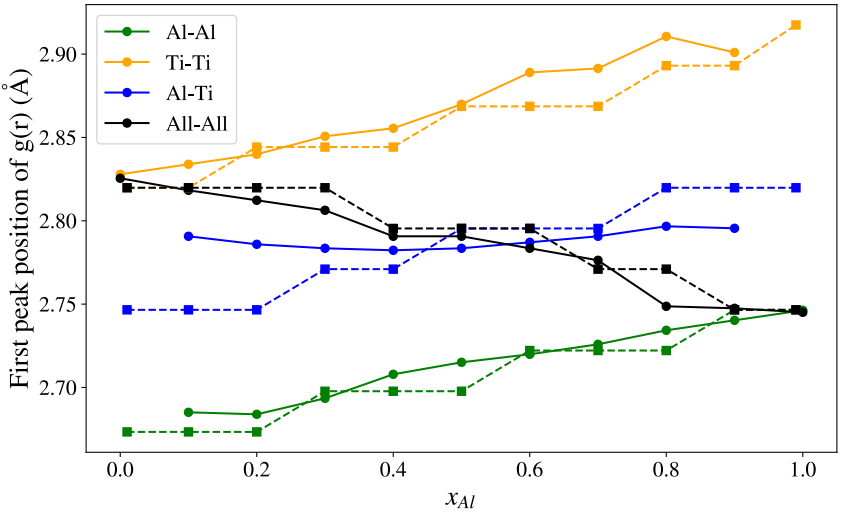

Figure A.6: Solid line: First-peak position of pair correlation function against concentration with 10000 particles at 1873K. Dashed line: First-peak position from Soft-sphere model /HNC-closure.

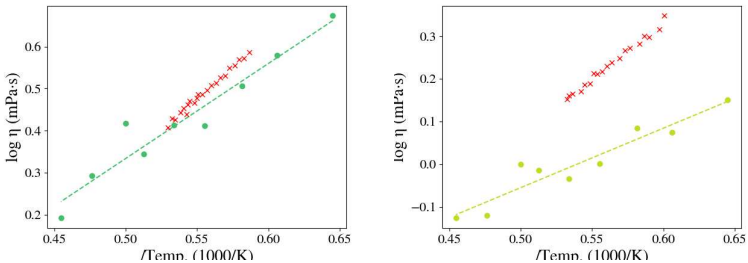

(a) $x_{Al} = 70\%$ (b) $x_{Al} = 90\%$

Figure A.7: Temperature dependence of the viscosity for different concentrations. Red symbols correspond to experimental data points. We show the concentration, where we got the best agreement between simulations and experiments (70%), and the one with the worst agreement (90%).

observe a monotonous increase of both the AlAl and the TiTi peak positions with increasing Al concentration. A similar trend has been seen in AlAu and was interpreted as a local compression. For the AlTi melt studied here, the compositional changes in microstructure are in fact well explained by a simple soft sphere model, the so-called HNC-closure, first established by Verlet and Hansen in the 1970s [32, 33]. This approximation generally describes fluids with soft or long-range interactions, such as ionic or metallic liquids, and serves as a key tool for predicting structural and thermodynamic properties from microscopic potentials. In figure A.6, one can see that with this model, we get a precise agreement between simulations and theoretical prediction.

Viscosity

Figure A.7 shows the temperature dependent viscosity for selected compositions where experimental data is available. In the temper-

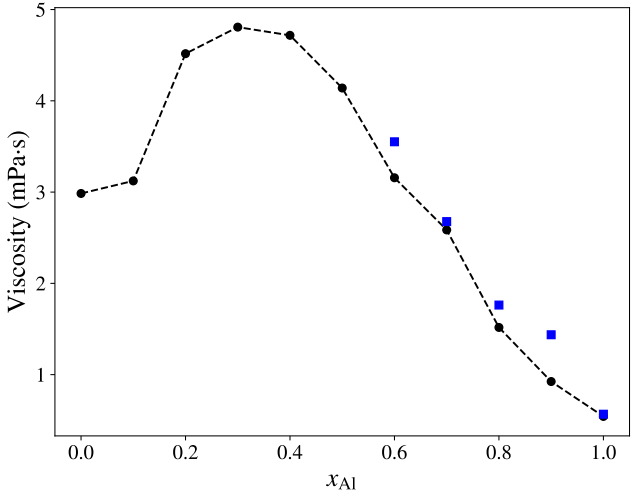

Figure A.8: Viscosity of the Al-Ti melts as a function of Al concentration, for fixed temperature $T = 1873\,\mathrm{K}$. Black symbols connected by dashed lines are the simulation results, blue squares represent experimental data.

ature range considered in this work, the viscosity closely follows an Arrhenius law, as corresponding fits (dashed lines in the figure) show. With the exception of pure Al, we observe that the NEP potential predicts slightly lower activation energies and slightly lower overall viscosities than those measured in experiment. The largest discrepancy occurs at $x_{\mathrm{Al}} = 0.9$, where the experimental viscosity is significantly larger than in the simulation.

The reason for this strong deviation is unclear. By comparing the data for $x_{\mathrm{Al}} = 0.8$ and $x_{\mathrm{Al}} = 1.0$, we note that in these cases, the agreement between simulation and experiment is much better.

To investigate more clearly the concentration dependence of the viscosity, we show results at fixed temperature in Fig. A.8. The viscosity displays are clear maximum at intermediate composition; this is an effect quite robustly found in various binary alloy systems such

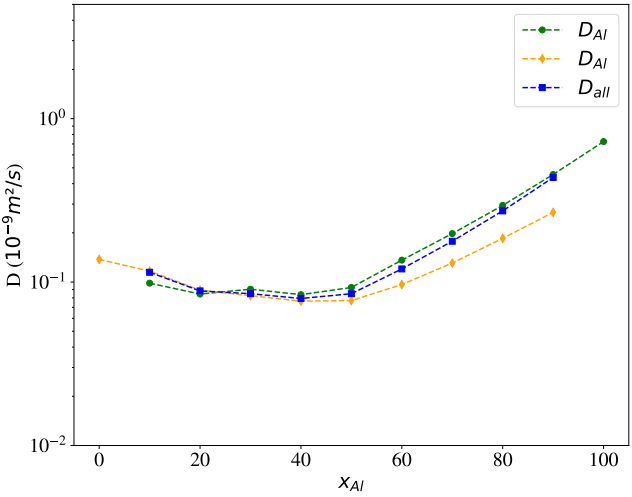

Figure A.9: Concentration-dependent diffusion coefficients of the Al-Ti melt at $T = 1720\,\mathrm{K}$.

as HgNa, PbTi [34], and AlNi [35].

In the case of AlTi, the NEP simulation predicts a maximum at around $x_{\mathrm{Al}} \approx 0.3$ for the chosen temperature, i.e., at somewhat lower Al concentrations as the one where the cross-over in the atomic volume and the minimum of the excess volume are seen. The available experimental data on the Al-rich side agree well with our simulation results.

Diffusion coefficient

Figure A.9 shows the diffusion coefficient as a function of concentration. The overall diffusion coefficient, L, is defined as the weighted average

$$L = x_{\mathrm{Al}}\, D_{\mathrm{Ti}} + x_{\mathrm{Ti}}\, D_{\mathrm{Al}}, \tag{A.9}$$

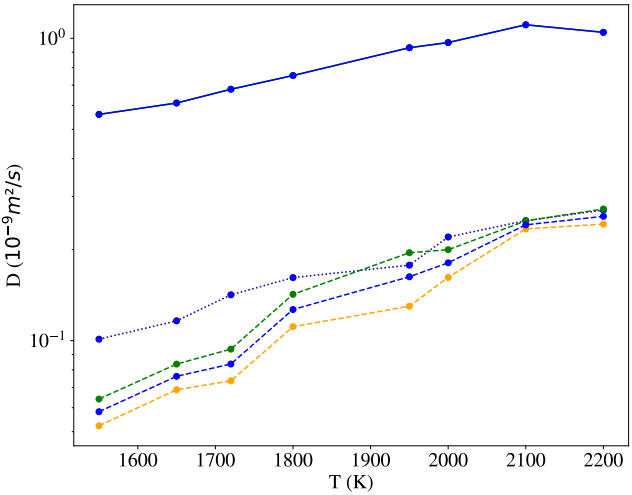

Figure A.10: Diffusion coefficients as a function of temperature. Green lines represent D_{Al}, orange lines represent D_{Ti}, and blue lines represent D_{All}. Solid lines correspond to $x_{\mathrm{Al}} = 100\%$, dashed lines to $x_{\mathrm{Al}} = 50\%$, and dotted lines to $x_{\mathrm{Al}} = 0\%$.

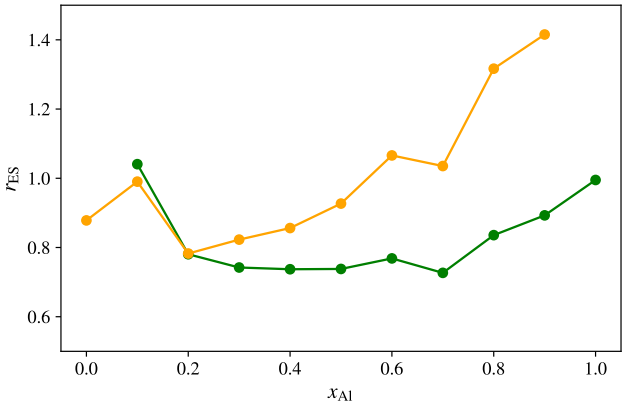

Figure A.11: Concentration-dependent hydrodynamic radius r_{SE} from the Stokes–Einstein (SE) relation of the Al-Ti melt at $T = 1873\,\mathrm{K}$.

where x is the Ti atomic fraction. This quantity provides a reference for the average mobility of the liquid mixture. Since diffusivity and inverse viscosity are both measures of the fluidity of a system, from the maximum in the viscosity one expects the diffusion coefficients to show a mixing-induced minimum. This is indeed seen in Fig. A.9. The minima in the self-diffusion coefficients occur at slightly different concentrations.

The temperature dependence of the diffusion coefficient can be seen in figure A.10. As expected, the diffusion becomes larger at larger temperatures. To further understand the relation between atomic diffusion and viscous flow, we estimated the effective hydrodynamic radius r_{SE} from the Stokes–Einstein (SE) relation, rewritten here with r_{SE} as the dependent variable:

$$r_{SE} = \frac{k_B T}{6\pi D_i \eta} \tag{A.10}$$

where D_i is the self-diffusion coefficient of each species and η is the dynamic viscosity of the liquid at $T = 1873$ K. The resulting values

are shown in Fig. A.11 as a function of composition. It is evident that r_{SE} varies considerably with composition, despite the fact that the first peak position of the radial distribution function, $r_{G(r)}/2$, remains nearly constant.

Conclusion

In conclusion, we investigated the thermophysical properties of Al-Ti-melts and by this validated the NEP89 potential.
In our study of static properties, we observed very good agreement between simulation-derived densities and experimentally measured densities. We found that in the Ti-rich case, deviations between these methods are much more pronounced. Future work will focus on a detailed investigation of this phenomenon. Specifically, one intriguing research question would be how the density and volume are affected by contamination, which is omnipresent in experiments. Such contaminations could in principle be modeled by the same potential as the one we used in these simulations.

Moreover, in the comparison of structural properties, such as the static structure factor and pair-correlation function, we observed very good agreement between simulations and experiments. This indicates, that the structure of the real material is well reproduced by the simulations. By tracking the first-peak-position of the pair-correlation function, we found that the peak-position is changing, when changing the concentration. This indicates that the particles are not behaving like hard spheres. We showed that they behave like soft spheres by comparing our results to a HNC-closure calculation. From this, we can conclude that also chemical reactions play a key role in the interaction.

Furthermore, the investigation of dynamical properties revealed very good agreement between simulations and experiments. As the potential is mainly trained on solid properties and also the applications of this potential are mainly related to properties of a solid material,

this is not trivial. When for example investigating the concentration dependence of the viscosity, it turns out that experiment and simulation are in very well agreement. Nevertheless, we observe that the temperature dependence of viscosity does not agree well across all compositions. The phenomenon that machine-learning potentials do not recover the temperature dependence of the material exactly, is a phenomenon which also occurred in other studies [36]; and future research will include the investigation of this temperature dependence, especially in the region of the glass-transition temperature.

A thin-film analysis of viscoelastic shear-thinning fluids using a droplet geometry

We study the thin-film behaviour of shear-thinning viscoelastic fluids. As an analytical approach, we make use of the lubrication approximation, i.e. we approximate the governing equations of motion such that they describe the behaviour of a thin film.
It turns out that we have to make use of a two-parameter scaling law in order to describe the droplet's behaviour on all timescales correctly.
We also present simulations, which describe the spreading of shear-thinning viscoelastic droplets and find a very accurate agreement between simulations and analytical prediction.

Introduction

Viscoelastic fluids, owing to their unique rheological properties, find extensive use across various industrial applications, spanning inkjet printing [37], spray coatings [38], diesel injections [39], additive manufacturing [40], pesticide deposition [41], and surface cooling [42], among others. Understanding the intricacies of wetting and spreading phenomena within these applications remains paramount for optimizing performance and efficiency.

On the theoretical front, the spreading behavior is often elucidated through thin-film equations, which rely on the lubrication approximation derived from hydrodynamic equations of motion, first done by Reynolds in 1886 [43]. This theory was then extended to both different flow geometries and generalized Newtonian fluids (see for example [44–48]). Over recent years, significant progress has been made in formulating thin-film equations tailored to both viscoelastic and shear-thinning fluids individually [49–55]. However, an unaddressed gap persists in deriving thin-film equations capable of accurately capturing the behavior of fluids exhibiting a combination of these rheological properties.

This paper endeavors to bridge this gap by introducing a novel approach. Our investigation reveals the necessity of employing a two-parameter scaling law to appropriately describe the spreading behavior across all relevant timescales, a novel method within the domain of lubrication approximation.

The focus of our study revolves around the behavior of a viscoelastic droplet spreading on a pre-wetted surface, with emphasis placed on measuring the droplet's height along the z-axis. In order to simplify the problem, we confine our analytical analysis to the 2-dimensional scenario.

The structure of the paper is as follows: We commence with the derivation of thin-film equations tailored to viscoelastic shear-thinning droplets. Subsequently, leveraging simulations, we delve into an in-depth exploration of the droplet's spreading dynamics.

Finally, we culminate our investigation with a comprehensive comparison between the simulation results and a Finite-Element analysis of the derived thin-film equation, thereby providing a rigorous validation of our proposed framework.

A thin-film equation for the generalized Maxwell-model

Governing equations

Here, we introduce the hydrodynamic conservation laws for viscoelastic media. In this part, we reduce ourselves to the 2-dimensional case due to cylindrical symmetry of the droplets.
We assume having an incompressible liquid with mass density ρ. Hence, the law of mass conservation can be written as:

$$\nabla \cdot \mathbf{v} = 0 \tag{A.11}$$

Here, $\mathbf{v} = (v_x, v_z)$ is the velocity field.
Neglecting external forces, the equation of momentum conservation is expressed by

$$\rho \frac{d\mathbf{v}}{dt} = -\nabla p + \nabla \cdot \sigma \tag{A.12}$$

with the pressure p and the deviatoric stress σ. In this equation, the operator $\frac{d}{dt}$ represents the material derivative, defined as $\frac{d}{dt}A = \partial_t A + (\mathbf{v} \cdot \nabla)A$.
The deviatoric stress is related to the shear rate $\dot{\gamma}$ (defined as $\dot{\gamma}_{ij} = \partial_i v_j + \partial_j v_i$ for $i, j \in (x, z)$) in the following way:

$$\left(\frac{1}{\tau_1} + \partial_t + \frac{|\dot{\gamma}|}{\gamma_c}\right)\sigma = \eta\left(\frac{1}{\tau_1} + \frac{G_\infty}{\eta} + \partial_t + \frac{|\dot{\gamma}|}{\gamma_c}\right)\dot{\gamma} \tag{A.13}$$

Here, τ_1 is the relaxation time, $\dot{\gamma}$ is the $\mathcal{L}_2$-norm of the shear-rate tensor, γ_c is a (nondimensional) constant, η is the viscosity and

G_∞ is the shear modulus. Note that this equation is similar to the one discussed in [50]. The principal difference is that we included a shear-rate dependent relaxation time $\tau^{-1} \to \tau^{-1} + |\dot{\gamma}|/\gamma_c$ as described by [56]. Physically, with this modification, we include the phenomenon of shear-thinning.
As boundary conditions, we make use of no-slip boundaries at the solid-liquid interface ($v_x|_{z=0} = v_y|_{z=0} = 0$) and the Laplace pressure at the gas-liquid interface:

$$(\sigma - p1) \cdot \mathbf{n} = 2\hat{\sigma}\kappa \cdot \mathbf{n} \tag{A.14}$$

Here, $\hat{\sigma}$ is the surface tension, $\mathbf{n}$ is the normal vector pointing out of the fluid and κ is the curvature of the interface.
As the fluid is incompressible, the height-function can be coupled to the velocity field:

$$\partial_t h = -\nabla_\parallel \cdot \int_0^h dz v_x \tag{A.15}$$

This is the so-called kinematic boundary condition.

Scaling laws

All quantities in x-direction are scaled with a length scale L, the quantities in z-direction are scaled with the length scale H. Their ratio $H/L = \epsilon$ is assumed to be small due to the fact that we work with a thin film.
In contrast to the existing lubrication approximations, we make use of two timescales, similar to methods described in [57, 58]: Physically, this means that we observe different processes at small and at large times.
The small timescale is called T_-, the large timescale is called T_+. We assume them to be related via a small parameter δ: $\delta \cdot T_+ = T_-$. As we assume having large relaxation times, the relaxation time is scaled with T_+, the other quantities are scaled with T_-. In fact, the timescale T_- can be understood as an 'inner droplet-time'.

Velocities in x-direction are scaled with L/T_-, velocities in z-direction are scaled with H/T_-. Similar to [50], the pressure is scaled with $P = \eta/T_- \cdot \epsilon^2$ and the surface tension is scaled with $L \cdot \eta/T_- \cdot \epsilon^3$. The shear modulus G_∞ is scaled similar to the relaxation time, with η/T_+.
The stress-tensor is scaled as

$$\begin{pmatrix} \sigma_{xx} & \sigma_{xz} \\ \sigma_{zx} & \sigma_{zz} \end{pmatrix} = \frac{\eta}{T_-} \cdot \begin{pmatrix} \sigma^*_{xx} & \sigma^*_{xz}/\epsilon \\ \sigma^*_{zx}/\epsilon & \sigma^*_{zz} \end{pmatrix}$$

Dimensionless equations

Note: Due to notation's brevity, until now, we write the non-dimensional quantities without the "*".
With the aid of the scaling laws derived in the previous section, we can formulate the governing equations in a non-dimensional form. The mass conservation is already non-dimensional.
The non-dimensional momentum equation is given by:

$$\begin{aligned} \epsilon^2 \cdot Re \cdot \frac{dv_x}{dt} &= \epsilon^2(\partial_x \sigma_{xx}) + \partial_z \sigma_{zx} - \partial_x p \\ \epsilon^4 \cdot Re \cdot \frac{dv_z}{dt} &= \epsilon^2(\partial_x \sigma_{xz} + \partial_z \sigma_{zz}) - \partial_z p \end{aligned} \tag{A.16}$$

Here, the Reynolds-number is defined $Re = \rho L^2/T\eta$.
The norm of the shear-rate can be formulated in the following non-dimensional, explicit way, using that this tensor is symmetric by definition:

$$|\dot{\gamma}| = \frac{\sqrt{(2\partial_x v_x)^2 + (2\partial_z v_z)^2 + 2 \cdot (\epsilon \partial_x v_z + \frac{\partial_z v_x}{\epsilon})^2}}{T_-} \tag{A.17}$$

Using that the time-derivative appears on both timescales ($\partial_t \to \frac{1}{T_+}\partial_t + \frac{1}{T_-}\partial_t$), for the diagonal components of the constitutive law,

we get the following equations:

$$\left(\frac{1}{T_+\tau_1}+\frac{1}{T_+}\partial_t+\frac{1}{T_-}\partial_t+\frac{|\dot\gamma|}{\gamma_c}\right)\sigma_{xx} = 2\cdot\left(\frac{1}{T_+}\Big[\frac{1}{\tau_1}+1\Big]+\frac{1}{T_+}\partial_t+\frac{1}{T_-}\partial_t+\frac{|\dot\gamma|}{\gamma_c}\right)\cdot\partial_x v_x \tag{A.18a}$$

$$\left(\frac{1}{T_+\tau_1}+\frac{1}{T_+}\partial_t+\frac{1}{T_-}\partial_t+\frac{|\dot\gamma|}{\gamma_c}\right)\sigma_{zz} = 2\cdot\left(\frac{1}{T_+}\Big[\frac{1}{\tau_1}+1\Big]+\frac{1}{T_+}\partial_t+\frac{1}{T_-}\partial_t+\frac{|\dot\gamma|}{\gamma_c}\right)\cdot\partial_z v_z \tag{A.18b}$$

The off-diagonal expression is given by

$$\left(\frac{1}{T_+\tau_1}+\frac{1}{T_+}\partial_t+\frac{1}{T_-}\partial_t+\frac{|\dot\gamma|}{\gamma_c}\right)\frac{1}{\epsilon}\sigma_{xz} = 2\cdot\left(\frac{1}{T_+}\Big[\frac{1}{\tau_1}+1\Big]+\frac{1}{T_+}\partial_t+\frac{1}{T_-}\partial_t+\frac{|\dot\gamma|}{\gamma_c}\right)\cdot(\epsilon\partial_x v_z+\frac{1}{\epsilon}\partial_z v_x) \tag{A.19}$$

From the Laplace-pressure, we get two equations:
One is obtained by multiplying the condition with the normal vector, the other with the tangential vector from left:

$$\frac{\sigma_{zz}-2\sigma_{xz}\partial_x h}{1+\epsilon^2(\partial_x h)^2}+\epsilon^2\frac{\sigma_{xx}\cdot(\partial_x h)^2}{1+\epsilon^2(\partial_x h)^2}-\frac{p}{\epsilon^2} = \frac{1}{\epsilon^2}\frac{\partial_x^2 h}{[1+\epsilon^2(\partial_x h)^2]^{3/2}} \tag{A.20}$$

$$0=[1-\epsilon^2(\partial_x h)^2]\partial_x h\cdot\sigma_{xz}+\epsilon^2(\partial_x h)^2[\sigma_{zz}-\sigma_{xx}] \tag{A.21}$$

Here, the normal vector $\mathbf{n}$ and the tangential vector $\mathbf{t}$ are defined as

$$\mathbf{n}=\frac{1}{\sqrt{1+(\partial_x)^2}}\begin{pmatrix}-\partial_x h\\1\end{pmatrix} \tag{A.22}$$

$$\mathbf{t}=\frac{1}{\sqrt{(\partial_x h)+(\partial_x h)^2}}\begin{pmatrix}\partial_x h\\(\partial_x h)^2\end{pmatrix}$$

The curvature of the interface is expressed as:

$$\kappa = \frac{\partial_x^2 h}{(1 + (\partial_x h)^2)^{3/2}} \tag{A.23}$$

The thin-film equation

In this step, we use the non-dimensional equations from section 6 and neglect all terms which are of order ϵ and higher.
With this, the momentum equation reduces to

$$\begin{aligned} \partial_z \sigma_{xz} &= \partial_x p + \mathcal{O}(\epsilon) \\ 0 &= \partial_z p + \mathcal{O}(\epsilon) \end{aligned} \tag{A.24}$$

From the Laplace pressure, we get the following relation:

$$p|_{z=h} = -\partial_x^2 h \tag{A.25}$$

as well as

$$0 = \partial_x h \cdot \sigma_{xz} \tag{A.26}$$

As $\partial_x h \neq 0$, from the last equation, it follows that $\sigma_{xz}|_{z=h} = 0$. If we integrate the momentum equation with respect to z, we get:

$$\sigma_{xz} = (z - h) \cdot \partial_x p \tag{A.27}$$

A Taylor-expansion around $\epsilon = 0$ gives the following expression for the norm of the shear-rate:

$$|\dot{\gamma}| = \frac{\sqrt{2}}{T_-} \cdot \frac{1}{\epsilon} |\partial_z v_x| + \mathcal{O}(1) \tag{A.28}$$

The off-diagonal component of the stress tensor can then be written in the following way:

$$\begin{aligned} &\Big(\frac{1}{T_+\tau_1} + \frac{1}{T_+}\partial_t + \frac{1}{\delta T_+}\partial_t + \frac{\sqrt{2}|\partial_z v_x|}{\epsilon\delta\gamma_c \cdot T_+}\Big)\frac{1}{\epsilon}\sigma_{xz} \\ &= 2\Big(\frac{1}{T_+}\Big[\frac{1}{\tau_1} + 1\Big] + \frac{1}{T_+}\partial_t + \frac{1}{\delta T_+}\partial_t + \frac{\sqrt{2}|\partial_z v_x|}{\epsilon\delta\gamma_c \cdot T_+}\Big) \cdot \\ &\qquad (\epsilon\partial_x v_z + \frac{1}{\epsilon}\partial_z v_x) \end{aligned} \tag{A.29}$$

Multiplying by ϵ and neglecting all terms which are of order ϵ^2 gives the following equation:

$$\begin{aligned}\Big(\frac{1}{T_+\tau_1}+\frac{1}{T_+}\partial_t+\frac{1}{\delta T_+}\partial_t+\frac{\sqrt{2}\cdot|\partial_z v_x|}{\epsilon\delta\gamma_c\cdot T_+}\Big)\sigma_{xz}\\ =2\cdot\Big(\frac{1}{T_+}\Big[\frac{1}{\tau_1}+1\Big]+\frac{1}{T_+}\partial_t+\frac{1}{\delta T_+}\partial_t+\\ \frac{\sqrt{2}}{\epsilon\delta\gamma_c\cdot T_+}\cdot|\partial_z v_x|\Big)\cdot\partial_z v_x\end{aligned}\tag{A.30}$$

Now, we balance all terms which are of the same order of δ individually:

$$\begin{aligned}\left(\frac{1}{\delta\cdot T_+}\partial_t+\frac{\sqrt{2}}{\epsilon\delta\gamma_c\cdot T_+}\cdot|\partial_z v_x|\right)\sigma_{xz}\\ =2\cdot\left(\frac{1}{\delta\cdot T_+}\partial_t+\frac{\sqrt{2}}{\epsilon\delta\gamma_c\cdot T_+}\cdot|\partial_z v_x|\right)\partial_z v_x\end{aligned}\tag{A.31a}$$

$$\begin{aligned}\left(\frac{1}{T_+\cdot\tau_1}+\frac{1}{T_+}\partial_t\right)\sigma_{xz}\\ =2\cdot\left(\frac{1}{T_+}\Big[\frac{1}{\tau_1}+1\Big]+\frac{1}{T_+}\partial_t\right)\partial_z v_x\end{aligned}\tag{A.31b}$$

In the second step, we take the limit $\epsilon\to 0$. Then our equations can be written as:

$$\left(\frac{\sqrt{2}|\partial_z v_x|}{\gamma_c\cdot T_+}\right)\sigma_{xz}=2\cdot\left(\frac{\sqrt{2}}{\gamma_c T_+}\cdot|\partial_z v_x|\right)\partial_z v_x\tag{A.32a}$$

$$\begin{aligned}\left(\frac{1}{T_+\tau_1}+\frac{1}{T_+}\partial_t\right)\sigma_{xz}\\ =2\cdot\left(\frac{1}{T_+}\Big[\frac{1}{\tau_1}+1\Big]+\frac{1}{T_+}\partial_t\right)\partial_z v_x\end{aligned}\tag{A.32b}$$

Finally, we can solve both equations. The first equation obviously represents the small-time regime. It turns out that in this regime, we find two distinct solutions: $|\partial_z v_x|=0$ and $2\cdot\partial_z v_x=\sigma_{xz}$.
The thin-film equation which corresponds to the first solution is

obviously given by $\partial_t h = 0$. The second one corresponds to a Newtonian thin-film equation.
The second equation represents the large-time regime. There, we see that this is a known problem, solved by [50]. This describes the behaviour of a thin-film of a Jeffrey's fluid without shear-thinning.
As we assume having a smooth transition from the small to the large time regime, we choose the solution $\partial_t h = 0$ as a solution for the small-time regime.
Finally, we define a transition time τ_{tran}, which describes the time, in which the behavior of the thin-film changes. From the argumentation above (especially formula A.31a), it follows that this time the following conditions should be fulfilled: $\epsilon\delta\gamma_c = \mathcal{O}(1)$ and $\delta = \mathcal{O}(\tau_1)$. It directly follows that $\tau_{trans} \propto \gamma_c^{-1}$ and $\tau_{trans} \propto \tau_1$.
As a consistency check, we note that for $\gamma_c \to \infty$ the transition time becomes 0. This corresponds to our expectation because this means that the 'no-shear-thinning'-behavior is starting at the beginning.
In the case $\gamma_c \to 0$, the transition time becomes infinite, which means that we have a finite height in the whole process. This corresponds to the research of Jalaal for the Bingham fluid [59].
Furthermore, for an infinite relaxation time, the transition time also becomes infinite. This also corresponds to the case of the yield stress [59].

Numerical Analysis

Simulations

Here, we present the simulations, carried out with the open-source free-software language `BASILISK C` [60, 61].
With this, we make use of an adaptive mesh refinement based on wavelet estimated discretization errors. `BASILISK C` makes use of a volume of fluid technique to track the interface. It makes use of a color function f ($f = 1$ in the liquid and $f = 0$ in the gas), which

satisfies the scalar-advection equation. One solves the governing equations using a one-fluid approximation [62, 63].

All plots, if not mentioned else, present the maximal height of the droplet in time. A more in-depth description of the individual parameters can be found in the appendix. In our simulations, we investigated the spreading of droplets which are described by an Oldroyd-B fluid, first introduced by Oldroyd in 1950 [64]. More specifically, we investigated both the case with shear-thinning and without shear-thinning.
As an initial condition, we made use of a function of Gaussian type:

$$h(x) = \exp\left(-x^2\right) + h_\infty \tag{A.33}$$

The governing equations of our simulations were given by the well-known mass-conservation equation for incompressible fluids

$$\nabla \cdot \mathbf{v} = 0 \tag{A.34}$$

and the momentum conservation equation

$$\rho \cdot \frac{d}{dt}\mathbf{v} = -\nabla p + \nabla \cdot \sigma + F_{ext} \tag{A.35}$$

This tensor is defined by a constitutive relation.
One assumes the stress to consist of two different parts, the Newtonian part and the polymeric part.
The Newtonian part can be described by $\sigma = \eta_N \cdot \dot{\gamma}$.
To describe the polymeric part, we use Maxwell's idea, that the fluid behaves like a solid on small timescales and on large timescales, it starts to flow. Hence, the polymeric part can be described by

$$\begin{aligned} &\frac{1}{\tau_{eq}} \cdot \sigma + \overset{\triangledown}{\sigma} = G_\infty \cdot \dot{\gamma} \\ &\text{or } \sigma + \tau_{eq}\overset{\triangledown}{\sigma} = \eta_P \cdot \dot{\gamma} \end{aligned} \tag{A.36}$$

In this definition, one can see that the relation between the shear-modulus and the polymeric viscosity is given by

$$\tau_{eq} \cdot G_\infty = \eta_P \tag{A.37}$$

The sign $\triangledown$ indicates the upper-convected time-derivative, defined as

$$\overset{\triangledown}{A} = \frac{d}{dt}A - (\nabla \mathbf{v})^T \cdot A + A \cdot (\nabla \mathbf{v}) \tag{A.38}$$

The total stress is then given by the sum of the Newtonian part and the polymeric part. Hence, the full constitutive law can be written in the following form:

$$\begin{aligned} \left(\frac{1}{\tau_{eq}} + \overset{\triangledown}{?}\right)\sigma &= \left(\frac{1}{\tau_{eq}} + \overset{\triangledown}{?}\right)(\sigma_N + \sigma_P) \\ &= \eta_N \left(\frac{1}{\tau_{eq}} + \overset{\triangledown}{?}\right)\dot{\gamma} + G_\infty \dot{\gamma} \\ \left(\frac{\eta_N}{\tau_{eq}} + G_\infty + \overset{\triangledown}{?}\right)\dot{\gamma} &= \eta_N \left(\frac{1}{\beta\tau_{eq}} + \overset{\triangledown}{?}\right)\dot{\gamma} \end{aligned} \tag{A.39}$$

To include shear-thinning, we make use of a shear-rate dependent relaxation time, following [56], such that

$$\frac{1}{\tau} \to \frac{1}{\tau} + \frac{|\dot{\gamma}|}{\gamma_c} \tag{A.40}$$

Figure A.13 shows a comparison of the height development for different relaxation times. As shown in the figure, for large times we recover Tanner's law, a law which predicts the scaling of the height for a Newtonian fluid ($h \propto t^{-1/10}$ in 2 dimensions) [65–67]. Furthermore, this plot shows that for large relaxation times oscillations occur. They can be explained by the elastic nature of the viscoelastic fluid at small times.
Figure A.14 shows how the maximal height of the droplet is changing for different values of γ_c, i.e. of different strengths of shear-thinning. These plots can be connected to our analytical approach, as we can see that the droplets' height development is a plateau. For a small relaxation time, i.e. in figure A.14, one can even observe the transition time, which is inverse proportional to the parameter γ_c.
Finally, we made a scaling analysis of the 'finite height', which in

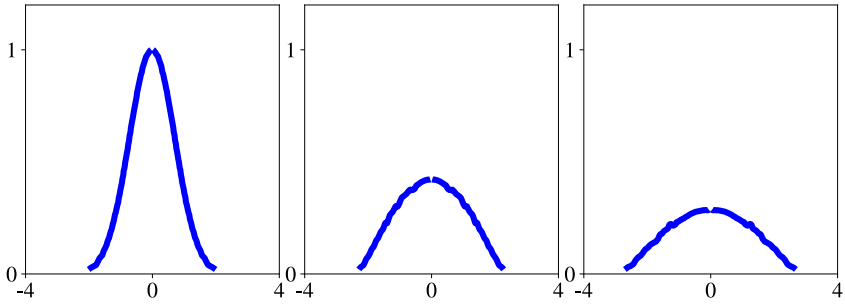

Figure A.12: Shape of the droplet at three different points in time: The left picture corresponds to $t = 0.0$, the center picture corresponds to $t = 2.4$ and the right picture corresponds to $t = 24$. The pictures correspond to the case of $\tau = 1$ and $\gamma_c = 1/10$.

our case means the height of the plateau: In figure A.15, one can see how the finite height scales with γ_c. As we assume the yield stress to be $G_\infty \cdot \gamma_c$, we can recover the scaling law of [59] in this plot. Similarly, we get the scaling law of the gravitation in figure A.16. Another free parameter of our simulations is the surface tension. In figure A.17, one can see the simulation results for different values of the surface tension, scaled with an effective relaxation time τ_{eff}. As shown in this figure, the only effect of the surface tension is the determination of a timescale. As shown in the inset, this effective relaxation time is inverse proportional to the surface tension.

Finite-Element-Analysis

In addition to the simulations, which solve the full Navier-Stokes equation numerically, we also solved the thin-film equation for the Jeffrey's model numerically. To do so, we used the open-source-package `fenics`.
A detailed description of these calculations can be found in the ap-

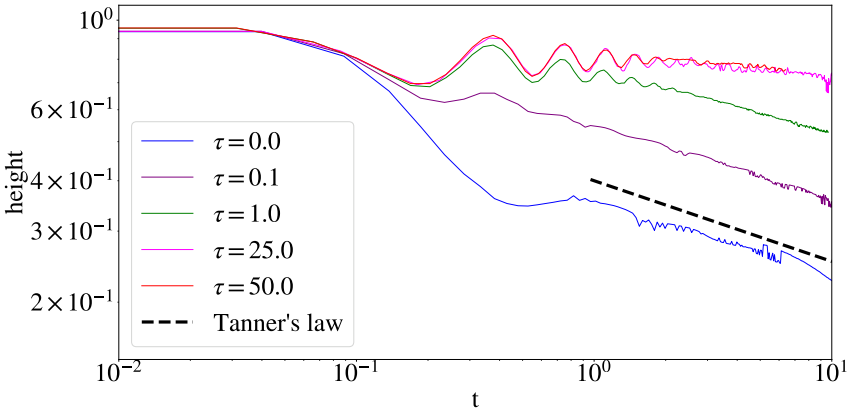

Figure A.13: Height evolution of the droplets for different relaxation times in the case without shear-thinning ($\gamma_c \to \infty$)

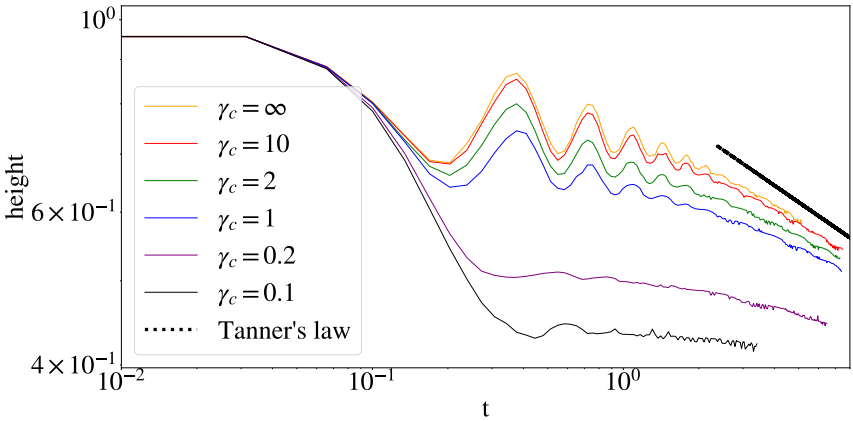

Figure A.14: Height evolution of droplets with different shear-thinning impact for a constant relaxation time of $\tau = 1$.

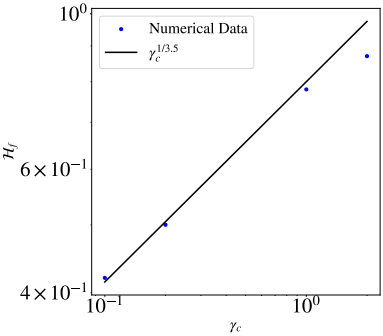

Figure A.15: Scaling of the final height with the yield stress ($\propto \gamma_c$). The numerical data corresponds to the case of $\tau = 50$ and different values of γ_c.

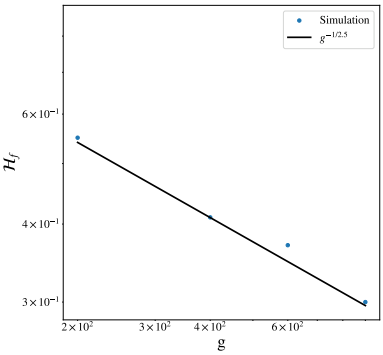

Figure A.16: Scaling of the final height in dependence of the gravitational force. The numerical data corresponds to the case of $\tau = 50$ with $\gamma_c = 0$.

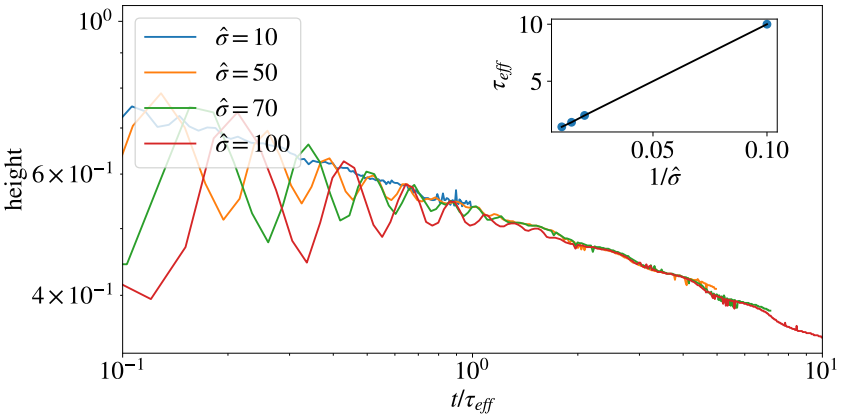

Figure A.17: Evolution of the droplet height for different surface tensions. The relaxation time is in all cases $\tau = 1$, and we used the case without shear-thinning. For each graph, the time is scaled with an effective relaxation time. The effective relaxation time is $10, 2, 1.4$ and 1 for the surface tensions $10, 50, 70, 100$. The relaxation times fulfill $\tau_{eff} \propto 1/\hat{\sigma}$, see inset

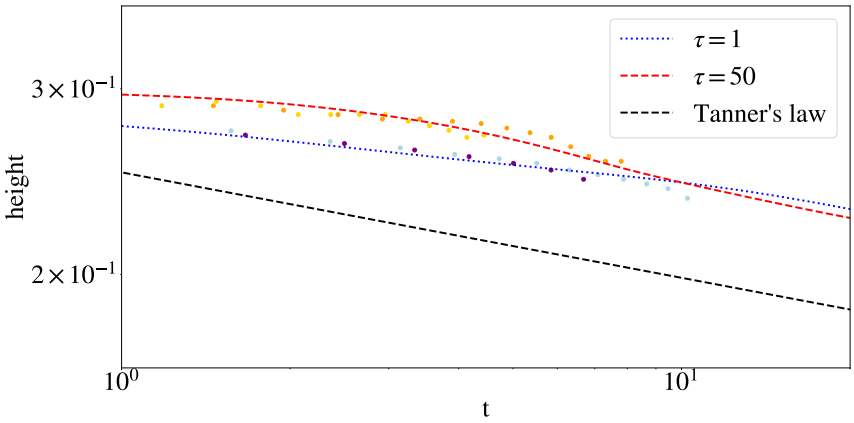

Figure A.18: Comparison of the numerical solution of the thin-film equation with the simulations. The golden and orange points correspond to simulations for $\tau = 50$, with $\hat{\sigma} = 50$ and $\hat{\sigma} = 100$. The blue and purple points correspond to simulations with $\tau = 1$, also for $\hat{\sigma} = 50$ and $\hat{\sigma} = 100$. One can observe a very well correspondence between the two methods. The simulation data is scaled as shown in figure A.17. Note that the corresponding simulations were done in 2 dimensions.

pendix.

Figure A.18 shows a comparison of the numerical results with the simulation results. There, the simulation results are scaled with an effective relaxation time, similar to figure A.17. The initial condition of these simulation was chosen such that the initial height is 0.3, similar to the numerical initial condition. Furthermore, the simulations were performed only in 2 dimension to have a proper comparison. Figure A.18 shows that there is an excellent agreement between numerical data from the thin-film equation and the simulations.

Summary and Outlook

In conclusion, our study presents a novel thin-film equation tailored specifically for viscoelastic shear-thinning droplets. Through rigorous testing against the spreading droplet geometry and subsequent validation via simulations, we have demonstrated the accuracy of our model.
Our findings underscore the complexity of viscoelastic fluid behavior, pointing out the inadequacy of a single-parameter approach in capturing the full spectrum of droplet dynamics across different timescales.

With our approach, we could identify three different regimes of the height evolution, related to the initial spreading, the yield-stress regime, and a final viscous-flow regime.

We discussed the different time scales associated to these regimes and their crossovers.

Moreover, our study demonstrates a remarkable agreement between the simulation outcomes and the results obtained from Finite Element Method (FEM) analysis of the derived equations, reaffirming the robustness of our proposed framework.

Looking ahead, experimental verification of our results, such as through experiment like the VIP-DROP campaign ([68–70]), holds promise for further validation and refinement of our model.

Appendix

Appendix A: Methods of the Simulations

We performed our simulations with the open-source Navier-Stokes solver `BASILISK` [60]. Our code is similar to the one of [71]. We chose an accuracy level of 9. Our simulations were carried out in a box of the size 20×10 length units to reduce finite-size effects.

The wetting height h_∞ is in our examples given by 0.001. If nothing else is mentioned, our simulations were carried out in 3 dimensions, using a cylindrical symmetry.

The densities of the droplet and the surrounding fluid are given by $\rho_{\text{fluid}} = 1$ and $\rho_{\text{surr}} = 0.001$. The viscosities are given by $\mu_{\text{fluid}} = 0.1$ and $\mu_{\text{air}} = 0.0002$. The shear-modulus is given by $G_\infty = 10$. If we do not mention anything else, the surface tension is set to $\hat{\sigma} = 10$. For the analysis, we made use of the python-library `scipy.interpolate` to interpolate the data with an accuracy of 0.001 on a regular grid. With this grid, we get the maximal height by reading out the centerline.

Appendix B: Methods of the FEM-analysis

For the Finite-Element analysis, we made use of the open-source package `fenics` (version 0.8). As a basis for our numerical analysis, we take the thin-film equation for Jeffrey's model which was derived by [50]. The corresponding system of equations can be written in the following form:

$$\begin{aligned} Q_\parallel + \tau_2 \partial_t Q_\parallel &= \nabla_\parallel p_R \\ R_\parallel + \tau_2 \partial_t R_\parallel &= h \cdot \nabla_\parallel p_R \\ (1+\tau_2\partial_t)\partial_t h + (\tau_2 - \tau_1)\nabla_\parallel \cdot \Big[\Big(\frac{h^2}{2} Q_\parallel - h R_\parallel\Big)\partial_t h\Big] & \\ = \nabla_\parallel \cdot \Big\{(1-\tau_1\partial_t)\frac{h^3}{3}\nabla_\parallel p_R\Big\} & \end{aligned} \tag{A.41}$$

We identify the shear modulus G_∞ as $\tau_1^{-1} = \tau_2^{-1} + G_\infty/\eta$. Furthermore from the boundary conditions, it follows that $p_R = -\nabla_\parallel h$. We assume having a cylindrical symmetric geometry. In order to numerically analyze the equation, we develop the weak statement of the system of equations. To so so, we introduce the test functions q, r, v and w. Then, both sides of the equation are multiplied by a test function and finally one integrates over the volume. To

simplify the equation, one then makes use of partial integration. Furthermore, we introduce the function k, defined as $\partial_x^2 h = k$. For the first equation we get:

$$Q_\parallel \cdot q + \tau_2 \partial_t Q_\parallel \cdot q = \nabla_\parallel p_R \cdot q \tag{A.42}$$

$$\longrightarrow \int_\Omega dx Q_\parallel \cdot q + \tau_2 \int_\Omega dx \partial_t Q_\parallel \cdot q = -\int_\Omega dx \partial_x^3 h \cdot q \tag{A.43}$$

$$\longrightarrow Q_\parallel \cdot q \cdot dx + \tau_2 \partial_t Q_\parallel \cdot q \cdot dx + \partial_x k \cdot q \cdot dx = 0 \tag{A.44}$$

As an initail condition, we chose, similar to our simulations, $0.3 \cdot \cdot e^{-x^2}$.
All values were approximated by $h_{mid} = (1-\theta)h_0 + \theta h_0$, using $\theta = 0.5$.
The interval, on which the equations were solved, is given by $(0, 20)$. We used the pre-implemented NewtonSolver of Fenics with Lagrange Elements. Our timestep was chosen as 0.0001.

Velocity profiles of butane in a nanochannel

Introduction

Despite decades of intensive research, our understanding of hydrodynamics at the nanoscale remains incomplete. At such small length scales, where continuum assumptions may break down, molecular dynamics (MD) simulations provide a powerful and well-suited tool for investigation. Numerous MD studies have demonstrated that classical hydrodynamic laws remain valid down to surprisingly small length scales, even in strongly confined systems [72–76].

One particularly important nanoscale effect is the emergence of spatially inhomogeneous density profiles. As a consequence of confinement, fluid density can vary strongly across the channel, which in turn influences the flow behavior. Several studies have therefore investigated hydrodynamics in systems with inhomogeneous density. For example, Bitsanis et al. [77] and Dalton et. al [78, 79] studied Poiseuille flow in an infinite system with an imposed density gradient and observed pronounced deviations from the classical velocity profile in regions where the density varies spatially.

More recently, Knudsen et al. [80] and Heitmeier et al. [81] performed MD simulations of confined model fluids subjected to a spatially sinusoidal external force. Both studies reported that, in the

steady state, the velocity profile is not dominated solely by the externally excited mode; instead, lower modes contribute significantly to the flow field. However, a detailed analysis of the origin of these additional modes and their relation to the fluid structure was not provided.

In the present work, we address this issue by systematically relating the spectral properties of the velocity profiles to those of the density profiles. In contrast to previous studies employing model fluids, we investigate a molecular fluid, namely butane. Butane is of practical relevance due to its wide range of industrial applications, including its use as a fuel, refrigerant, and chemical feedstock, and thus serves as a realistic test system for nanoscale flow phenomena [82–84].

Our analysis is furthermore related to the work by Bitsanis et al. [77]. While their study focused on spatial deviations of the velocity profile in regions of varying density, we additionally demonstrate a clear correspondence between the spectral modes present in the density and velocity fields.

Furthermore, we show that the observed mode coupling effects are robust with respect to the wall morphology. Specifically, we find qualitatively identical behavior for both crystalline and amorphous walls over a range of wall densities. This observation is particularly important in light of recent findings by Marcelli et al. [85], who demonstrated that wall morphology can significantly influence the shape of the density profile.

The remainder of this paper is organized as follows. First, we introduce the theoretical framework underlying our analysis. Next, we describe the Molecular Dynamics simulation methodology. Finally, we present and discuss the results for different wall morphologies and wall densities.

Theory

The investigated system is butane confined between parallel walls, which are semi-infinite. We impose the external force

$$F_{ext} = \rho(z) \cdot A \cdot \sin(k_n z) \tag{A.45}$$

Here, $\rho(z)$ is the density profile, A is the amplitude, and $k_n = 2\pi n/h$ is the external wavevector, and h is the channel height.

The aim is now to derive the velocity profile predicted from hydrodynamics. For sufficiently small Reynolds-numbers, the momentum balance equation can be written as [86]

$$\rho \frac{\partial u}{\partial t} = F_{ext} - \frac{\partial P_{xz}}{\partial z} \tag{A.46}$$

Here, u is the velocity of the fluid in x-direction and P_{xz} is the relevant component of the pressure tensor. For a Newtonian fluid, we can assume this tensor to be given by Newton's law of viscosity:

$$P_{xz} = -\eta_0 \frac{\partial u}{\partial z} \tag{A.47}$$

using the shear viscosity η_0. By substituting, we get the following relation between the velocity profile u and the density profile ρ:

$$\frac{d^2 u(z)}{dz^2} = -\frac{A\rho(z)}{\eta_0} \sin(k_n \cdot z) \tag{A.48}$$

As mentioned above, we assume the density of the fluid to be non-homogenous. Hence, we model it by

$$\rho(z) = \sum_{i=0} \rho_i \cos(k_i \cdot z) \tag{A.49}$$

Here, ρ_0 is the bulk density, which in in our case around 1.48 by definition. We made use of a similar definition for the wavevectors

as above, $k_i = 2\pi i/h$. Additionally, we assume the resulting velocity profile to also have the form:

$$u(z) = \sum_{m=0}^{\infty} u_m \sin(k_m z) \tag{A.50}$$

Hence, the second derivative with respect to z is given by:

$$\frac{d^2}{dz^2} u(z) = -\sum_{m=0}^{\infty} u_m k_m^2 \sin(k_m z)$$

Similarly, the density can be written as

$$\rho(z) = \sum_{i=0} \rho_i \cos(k_i \cdot z) \tag{A.51}$$

Here, ρ_0 is the bulk density, which in in our case around 1.48 by definition. The aim is to determine u_m in dependence of ρ_i for a given k_n. Hence, we can insert the approach in equation (A.48):

$$\begin{aligned}
-\sum_{m=0}^{\infty} u_m k_m^2 \sin(k_m z) &= -\frac{A}{\eta} \sum_{i=0} \rho_i \cos(k_i z) \sin(k_n z) \\
\Leftrightarrow \sum_{m=0}^{\infty} u_m k_m^2 \sin(k_m z) &= \frac{A}{\eta} \sum_{i=0}^{\infty} \rho_i \frac{1}{2} \left[\sin((k_n + k_i)z) + \sin((k_n - k_i)z)\right] \\
\Leftrightarrow \sum_{m=0}^{\infty} u_m k_m^2 \sin(k_m z) &= \frac{A}{2\eta} \left[\sum_{i=0}^{\infty} \rho_i \sin((k_n + k_i)z) + \sum_{i=0}^{\infty} \rho_i \sin((k_n - k_i)z)\right]
\end{aligned} \tag{A.52}$$

From this, one can identify that the velocity modes m couple to the density modes via $m = n \pm i$.
The velocity mode u_m can hence be written as $u_m k_m^2 = \frac{A}{2\eta} \sum \rho_i$, with i being the solution(s) of $m = n \pm i$, and noting that $i > 0$. This formula can be used to be compared to our simulation data.

Simulations

Potential and Parameters

We perform MD-Simulations of butane with the open-source code `gamdpy` [87, 88]. A snapshot of the simulations can be seen in figure A.19.

In the following, we make use of Lennard-Jones units, which can be converted to real units by using $\sigma = 3.9\text{Å}$ and $\epsilon/k_B = 72.1K$. The mass is set to $m^* = 14.5u$. Butane is modeled by the Ryckeart-Bellemann model for alkanes [89–91]. It models torsional (dihedral) interactions, i.e., the energy associated with rotation around a bond (like C–C bonds in hydrocarbons). This is crucial for getting realistic molecular conformations. The basic idea of this model is that instead of using a simple cosine series like many dihedral potentials, the RB model expresses the torsional energy as a polynomial in $\cos\phi$:

$$V(\phi) = \sum_{n=0}^{5} C_n(\cos(\phi))^n \tag{A.53}$$

The exact parameters of our system can be seen in table A.3.
The system is set up in two steps: First, we set $N = 8000$ molecules on a regular grid, then we compress it, until it has the desired density. This system is then equilibrated in the NVE-ensemble. After that, two types of walls are set: For the case of a crystalline wall, we simply set particles on an FCC lattice. For the case of an amorphous wall, we set the particles on an FCC-lattice, and let the material melt for 500τ at $T = 2.0$. We checked that the resulting material is amorphous by investigating the corresponding pair-correlation function.

The particles are then tethered to their positions by using a spring constant of $k = 500$. Finally, wall and fluid system are combined, such that one models a fluid in a nanochannel of width L_z. Here, L_z is the distance between the walls.

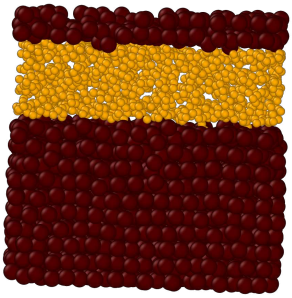

Figure A.19: Schematic setup of the simulations. Brown particles are wall atoms, orange ones correspond to the butane.

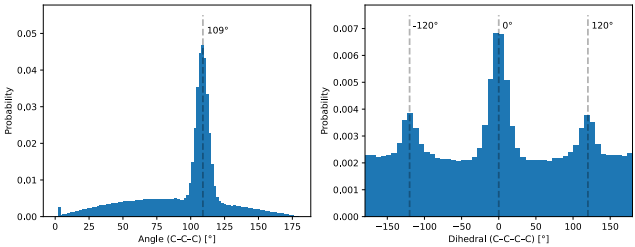

Figure A.20: Angle and dihedral distribution of a bulk system with 200 molecules.

The interaction between walls and C-atoms is modeled with a Lennard-Jones potential, taking similar values as [81].

The individual molecules are modeled by using a bond, angle and dihedral potential, with parameters shown in table A.3. A schematic setup of the simulations can be seen in figure A.19.

To validate the molecular model of butane, we analyzed the angular and dihedral distributions of the molecules. The resulting distributions, shown in Fig. A.20, are in good agreement with theoretical expectations. In particular, the bond angle distribution is centered around 109°, while the dihedral angle distribution exhibits the char-

quantity	value (LJ units)
density ρ	1.477
temperature T	4.16
mass m_C , mass wall m_{Wall}	1, 4.3
bond parameters L_{bond}, k_{bond}	0.4, 33e3
angle parameters α_{ang}, k_{ang}	1.9, 866
dihedral parameters	15.5000, 20.3050, -21.9170, -5.1150, 43.8340, -52.6070
interaction $C-C$: $\sigma_{CC}, \epsilon_{CC}$	1,1
interaction $C-$ wall:$\sigma_{CW}, \epsilon_{CW}$	1,1

Table A.1: Parameters which were used in the simulations. The atoms of the fluid should represent butane; the ones of the wall are chosen similar to the values of copper.

acteristic gauche and trans conformations.

As a further validation of our simulation setup, we investigated Poiseuille flow through a nanochannel. The resulting density profiles show the expected behavior, including pronounced layering near the walls and a homogeneous density in the channel center. Within the range of external forces and butane densities considered in this study, no significant changes in the density profile were observed. After equilibrating, we imposed a sinusoidal force on the system:

$$F_{ext}(z) = A \cdot \sin(k_n z) \tag{A.54}$$

Here, A is the force amplitude, and k_n is the wavevector, defined by $k_n = \frac{2\pi n}{h_{\text{eff}}}$. Here, h_{eff} is the effective channelwidth, which is specific for each system. We measured it by defining the region in which the density is at least 0.1. A list of effective densities can be found in table A.2. To determine the force amplitude A, we performed simulations for different A. By checking that u/A is a constant, we validated that the values we chose were still in the linear regime of

system	ρ_{Wall}	$L_z = 5.5$	$L_z = 10$	$L_z = 15$	$L_z = 20$
amo	0.8	5.10	9.57	14.60	19.55
amo	1.0	4.76	9.28	14.21	18.28
FCC	1.0	–	8.81	13.65	19.12
FCC	2.2	–	8.05	12.94	17.82

Table A.2: Effective channel widths of the different wall morphologies and wall distances L_z. The systems where we do not report an effective channel width are not included in the analysis of velocity profiles.

viscosity. The values we chose for the production run were then in the range between 0.05 to 0.35.

Results

Figure A.21 shows the density profiles of butane confined in a nanochannel for different wall morphologies and channel widths. In agreement with previous studies [85], pronounced density oscillations are observed in the vicinity of the walls. The figure further demonstrates that the wall morphology strongly influences the shape of the density profile. While crystalline walls lead to sharply defined layering, the density profile near amorphous walls increases more gradually toward the channel center.

Figure A.22 illustrates the density profile for the case of an amorphous wall together with a fit using Eq. (A.49) with 50 terms. By varying the number of terms, we checked that the obtained results do not rely specifically on the number of fitting parameters. The fitted profile reproduces the simulation data very accurately. The central panel of the figure displays the individual density modes ρ_i, which correspond to the modes previously identified in Ref. [92]. The right panel shows the difference between the actual force density and the

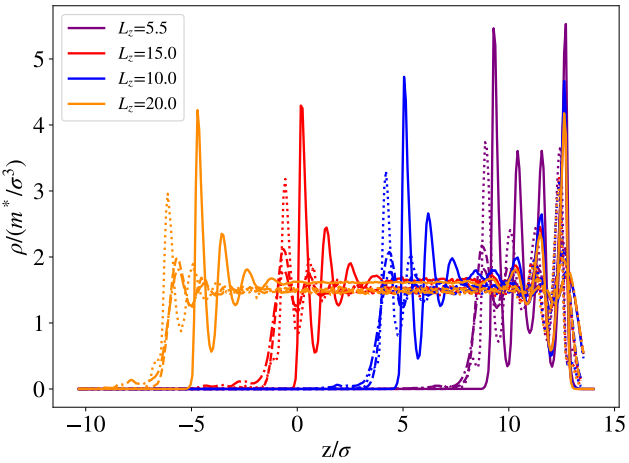

Figure A.21: Density profile of the C-atoms in the nanochannel for a constant force of strength $A = 0.05$. We checked that the density profile does not change, if a different force is applied ($A \leq 0.35$). Solid lines correspond to FCC with $\rho = 2.2$ (dotted: $\rho = 1.0$), dashed lines correspond to an amorphous wall with $\rho = 1.0$ (dashdot: $\rho = 0.8$).

force density expected for a homogeneous system, defined as

$$\rho(z)\, A \sin(k_n z) - \rho_{\text{bulk}}\, A \sin(k_n z). \tag{A.55}$$

It is evident that deviations from the expected force, and consequently from the ideal velocity profile, become increasingly pronounced near the walls. This effect must therefore be taken into account when interpreting velocity profiles in confined systems.

Figure A.52 presents the steady-state velocity profiles for different wall morphologies (crystalline and amorphous), external forcing wavelengths k_n, and channel widths. The black solid lines represent fits obtained from Eq. (A.52), where the density modes extracted from the density profile fits are used as input. In this fitting procedure, the viscosity is the only adjustable parameter. Remarkably, a single value of $\eta = 3.8$ provides an excellent description of all cases considered.

Finally, Fig. A.24 compares velocity profiles obtained for different wall morphologies. These results indicate that the wall structure has a stronger influence on the velocity profile than the wall density. In particular, for amorphous walls the contribution of the first velocity mode is significantly weaker than in the crystalline case. We attribute this behavior to differences in the slip properties of the walls. This trend is also clearly reflected in the corresponding spectral representations shown in the figure.

Discussion and outlook

In this paper, we have investigated the steady-state velocity profiles of butane confined in nanochannels. In contrast to previous studies of fluid flow under nanoconfinement, which predominantly focused on model fluids, we considered a molecular fluid with direct technological relevance. We demonstrated that the velocity profiles exhibit contributions from multiple modes and showed that these

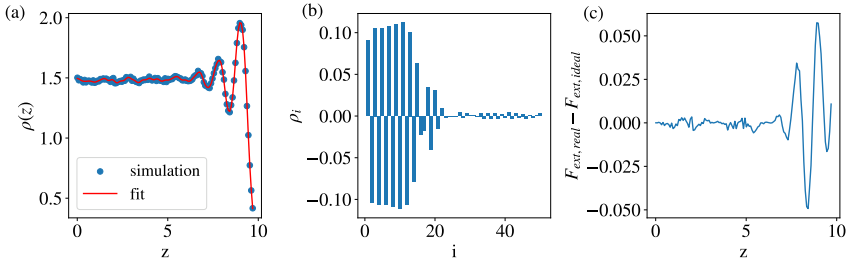

Figure A.22: Illustration of the fitting procedure. Left: Density profile with fitted modes, using 50 terms. Center: Modes of the density profile. Right: Force density of the problem.

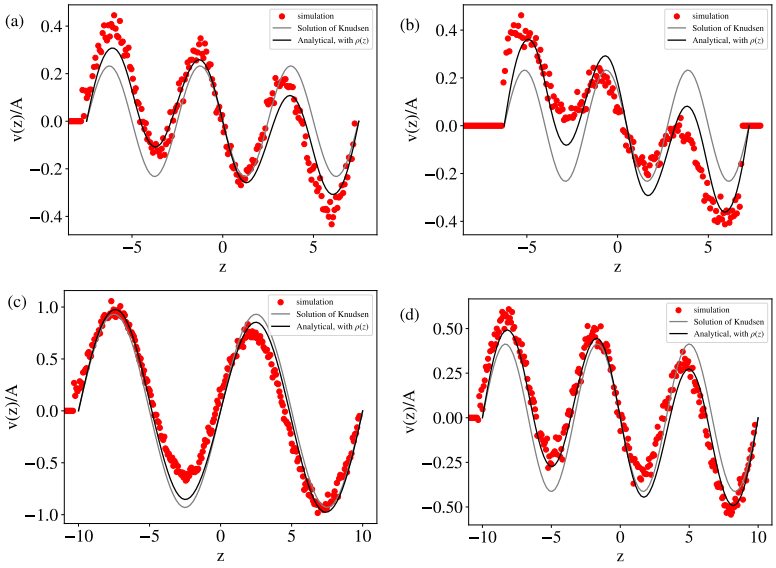

Figure A.23: Fitted velocity profiles, using formula (A.52). (a): $L_z = 15, n = 3$ for an amorphous wall with $\rho = 1.0$. (b): $L_z = 15, n = 3$ for an FCC wall with $\rho = 2.2$. (c): $L_z = 20, n = 2$ for an amorphous wall with $\rho = 1.0$. (d): $L_z = 20, n = 3$ for an amorphous wall with $\rho = 1.0$.

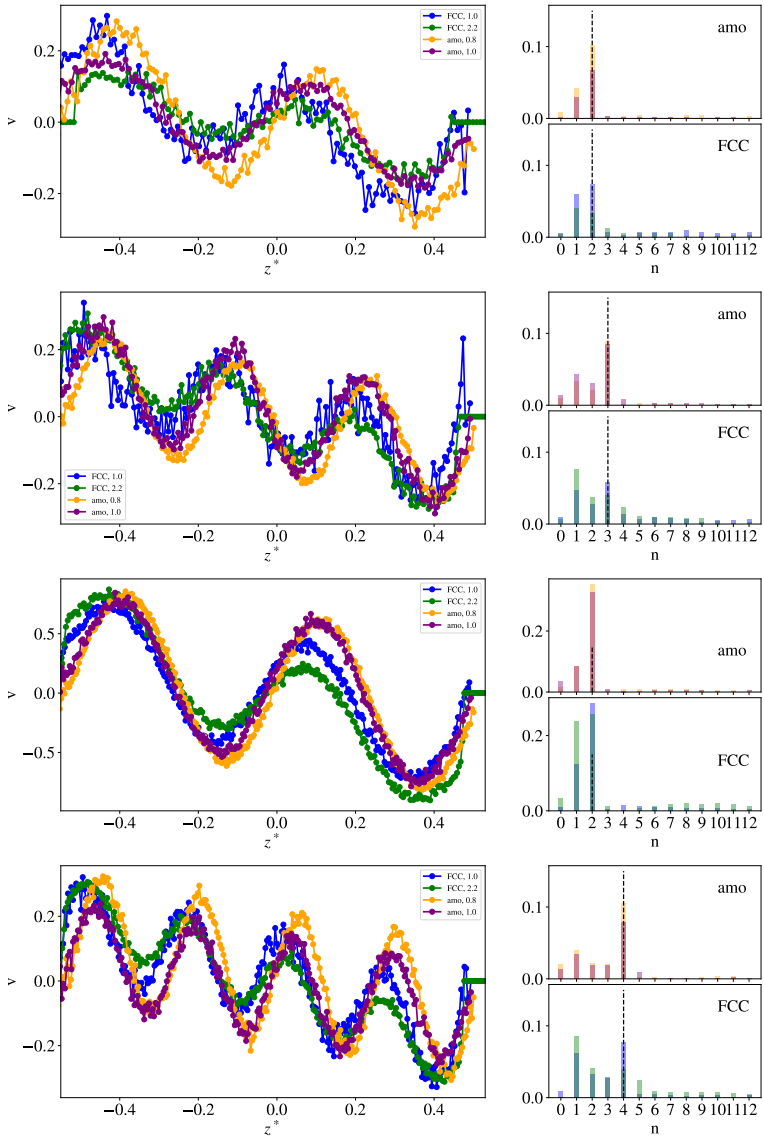

Figure A.24: Comparison of the velocity profiles for different wall morphologies. One can observe that only modes smaller than the excited mode contribute to the profile. From top to bottom: $L_z = 10, n = 2$; $L_z = 15, n = 3$; $L_z = 20, n = 2$ and $L_z = 20, n = 4$

additional modes can be directly related to oscillations in the density profile induced by confinement. By relating the density modes to the modes of the velocity, we also showed that hydrodynamic laws are still valid on these lengthscales, as also discussed by [74].

Furthermore, we developed a systematic procedure that allows for an accurate prediction of the velocity profile in a nanochannel based solely on the corresponding density profile. We demonstrated that this approach is robust with respect to variations in both wall morphology and channel width, yielding consistent results for crystalline and amorphous walls alike.

Future work will extend this study to other molecular fluids and explore a more direct theoretical connection to the Yvon–Born–Green equation. This framework offers the possibility to determine density profiles analytically using a limited set of approximations [77]. Ultimately, such an approach could enable the prediction of velocity profiles without the need for prior density measurements, which would be of considerable technological interest.

Particle Dynamics in Vibrated Granular Systems: A DEM Study

We perform Discrete-Element simulations of granular particles, which are shaken inside a finite box. Specifically, we study the evolution of the packing fraction for different shaking amplitudes, as well as the Mean-Squared Displacements. By this, we relate the system's behavior to the behavior of glassy systems. A comparison with experiments shows that the MSDs from the simulations are significantly higher than the measured ones in [93]. We propose two explanations for this derivation: Either the amplitude of the experiment is smaller than expected, or the experiment is measuring the rotational MSD instead of the translational MSD. We show that also from simulations, we obtain rotational MSDs, which are much smaller than the translational ones.

Introduction

Granular matter has a wide range of applications in both biological and industrial processes. Some examples include snow, nuts, coal, and rice [94–97]. One of the most important applications is additive manufacturing, where the flow properties of the filament, which can be granular matter, are of high importance for the resulting printing quality [98–100].

The research of the last years showed that the behavior of dense granular matter can be well compared to the one of dense liquids, showing a behavior similar to the one of a glass-forming fluid [101–104]. In contrast to fluids, where for the energy supply thermal excitation can be used, for the investigation of granular systems the main challenge is the way how energy can be brought into the system. One common way to come up with this challenge is the use of a vibration of the system. Experimentally, this method has for example been used in Refs. [93, 105–107], but simulations of this setup are still lacking [108–110].

The aim of the following work is to fill this gap, and to perform Discrete-Element simulations of a vibrated granular system. During the shaking process, we track both statical and dynamical properties: We investigate the volume fraction, and the Mean-Squared Displacement (MSD) during the process. By this, we can also relate the density to the dynamics of the system. Similar to glassy systems, we find that even very small changes in the density can significantly change the dynamics of the system.

We get a qualitative agreement to experimental findings, but regarding quantities, there are still differences between simulations, experiments, and theoretical prediction. In simulations, we find caging effects at a distance of around $0.01d$, where d is the particle diameter. This is in agreement with a theoretical prediction from Mode-Coupling Theory, which predicts the caging to occur at 7% of the particle diameter In contrast, in experiments, caging was found to be at 0.07% of the particle diameter [93].

We conclude our paper by shortly discussing the rotational MSD

(rMSD), as its order of magnitude is fitting to the order measured in the experiments. We note that investigations of the rMSD are rare in literature, for example they are discussed in [111, 112]. For granular systems, this property has not been investigated and is strongly dependent on the tangential components of the interparticle interactions.

Simulations

We performed Discrete-Element simulations (DEM) using the open-source software `LAMMPS` [113]. The interactions between particles were modeled using a Hookean contact law, where particles experience a force only when they overlap. The corresponding pairwise force is given by [102, 114, 115]:

$$\mathbf{F}_{\text{Hooke}} = (k_n \, \delta \, \mathbf{n}_{ij} - m \, \gamma_n \, \mathbf{v}_n) - (k_t \, \Delta \mathbf{s}_t + m \, \gamma_t \, \mathbf{v}_t), \tag{A.56}$$

where δ is the overlap between two particles, k_n and k_t denote the elastic constants in the normal and tangential directions, respectively, and γ_n and γ_t are the corresponding damping coefficients. The variable m represents the particle mass, while $\mathbf{v}_n$ and $\mathbf{v}_t$ are the normal and tangential components of the relative velocity. The vector $\Delta \mathbf{s}_t = \int dt v_t$ accounts for the tangential displacement between two particles and includes the history of tangential contacts. In some cases, we also made use of the static yield criterion. If not mentioned else, it is set to 0.

Initially, N particles were placed randomly within a rectangular box of dimensions $L_x \times L_y \times L_z$. A gravitational force of magnitude mg was applied in the negative z-direction to induce particle settling and segregation. The boundaries of the simulation box were modeled as walls interacting with the particles through the same Hookean potential, but with different interaction parameters (see Table A.3). The setup after the segregation is illustrated in figure A.25.

Subsequently, a sinusoidal excitation was imposed by oscillating all walls with amplitude A and angular frequency ω, such that the z-position of the walls w_z were at time t given by

$$w_z(t) = w_z(0) + A \sin\left(\frac{2\pi t}{\omega}\right) \tag{A.57}$$

During the shaking process, we monitored the evolution of the *volume fraction*, and the *mean-squared displacement (MSD)*. For the beginning of the process, we also tracked the *rotational mean-squared displacement (rMSD)*.

The volume fraction ϕ was determined as the ratio of the number of particles N to the "effective" system volume, defined by the minimal and maximal particle coordinates in each direction:

$$\phi = \frac{N}{\prod_{c=x,y,z} c_{\max} - c_{\min}} \tag{A.58}$$

We checked that the results, we obtain from this method are consistent with an alternative approach, which calculates the density of the system in dependence of the z-coordinate.
The translational mean-squared displacement was calculated as

$$\mathrm{MSD}(t) = \langle\, |\mathbf{r}(t) - \mathbf{r}(0)|^2 \,\rangle, \tag{A.59}$$

where $\mathbf{r}(t)$ denotes the particle position at time t, and the brackets $\langle\cdot\rangle$ indicate an ensemble average over all particles. For the calculation of this quantity, we made use of the in-build methods of `LAMMPS`, which calculates the MSD [116].
The rotational mean-squared displacement was obtained from the time-integrated angular velocity $\boldsymbol{\omega}(t)$ of each particle, scaled by the particle diameter d:

$$\mathrm{RMSD}(t) = \frac{d}{2}\,\frac{\pi}{180}\int_0^t |\boldsymbol{\omega}(t')|\, dt'. \tag{A.60}$$

This quantity provides a measure of the particle's reorientation due to rotational motion.

quantity	value
particle diameter d	140×10^{-6}
density ρ	1600
number of particles N	20000
box lengths L_x, L_y, L_z	$0.004, 0.004, 0.004$
gravitational acceleration g	9.81
elastic stiffness k_n, k_t	$33.81,\ 4.52$
damping constant γ_n, γ_t	$1.01 \times 10^4,\ 9.08 \times 10^3$
wall stiffness k_n^{wall}, k_t^{wall}	$90.55,\ 1.22 \times 10^4$
wall damping $\gamma_n^{\text{wall}}, \gamma_t^{\text{wall}}$	$1.97 \times 10^4,\ 1.77 \times 10^4$
shaking frequency $\hat{\omega}$	100
shaking amplitude A	1×10^{-5} to 3×10^{-5}
dynamic yield criterion	$0, 1$

Table A.3: Parameters used in the simulations. Interpreted in SI-units, the values are comparable with those of polysterene, but a precise mapping between material properties and parameters in the model is still lacking [121].

All results are the average over at least 5 different initial configurations.

The simulation parameters are summarized in Table A.3. The material properties were chosen to resemble those of polystyrene particles (Dynoseeds 140), adopting parameter values consistent with previous studies [117–120]. Note that despite of decades of research, the exact parameters, which should be used in the Hookean spring model, are still unknown [121].

Results

Density development

During the shaking process, we tracked the volume fraction of the particles. This can be seen in figure A.26. It turns out that the

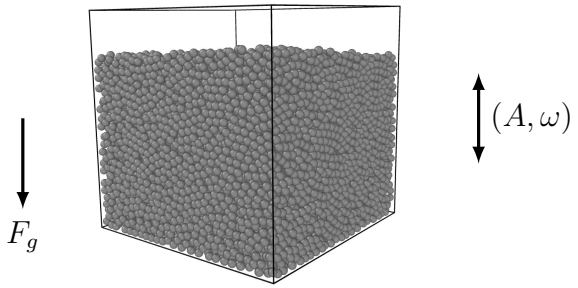

Figure A.25: Schematic representation of the simulation setup after the segregation. The gravitational force F_g acts downward, while the container walls oscillate vertically with amplitude A and frequency ω.

densification highly depends on the shaking amplitude. For very small amplitudes, the system densifies very slowly, for intermediate ones, it densifies more fastly, and for large amplitudes we do not see densification anymore. This behavior can be explained by the following thoughts: Shaking a system means inserting energy into it. If we insert much energy into it, all particles are fluidized, if the energy is smaller, the particles can use the energy to reorder themselves and by this, approaching the most favorable state.

Mean-Squared Displacement

During the shaking process, we also track the MSD. Here, we see a phenomenon, which is well established in the physics of glasses. The MSD consists of two different time regimes: For small timescales, the system shows a ballistic behavior,*i.e.* the MSD is behaving like $\propto t^2$. For large timescales, the system is behaving diffusive, *i.e.* the MSD is linear in time. We can identify both regimes in the

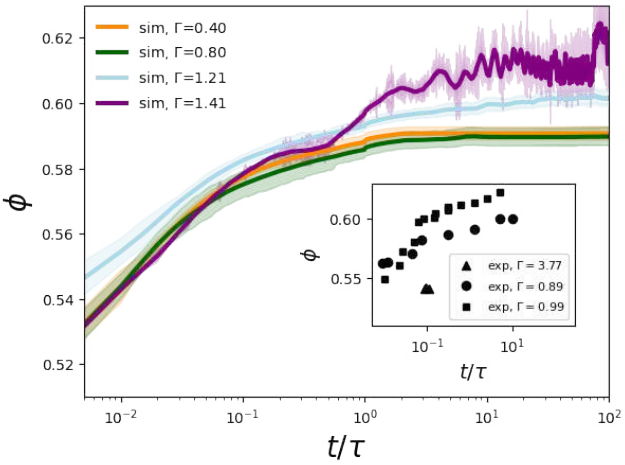

Figure A.26: Density evolution of the system for $A = 3 \times 10^{-5}$ (blue), $A = 2 \times 10^{-5}$ (green), and $A = 1 \times 10^{-5}$ (orange). The light lines correspond to single configurations, the dark ones to the mean value. The black data points correspond to the experimental data from [93]. The timescale is normed, such that $\tau_{\text{sim}} = 1000\tau_{\text{exp}} = 11\,\text{s}$. The gray lines correspond to cases with finite x_μ.

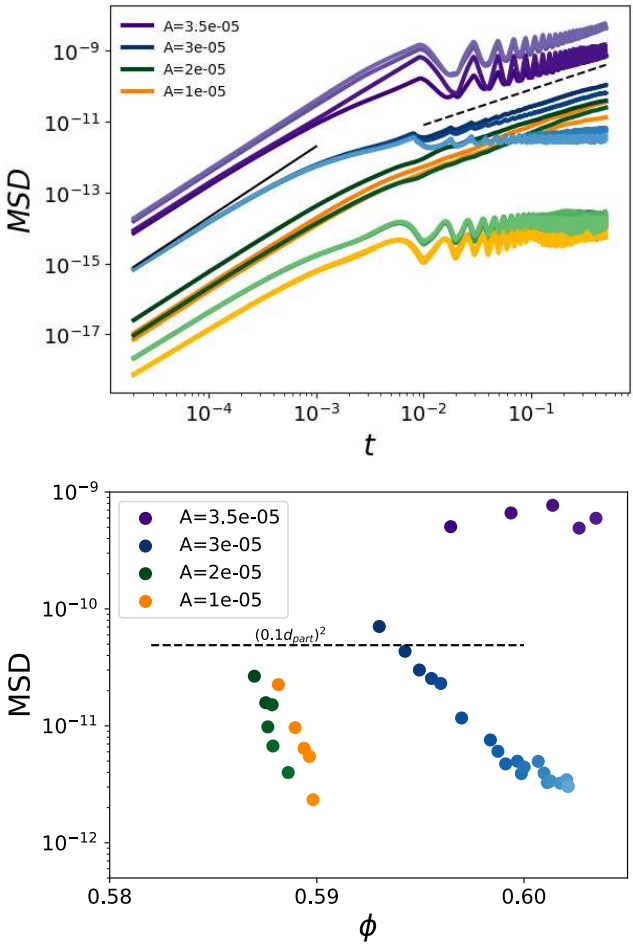

Figure A.27: MSDs of the particles during the shaking process. Light lines correspond to earlier times, while dark ones correspond to late times. We show the MSDs for different shaking amplitudes $A = 3 \times 10^{-5}$ (blue), $A = 2 \times 10^{-5}$ (green), and $A = 1 \times 10^{-5}$ (orange). As indicated in the legend, the gray lines for orientation correspond to t, and t^2 respectively. The lower image shows that there is not a unique relation between MSD and packing fraction. This indicates that the MSD is history-dependent.

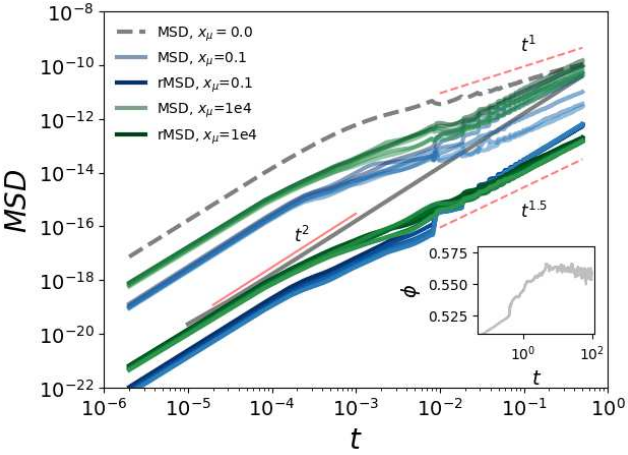

Figure A.28: Comparison of translational MSD and rotational MSD for different values of x_μ (static yield criterion), i.e. tangential forces play a role here. It turns out that for our choice of parameters, the rotational MSD differs from the translational MSD with a factor of 1×10^4. A super-diffusive behavior was also observed by Scalliet et al. in [112]. The extend of super-diffusivity is dependent on the static yield criterion.

MSDs from the simulations. As the time progresses, which means that the density is increasing, the MSD shows a plateau, which can be related to the caging-phenomenon. This caging becomes more and more pronounced when the system is denser. A decrease of the amplitude makes the dynamics slower, i.e. the MSDs are becoming smaller.

Comparison to experiments

Notably, a comparison to experiments [93] shows that the order of the MSD, which is obtained in experiment differs for around a factor of 100, although the simulation parameters were chosen

such that they are similar to the expected values for the same material. From our simulations, we do not only get information about the particle positions and center-of-mass velocities, but also about the angular velocities. From this, we determined the rMSDs, as explained in the section above. It turns out that the rMSD is indeed smaller than the MSD, and the order of the rMSD is fitting to the measured one. From this, we propose that the method used by Kunzner et al does not measures the translational MSD as stated in their work [93], but the rotational MSD.
Due to computational limitations, we are not able to study the rMSD for the whole process. Additionally, one should note that the behavior of the rMSD strongly depends on the parameters k_t and γ_t, which are to large parts unknown.

Summary

In this paper, we investigated the dynamics of granular matter during vibration by means of DEM-simulations. First, in agreement to both experiments and expectation, we found that the density of the system increases during the shaking process. This increase is characterized by the amplitude of the vibration. We find that the final values of the density differ from amplitude to amplitude.
After that, we studied the dynamics of the system during the vibration by studying the MSD during the densification. Here, it turns out that the qualitative behavior of the system is very similar to the behavior observed in experiments. We propose a few hypotheses for the derivations regarding the quantities: Firstly, experimental errors cannot be completely ruled out. For example, the determination of the amplitude is very challenging. A different shaking amplitude would clearly change the exact numbers of the MSD. Additionally, the exact parameters of the model used in the simulations are still

unclear [121]. Also, different parameters for the spring constants or damping coefficient would in principle change the MSD.
The most likely reason for the derivation is also investigated in the current paper. We find that the order of magnitude of the rMSD is similar to the MSD measured in the experiment. This similarity lets us suspect that in the experiments, the rotation of the particles was characterized, instead of the translational motion.
In a future project, the authors will investigate the rotational MSD in detail. Additionally, the influence of the strength of gravitational forces and of the wall interactions will be studied. Specifically, the segregation of granular particles under various gravitational forces is still poorly understood.
Also the behavior of the rMSD should be studied in detail. Specifically, until now it is not fully understood in which cases superdiffusion occurs. A detailed analysis of this would significantly enhance the underlying processes. Finally, the exact parameters which should be used to perform simulations of polysterene should be determined.

References to the Addendum

[1] K. Song, R. Zhao, J. Liu, Y. Wang, E. Lindgren, Y. Wang, S. Chen, K. Xu, T. Liang, P. Ying, et al., *Nature Communications* **2024**, *15*, 10208.

[2] J. Brillo, Thermophysical properties of multicomponent liquid alloys, Walter de Gruyter GmbH & Co KG, **2016**.

[3] Y. J. Lv, M. Chen, *International Journal of Molecular Sciences* **2011**, *12*, 278–316.

[4] S. Terekhov, *Inorganic Materials* **2023**, *59*, 926–931.

[5] S. Li, X. Yue, Q. Li, H. Peng, B. Dong, T. Liu, H. Yang, J. Fan, S. Shu, F. Qiu, et al., *Journal of Material Research and Technology* **2023**, *27*, 944–983.

[6] A. A. Alghannam, M. S. Soliman, A. H. Seikh, I. A. Alnaser, A. Fouly, J. A. Mohammed, S. A. Ragab, H. S. Abdo, *Scientific Reports* **2023**, *13*, 11535.

[7] J. R. Davis et al., Aluminum and aluminum alloys, ASM international, **1993**.

[8] B. N. Bhat, Aerospace Materials Characteristics, tech. rep., Reston, VA, **2018**, Chapter 2, pp. 11–208.

[9] Y. Plevachuk, I. Egry, J. Brillo, D. Holland-Moritz, I. Kaban, *International Journal of Material Research* **2007**, *98*, 107–111.

[10] J. Brillo, I. Egry, J. Westphal, *International Journal of Material Research* **2008**, *99*, 162–167.

[11] H. Peng, T. Voigtmann, G. Kolland, H. Kobatake, J. Brillo, *Physical Review B* **2015**, *92*, 184201.

[12] H. Sheng, M. Kramer, A. Cadien, T. Fujita, M. Chen, *Physical Review B* **2011**, *83*, 134118.

[13] R. R. Zope, Y. Mishin, *Physical Review B* **2003**, *68*, 024102.

[14] N. Li, Z. Hao, L. Xu, M. Tang, L. Wei, L. Wang, *Metals* **2024**, *14*, 1018.

[15] A. Fellman, J. Byggmästar, F. Granberg, K. Nordlund, F. Djurabekova, *Physical Review Materials* **2025**, *9*, 053807.

[16] J. Sandberg, T. Voigtmann, E. Devijver, N. Jakse, *arXiv preprint arXiv:2410.07886* **2024**.

[17] Z. Zhao, M. Yi, W. Guo, Z. Zhang, *Physical Review B* **2024**, *110*, 184115.

[18] A. Rahman, M. S. Hossain, A.-B. Siddique, *Journal of Materials Science* **2025**, *60*, 12189–12221.

[19] T. Liang, K. Xu, E. Lindgren, Z. Chen, R. Zhao, J. Liu, E. Berger, B. Tang, B. Zhang, Y. Wang, K. Song, P. Ying, N. Xu, H. Dong, S. Chen, P. Erhart, Z. Fan, T. Ala-Nissila, J. Xu, *arXiv preprint arXiv:2504.21286* **2025**.

[20] S. Liu, G. Zhang, F. Yin, A. A. Barinov, V. I. Khvesyuk, N. Yang, *Journal of Applied Physics* **2025**, *138*, 104301.

[21] J. Zhang, Z. Zhao, M. Jiang, Y. Cheng, G. Zhang, *Physical Review Materials* **2025**, *9*, 094603.

[22] X. Jia, Y. Bao, S. Cao, Y. Su, P. Qian, *Journal of Nuclear Materials* **2025**, *616*, 156025.

[23] D. Holland-Moritz, O. Heinen, R. Bellissent, T. Schenk, *Materials Science and Engineering: A* **2007**, *449*, 42–45.

[24] A. P. Thompson, H. M. Aktulga, R. Berger, D. S. Bolintineanu, W. M. Brown, P. S. Crozier, P. J. In't Veld, A. Kohlmeyer, S. G. Moore, T. D. Nguyen, et al., *Computer physics communications* **2022**, *271*, 108171.

[25] J. Brillo, J. J. Harpur, H. Kobatake, H. Fukuyama, *International Journal of Thermophysics* **2025**, *46*, 188.

[26] M. Mohr, Y. Dong, G. Bracker, D. Matson, R. Zboray, R. Frison, A. Domman, A. Neels, X. Xiao, J. Brillo, R. Busch, R. Novakovic, P. Srirangam, H.-J. Fecht, *npj microgravity* **2023**, *9*, 34.

[27] J. Brillo, F. Yang, D. Holland-Moritz, *International Journal of Thermophysics* **2024**, *45*, 17.

[28] P.-F. Paradis, T. Ishikawa, G.-W. Lee, D. Holland-Moritz, J. Brillo, W.-K. Rhim, J. Okada, *Materials Science and Engineering R* **2014**, *76*, 1–53.

[29] O. Takeda, H. Yoneda, Y. Sato, *International Journal of Thermophysics* **2025**, *46*, 154.

[30] J. Brillo, J. J. Harpur, H. Kobatake, H. Fukuyama, *International Journal of Thermophysics* **2025**, *46*, 188.

[31] J. Brillo, J. J. Wessing, H. Kobatake, H. Fukuyama, *High Temperatures-High Pressures* **2019**, *48*, 423–438.

[32] L. Verlet, *Physical Review* **1968**, *165*, 201.

[33] J.-P. Hansen, I. R. McDonald, Theory of simple liquids: with applications to soft matter, Academic press, **2013**.

[34] W. Gąsior, *Calphad* **2014**, *44*, 119–128.

[35] R. Novakovic, D. Giuranno, M. Mohr, J. Brillo, H.-J. Fecht, *International Materials Reviews* **2024**, *69*, 63–79.

[36] F. Pabst, S. Baroni, *Physical Review E* **2025**, *111*, L023401.

[37] A. van der Bos, M.-J. van der Meulen, T. Driessen, M. van den Berg, H. Reinten, H. Wijshoff, M. Versluis, D. Lohse, *Physical review applied* **2014**, *1*, 014004.

[38] P. A. Schweitzer, Paint and coatings: applications and corrosion resistance, CRC press, **2005**.

[39] C. Arcoumanis, M. Gavaises, B. French, *SAE transactions* **1997**, 1025–1064.

[40] A. L. Yarin, *Annu. Rev. Fluid Mech.* **2006**, *38*, 159–192.

[41] V. Bergeron, D. Bonn, J. Y. Martin, L. Vovelle, *Nature* **2000**, *405*, 772–775.

[42] M. Xu, J. Zhang, R. Chen, *International Journal of Heat and Mass Transfer* **2022**, *183*, 122070.

[43] O. Reynolds, *Philosophical transactions of the Royal Society of London* **1886**, *177*, 157–234.

[44] N. D. Sylvester, J. S. Tyler, A. Skelland, *The Canadian Journal of Chemical Engineering* **1973**, *51*, 418–429.

[45] R. X. Dai, Q. Dong, A. Z. Szeri, *Journal of Tribology* **1992**, *114*, 14–25.

[46] J. Becker, G. Grün, *Journal of Physics: Condensed Matter* **2005**, *17*, S291.

[47] B. M. Pereira, G. A. Dias, F. S. Cal, K. R. Rajagopal, J. H. Videman, *Fluids* **2019**, *4*, 98.

[48] F. James, M. M'baye, K. Msheik, D. Nguyen, *ESAIM: Proceedings and Surveys* **2021**, *70*, 147–165.

[49] R. Hewson, N. Kapur, P. Gaskell, *Journal of non-newtonian fluid mechanics* **2009**, *162*, 21–28.

[50] M. Rauscher, A. Münch, B. Wagner, R. Blossey, *The European Physical Journal E* **2005**, *17*, 373–379.

[51] A. Münch, B. Wagner, M. Rauscher, R. Blossey, *The European Physical Journal E* **2006**, *20*, 365–368.

[52] J. King, *Mathematical and Computer modelling* **2001**, *34*, 737–756.

[53] S. G. Lampaert, R. A. van Ostayen, *Tribology International* **2020**, *147*, 106160.

[54] M. Jalaal, B. Stoeber, N. J. Balmforth, *Journal of Fluid Mechanics* **2021**, *914*, A21.

[55] C. Datt, M. Kansal, J. H. Snoeijer, *Journal of Non-Newtonian Fluid Mechanics* **2022**, *305*, 104816.

[56] T. Voigtmann, *Current opinion in colloid & interface science* **2014**, *19*, 549–560.

[57] J. K. Kevorkian, J. D. Cole, Multiple scale and singular perturbation methods, Springer Science & Business Media, **2012**.

[58] H. Ahmed, L. Biancofiore, *Journal of Non-Newtonian Fluid Mechanics* **2021**, *292*, 104524.

[59] M. Jalaal, PhD thesis, University of British Columbia, **2016**.

[60] Basilisk: Adaptive Cartesian Grid CFD Framework, basilisk.fr/.

[61] S. Popinet, *Journal of Computational Physics* **2009**, *228*, 5838–5866.

[62] A. Prosperetti, Computational Methods for Multiphase Flow, Cambridge University Press, **2009**.

[63] G. Tryggvason, R. Scardovelli, S. Zaleski, Direct numerical simulations of gas–liquid multiphase flows, Cambridge University Press, **2011**.

[64] J. G. Oldroyd, *Proceedings of the Royal Society A* **1950**, *200*, 523–541.

[65] L. Tanner, *Journal of Physics D: Applied Physics* **1979**, *12*, 1473.

[66] P.-G. Gennes, F. Brochard-Wyart, D. Quéré, et al., Capillarity and wetting phenomena: drops, bubbles, pearls, waves, Springer, **2004**.

[67] S. L. Cormier, J. D. McGraw, T. Salez, E. Raphaël, K. Dalnoki-Veress, *Physical Review Letters* **2012**, *109*, 154501.

[68] O. D'Angelo, F. Kuthe, K. van Nieuwland, C. Ederveen Janssen, T. Voigtmann, M. Jalaal, *Review of Scientific Instruments* **2022**, *93*, 115103.

[69] O. D'Angelo, F. Kuthe, K. van Nieuwland, C. Ederveen Janssen, T. Voigtmann, M. Jalaal, *Review of Scientific Instruments* **2022**, *93*, 115103.

[70] L. Heitmeier, O. D'Angelo, M. Jalaal, T. Voigtmann, *Journal of Rheology* **2026**, *70*, 631–643.

[71] R. Figueiredo, C. M. Oishi, A. Afonso, I. Tasso, J. A. Cuminato, *International Journal of Multiphase Flow* **2016**, *84*, 98–115.

[72] J. Koplik, J. Banavar, J. Willemsen, *Physics of Fluids* **1989**, *1*, 781–794.

[73] K. P. Travis, D. J. Evans, *Physical Review E* **1997**, *55*, 1566.

[74] J. S. Hansen, *Molecular Simulations* **2021**, *47*, 1391.

[75] J. S. Hansen, Nanoscale Hydrodynamics of Simple Systems, Cambridge University Press, **2022**.

[76] M. Vergeles, P. Keblinski, J. Koplik, J. Banavar, *Physical Review Letters* **1995**, *75*, 232–235.

[77] I. Bitsanis, T. Vanderlick, M. Tirrell, H. Davis, *Journal of Chemical Physics* **1988**, *89*, 3152.

[78] B. Dalton, P. Daivis, J. Hansen, B. Todd, *Physical Review E* **2013**, *88*, 052143.

[79] B. Dalton, K. Glavatskiy, P. Daivis, *Physical Review E* **2015**, *92*, 012108.

[80] S. Knudsen, B. D. Todd, J. S. Hansen, *Physics of Fluids* **2025**, *37*, 012021.

[81] L. Heitmeier, T. Voigtmann, J. S. Hansen, *Physics of Fluids* **2025**, *37*, 122019.

[82] E. R. Weaver, Propane, Butane, and Related Fuels, US Government Printing Office, **1938**.

[83] E. Almqvist in History of Industrial Gases, Springer, **2003**, pp. 47–135.

[84] M. Sattar, R. Saidur, H. H. Masjuki, *International Journal of Mechanical and Materials Engineering* **2007**, *2*, 154–160.

[85] G. Marcelli, T. Bottinelli Montandon, R. Ebrahimi Viand, F. Höfling, *The Journal of Chemical Physics* **2025**, *162*, 104101.

[86] N. Phan-Thien, N. Mai-Duy, Understanding viscoelasticity: An introduction to rheology, Springer, **2013**.

[87] gamdpy, GPU-Accelerated Molecular-Dynamics in Python, https://github.com/ThomasBechSchroeder/gamdpy.

[88] N. Bailey, T. Ingebrigtsen, J. S. Hansen, A. Veldhorst, L. Bøhling, C. Lemarchand, A. Olsen, A. Bacher, L. Costigliola, U. Pedersen, H. Larsen, J. Dyre, T. Schrøder, *SciPost Physics* **2017**, *3*, 038.

[89] J.-P. Ryckaert, A. Bellemans, *Chemical Physics Letters* **1975**, *30*, 123–125.

[90] J.-P. Ryckaert, A. Bellemans, *Faraday Discussions of the Chemical Society* **1978**, *66*, 95–106.

[91] R. Puscasu, B. Todd, P. Daivis, J. S. Hansen, *Physical Review E—Statistical Nonlinear and Soft Matter Physics* **2010**, *82*, 011801.

[92] S. Knudsen, B. Todd, J. S. Hansen, *Physics of Fluids* **2025**, *37*, 012021.

[93] M. Kunzner, C. Mayo, M. Sperl, J. P. Gabriel, *Physical Review E* **2025**, *112*, 025405.

[94] H. M. Jaeger, S. R. Nagel, R. P. Behringer, *Physics today* **1996**, *49*, 32–38.

[95] J. Duran, Sands, powders, and grains, Springer Science & Business Media, **2012**.

[96] A. Dufresne, *Earth surface processes and landforms* **2012**, *37*, 1527–1541.

[97] A. Rosato, K. J. Strandburg, F. Prinz, R. H. Swendsen, *Physical review letters* **1987**, *58*, 1038.

[98] M. Sweeney, L. L. Campbell, J. Hanson, M. L. Pantoya, G. F. Christopher, *Journal of Materials Science* **2017**, *52*, 13040–13053.

[99] S. Roy, T. Weinhart, *Granular Matter* **2024**, *26*, 102.

[100] O. Asaf, A. Bentur, P. Larianovsky, A. Sprecher, *Automation in Construction* **2024**, *166*, 105544.

[101] A. O. Siemens, M. Van Hecke, *Physica A: Statistical Mechanics and its Applications* **2010**, *389*, 4255–4264.

[102] H. Zhang, H. Makse, *Physical Review E—Statistical Nonlinear and Soft Matter Physics* **2005**, *72*, 011301.

[103] R. P. Behringer, B. Chakraborty, *Reports on Progress in Physics* **2018**, *82*, 012601.

[104] J. Zhang, T. Majmudar, M. Sperl, R. Behringer, *Soft Matter* **2010**, *6*, 2982–2991.

[105] A. Kudrolli, *Reports on progress in physics* **2004**, *67*, 209.

[106] J. E. Kollmer, T. Shreve, J. Claussen, S. Gerth, M. Salamon, N. Uhlmann, M. Schröter, T. Pöschel, *Physical Review Letters* **2020**, *125*, 048001.

[107] P. Eshuis, K. Van Der Weele, D. Van Der Meer, R. Bos, D. Lohse, *Physics of Fluids* **2007**, *19*, 12.

[108] M. A. El-Emam, L. Zhou, W. Shi, C. Han, L. Bai, R. Agarwal, *Archives of Computational Methods in Engineering* **2021**, *28*, 4979–5020.

[109] A. Hadi, R. Roeplal, Y. Pang, D. L. Schott, *KONA Powder and Particle Journal* **2024**, *41*, 78–107.

[110] A. Di Renzo, E. S. Napolitano, F. P. Di Maio, *Processes* **2021**, *9*, 279.

[111] L. F. Elizondo-Aguilera, E. C. Cortés-Morales, P. F. Z. Rico, M. Medina-Noyola, R. Castañeda-Priego, T. Voigtmann, G. Pérez-Ángel, *Soft matter* **2020**, *16*, 170–190.

[112] C. Scalliet, A. Gnoli, A. Puglisi, A. Vulpiani, *Physical Review Letters* **2015**, *114*, 198001.

[113] A. P. Thompson, H. M. Aktulga, R. Berger, D. S. Bolintineanu, W. M. Brown, P. S. Crozier, P. J. in 't Veld, A. Kohlmeyer, S. G. Moore, T. D. Nguyen, R. Shan, M. J. Stevens, J. Tranchida, C. Trott, S. J. Plimpton, *Computer Physics Communications* **2022**, *271*, 108171.

[114] N. V. Brilliantov, F. Spahn, J.-M. Hertzsch, T. Pöschel, *Physical Review E* **1996**, *53*, 5382.

[115] L. E. Silbert, D. Ertaş, G. S. Grest, T. C. Halsey, D. Levine, S. J. Plimpton, *Physical Review E* **2001**, *64*, 051302.

[116] Calculation of the Mean-Squared Displacement, `https://docs.lammps.org/compute_msd.html`.

[117] O. D'Angelo, F. Kuthe, S.-J. Liu, R. Wiedey, J. M. Bennett, M. Meisnar, A. Barnes, W. T. Kranz, T. Voigtmann, A. Meyer, *Additive Manufacturing* **2021**, *47*, 102349.

[118] K. Mair, J. F. Hazzard, *Earth and Planetary Science Letters* **2007**, *259*, 469–485.

[119] D. Vescovi, S. Luding, *Soft matter* **2016**, *12*, 8616–8628.

[120] K. F. Malone, B. H. Xu, *Particuology* **2008**, *6*, 521–528.

[121] A. Di Renzo, F. P. Di Maio, *Chemical Engineering Science* **2004**, *59*, 525–541.